

Comparative assessment of a mountain river flow resistance –
 1D-: sensitivity and prediction using data-based approaches

Juan Sebastián Cedillo Galarza



**UNIVERSIDAD
 DE CUENCA**



UCUENCA

Facultad de Ingeniería

Doctorado en Recursos Hídricos II cohorte

Comparative assessment of a mountain river flow resistance – 1D- : sensitivity and prediction using data-based approaches

Trabajo de titulación previo a la
obtención del título de Doctor
(PhD) en Recursos Hídricos

Autor:

Juan Sebastián Cedillo Galarza

CI: 0104057351

Correo electrónico: sebastiancedillo@gmail.com

Director:

Dr. Andrés Omar Alvarado Martínez

CI: 0102246477

Cuenca, Ecuador

16-noviembre-2022

Resumen

Los ríos de montaña son, con distancia, el caso más difícil de modelación hidráulica debido a las características de su lecho y sus mecanismos de disipación de energía en función de su morfología irregular. La resistencia, llamada también rugosidad o fricción juega un papel importante en los modelos de canal abierto 1-D para estimar diferentes variables. El parámetro de resistencia contiene todos los procesos disipativos en un río de montaña y suele valorarse mediante mediciones de campo, existiendo diferentes metodologías para estimarlo. En consecuencia, es fundamental determinar qué metodología es la más adecuada para predecirla. El parámetro de resistencia determinado en campo no siempre es el mismo que el utilizado en un modelo hidrodinámico. En la presente investigación diferentes morfologías han sido estudiadas en el río Quinuas (Ecuador): grada, lecho plano, y cascada. Los resultados muestran que las ecuaciones denominadas “Non-dimensional hydraulic geometry equations” (NDHG) son la mejor opción para predecir la velocidad en todos los tramos de ríos de montaña, además se ha desarrollado una metodología para encontrar sus parámetros. Las diferencias entre la rugosidad usada por el modelo matemático y la medida en campo dependen de la morfología y la magnitud de flujo. Finalmente, se implementó la técnica de “machine learning” que utiliza la física del sistema (Physics Informed Neural Network), con resultados satisfactorios para encontrar los niveles de agua y para la calibración del parámetro de resistencia.

Palabras clave: Resistencia al flujo; HEC-RAS; Physic informed neural network; Canal abierto; Río de montaña.

Abstract

Mountain -rivers are, by far, the most challenging case to model because of its bed characteristics and their energy dissipation mechanisms depending on its irregular morphology. Resistance, roughness, or friction parameter are equivalent terms. It plays an important role in 1-D open channel models to estimate different variables. Moreover, this parameter contains all the dissipative processes in a mountain river, and it is usually valued through field measurements, existing different methodologies to estimate it. Consequently, it is essential to determine which methodology is the most adequate to predict it. The resistance parameter determined in field is not always the same as the one used in a hydrodynamic model. In this thesis; cascades, plane bed, and step-pool has been studied in the Quinuas river (Ecuador). “Non-dimensional hydraulic geometry equations” (NDHG) were the best option to predict velocity in all the mountain river reaches. The parameters of NDHG varies depending on the author, therefore a methodology based on some field measurements to estimate the NDHG parameters was developed. The differences between model and field resistance coefficient depends on the morphology and flow magnitude. A machine learning technique using the system physics was develop providing optimal results to predict water depths and to calibrate resistance parameter.

Keywords: Flow resistance; HEC-RAS model; Physic informed neural network; Open channel; Mountain river.

CONTENTS

Resumen	3
Abstract.....	4
List of figures	8
List of tables	9
Acknowledge.....	15
Chapter 1	17
1 Introduction	17
1.1 Background.....	17
1.2 Objectives	18
1.3 Thesis outline.....	19
Chapter 2	22
2 Flow resistance literature review	22
2.1 Introduction	22
2.1 Resistance partitioning.....	22
2.1.1 Methodology description	22
2.1.2 Limitations.....	23
2.3 Common bed morphologies in mountain rivers.....	23
2.3.1 Plane bed.....	24
2.3.2 Cascade.....	25
2.3.3 Step-pool.....	25
2.4 Resistance field measurement.....	26
2.4.1 Description.....	26
2.4.2 Measurement	33
2.5 Resistance coefficient evaluation.....	35
2.5.1 Methodologies	35
2.5.2 Resistance prediction Eq. types	35
2.5.3 Use of D_{84} in resistance equations	39
2.5.4 Resistance equations: error and requirements.....	40
2.6 Unsteady resistance	40
2.7 Conclusions	41
Chapter 3	43
3 Flow resistance prediction in headwater mountain streams morphologies.....	43
3.1 Introduction	43
3.2 Materials and methods.....	44
3.2.1. River reach.....	44
3.2.2. Empirical resistance equations.....	48
3.2.3. Statistical performance metrics.....	49
3.2.4. Determination of NDHG parameters	50

3.2.5	51
3.2.6. Test with data from literature.....	51
3.3 Results	52
3.3.1 Best fitting equation.....	52
3.3.2. Estimation of NDHG Parameters.....	52
3.3.3. Variance decomposition methodology (VDM).....	55
3.3.4. Test with data from literature.....	56
3.4 Discussion.....	56
3.4.1 Characteristics of NDHG equations.....	56
3.4.2 NDHG parameters	57
3.4.3 Variance decomposition methodology (VDM).....	57
3.5 Conclusions	58
Chapter 4	59
4 Assessment of calibrated and measured based resistance parameter	59
4.1 Introduction	59
4.2 Materials and methods.....	60
4.2.1. Study area	60
4.2.2. Field data	61
4.2.3 Numerical scheme	63
4.2.4 The GLUE methodology	64
4.2.5 Uncertainty measurement analysis PRP	65
4.3 Results	65
4.3.1 Likelihood curves	65
4.3.2 Field measurements uncertainty	69
4.3.3 Effective and measured resistance values.....	69
4.4 Discussion.....	75
4.4.1 Likelihood curves	75
4.4.2 Likelihood peak values.....	76
4.4.3 Friction slope methodology	76
4.4.4 Effective resistance coefficient (ERC) and physical resistance parameter (PRP)	76
4.5 Conclusions	78
Chapter 5	79
5 Physics-informed neural network scheme to calibrate flow resistance in 1d steady-state open channel cases .	79
5.1 Introduction	79
5.2 Materials and methods.....	80
5.2.1 Cases under study	80
5.2.2 Physics-informed neural network (PINN)	83
5.2.3 HEC RAS model.....	87
5.2.4 Direct step method.....	87
5.2.5 Metrics.....	87

5.2.6 Systematic studies.....	87
5.3 Results	88
5.3.1 Equivalent cross-section	88
5.3.2 Forward PINN: solving the differential equation	90
5.3.3 Inverse PINN	95
5.3.4 Results of the systematic studies.....	96
5.4 Discussion.....	99
5.4.1 Activation function performance	99
5.4.2 Neural network architecture.....	99
5.4.3 PINN predictability.....	100
5.4.4 Systematic studies.....	100
5.5 Conclusions	101
Chapter 6	102
6 Conclusions	102
6.1 Physical resistance parameter (PRP)	102
6.2 Effective resistance coefficient (ERC).....	103
6.3 PINN application to mountain rivers	103
6.4 Research limitations and further research.....	103
References	104
Curriculum vitae.....	110
Symbology and abbreviations.....	112

List of figures

Figure 1.1: Thesis description and relation between different chapters.....	20
Figure 2.1: Conductance-time curves	29
Figure 3.1: Plan view of the studied 1500 km river reach showing the sequence of the sub-reaches and the location of the meteorological station.	45
Figure 3.2: Linear regression of Eq. (3.3) for 50% of the data provided in (Jarrett, 1984) and (Bathurst, 1985) randomly chosen.....	51
Figure 3.3: Linear regression of Equation (3): (a) Cascade 1; (b) Cascade 2; (c) Cascade 3; (d) Step-pool 1; (e) Step-pool 2; (f) Plane-bed.....	54
Figure 3.4: Plot of observed and predicted velocity values: (a) Cascade; (b) Step-pool; (c) Plane-bed.....	56
Figure 4.1: Location of the 1.5 km river reach with indication of the different morphologies.....	61
Figure 4.2: Profiles and topographic characteristics of morphologies under study. (a) Step-pool 1 (b) Cascade 3 (c) Plain bed 1.....	62
Figure 4.3 : Pictures of analyzed reaches. (a) Step-pool 1 (b) Cascade 3 (c) Plain bed 1.....	63
Figure 4.4: GLUE likelihood curves in Experiment 1: Cascade (a, b, c), Plane-bed (d, e, f), and Step-pool (g, h, i).....	66
Figure 4.5: GLUE likelihood curves in Experiment 2: Cascade (a, b, c), Plane-bed (d, e, f), and Step-pool (g, h, i).....	68
Figure 4.6: Comparison of measured and calibrated n values. (a) Cascade (b) Plane bed (c)Step-pool.....	72
Figure 4.7: Water surface profiles using ERC and PRP in Cascade. a) $0.065 \text{ m}^3\text{s}^{-1}$ b) $0.485 \text{ m}^3\text{s}^{-1}$ c) $0.708 \text{ m}^3\text{s}^{-1}$	73
Figure 4.8: Water surface profiles using ERC and PRP in Plane-Bed. a) $0.063 \text{ m}^3\text{s}^{-1}$ b) $0.513 \text{ m}^3\text{s}^{-1}$ c) $0.918 \text{ m}^3\text{s}^{-1}$	74
Figure 4.9: Water surface profiles using ERC and PRP in Step-pool. a) $0.035 \text{ m}^3\text{s}^{-1}$ b) $0.443 \text{ m}^3\text{s}^{-1}$ c) $0.878 \text{ m}^3\text{s}^{-1}$	75
Figure 5.1: . Bed profile for different cases. Benchmark cases: (a) Case 1, (b) Case 2, (c) Case 3, (d) Case 4, Real Case: (e) Step-pool	82
Figure 5.2: Plan view of the studied 1500 km river reach showing the sequence of the sub-reaches and the location of the meteorological station.	83
Figure 5.3: Physics-Informed Deep Learning shemes: a)Forward problem: Benchmark cases b) Forward Problem:Real Case c) Inverse problem: Real Case	86
Figure 5.4: Cross sections in Step-pool and equivalent cross section.....	89
Figure 5.5: Area and Hydraulic Radius data of the equivalent cross-section. (a) Area, (b) Hydraulic Radius.....	90
Figure 5.6: PINN results with the best case for each activation function for: (a) Case 1, (b) Case 2, (c) Case3, and (d) Case 4.....	93
Figure 5.7: PINN results with the best case for each activation function for Step-pool: (a) Low flow, (b) Mid flow, and (c) High Flow	94
Figure 5.8: PINN results with the best case for each activation function for Step-pool, high flow.....	95
Figure 5.9: Rate of convergence. (a) Case 1, (b) Case 2, (c) Case 3, (d) Case 4, and (e) Case 5	97
Figure 5.10: Sensibility test. (a) Case 1, (b) Case 2, (c) Case 3, (d) Case 4, and (e) Case 5.....	98

List of tables

Table 1.1: Advantages and disadvantages of different models	18
Table 2.1: Mountain river morphology, schemes adapted from (Chin & Wohl, 2005; Comiti et al., 2009; Maxwell & Papanicolaou, 2001; Montgomery & Buffington, 1997)	24
Table 2.2: Field measurement methodologies	30
Table 2.3: Empirical Resistance Equations	38
Table 3.1: Longitudinal profiles and pictures of Cascade, Step-pool, and Plane-bed.....	46
Table 3.2: Average geometry characteristics of the studied reaches.	47
Table 3.3: Resistance equations tested in this chapter.	48
Table 3.4: Statistical fitting metrics for Cascade, Step-pool, and Plane-bed morphologies.	52
Table 3.5: NDHG exponents based on the proposed methodology.	53
Table 3.6: Comparison of proposed NDHG equations with previously best-performing empirical equations. ...	55
Table 3.7: Variance decomposition methodology for the studied morphologies.....	55
Table 3.8: Comparison of the proposed NDHG equation (NDHGlit) with the previously best-performing empirical equation.	56
Table 4.1: Range of values for measured and calibrated n value for Experiment 1	70
Table 4.2: Range of values for calibrated n value for Experiment 2	71
Table 4.3: Bed material quartiles and mean depth for each morphology and flow magnitudes.	77
Table 5.1: Best cases of activation functions based on loss function	92
Table 5.2: Inverse PINN comparison between calibrated resistance values from GLUE experiments and the ones obtained from different AFs and different flow values.....	96

Cláusula de licencia y autorización para publicación en el Repositorio Institucional

Juan Sebastián Cedillo Galarza, en calidad de autor y titular de los derechos morales y patrimoniales del trabajo de titulación “Comparative assessment of a mountain river flow resistance – 1D: sensitivity and prediction using data-based approaches”, de conformidad con el Art. 114 del CÓDIGO ORGÁNICO DE LA ECONOMÍA SOCIAL DE LOS CONOCIMIENTOS, CREATIVIDAD E INNOVACIÓN reconozco a favor de la Universidad de Cuenca una licencia gratuita, intransferible y no exclusiva para el uso no comercial de la obra, con fines estrictamente académicos.

Asimismo, autorizo a la Universidad de Cuenca para que realice la publicación de este trabajo de titulación en el repositorio institucional, de conformidad a lo dispuesto en el Art. 144 de la Ley Orgánica de Educación Superior.

Cuenca, 16 de noviembre de 2022



Juan Sebastián Cedillo Galarza
C.I: 0104057351

Juan Sebastián Cedillo Galarza, autor del trabajo de titulación “Comparative assessment of a mountain river flow resistance – 1D-: sensitivity and prediction using data-based approaches”, certifico que todas las ideas, opiniones y contenidos expuestos en la presente investigación son de exclusiva responsabilidad de su autora.

Cuenca, 16 de noviembre de 2022



Juan Sebastián Cedillo Galarza
C.I: 0104057351

Supervisor

Prof. Dr. Andrés Alvarado Martínez
Department of Water Resources and Environmental Sciences
University of Cuenca

Co-supervisors

Prof. Dr. Esteban Patricio Samaniego
Department of Water Resources and Environmental Sciences
University of Cuenca

Prof. Dr. Luis Timbe
Department of Water Resources and Environmental Sciences
University of Cuenca

Assessment committee

Prof. Dr. Patricio Crespo (Universidad de Cuenca, Ecuador).
Prof. Dr. Lenin Vladimir Campozano Parra (Escuela Politécnica Nacional, Ecuador).
Prof. Dr. Pablo Guzmán (Universidad del Azuay, Ecuador).

Dean of the Faculty

Dr. Lorena Catalina Sigüenza Guzmán

Rector of the University

Dr. María Augusta Hermida

Comparative Assessment of a Mountain River Flow Resistance – 1D-:
Sensitivity and Prediction Using Data-Based Approaches

Thesis submitted in partial fulfillment of the requirements for the degree of
Doctor of Philosophy in Water Resources

Spanish translation of the title:

Evaluación comparativa de la resistencia al flujo de un río de montaña - 1D-: sensibilidad y predicción utilizando enfoques basados en datos

Refer to this work as follows:

Cedillo S, 2022. Comparative assessment of a mountain river flow resistance – 1D-: sensitivity and prediction using data-based approaches. PhD thesis, Universidad de Cuenca, Escuela Politécnica Nacional and Universidad Técnica Particular de Loja, Ecuador.

Faculty:

Faculty of Engineering, University of Cuenca.

Department:

Department of Water Resources and Environmental Sciences, University of Cuenca.

Universities:

Universidad de Cuenca, Escuela Politécnica Nacional y Universidad Técnica Particular de Loja.

City:

Cuenca, Ecuador.

Acknowledge

I want to thank all the people involved in the development of this thesis work: Prof. Dr. Andrés Alvarado, Prof. Dr., Prof. Dr. Esteban Samaniego, Prof. Dr. Luis Timbe, Prof. Dr. Esteban Sánchez, and Dr. Gabriela Nuñez. I want to thank assessment committee for the invested time and comments to improve the quality of this thesis: Prof. Dr. Patricio Crespo, Prof. Dr. Lenin Vladimir Campozano Parra, and Prof. Dr. Pablo Guzmán.

I want to thank to my family: Lautaro, Patricia and Adrian.

I want to thank to my friends: Gina Berrones, Mario Navas, Emilio Navas, and Sheila Serrano.

Chapter 1

1 Introduction

1.1 Background

Rivers has been an upside and downside for human development. They have been essential in the human development providing drinking water, power supply, navigation, and receiving wastewater from cities (Chapra, 2008). However, rivers can be a menace for humans as well. Flooding is considered one of the most damaging natural disasters which occurrence is increasing due to global warming (Camp et al., 2016; Douben, 2006). Thus, improving knowledge of the interaction of water and its boundaries will collaborate to an increased understanding of the river behavior. The focus of the present thesis is the mountain rivers and the study of the main feature of the river hydraulics: the resistance to flow.

To understand the resistance to flow, the bed material needs to be considered. Firstly, it has a bimodal distribution (Bathurst, 2002). Indeed, the bed material is coarse poorly sorted (Wohl, 2000) with the presence of boulders which protrude above water level (Jarrett, 1984). Secondly, boulders increase flow resistance because water hits its protruding surface producing jets between them (Pagliara & Chiavaccini, 2006) and eddies behind it depends on the concentration of boulders (Jarrett, 1984). Thirdly, the water depth has the same magnitude as bed material producing a near-bed flow (Aberle & Smart, 2003; Maxwell & Papanicolaou, 2001). Thus, there is a low relative submergence (d/D_{84}) with a range between 4 to 10 (Bathurst, 2002). Fourthly, while in plane rivers the velocity distribution is semi-logarithmic, in mountain rivers there is a S-shape velocity distribution (Wohl, 2000). Therefore, the analysis of resistance in mountain rivers is crucial and challenging due to the complex interaction of the river with its boundaries (Romero et al., 2010).

The resistance to flow in an open channel under the supposition of one-dimensional flow is considered through a parameter called “rugosity”. There are different rugosity parameters present in the literature such as Chezy (C), Darcy–Weisbach (f), and Manning (n). The former two (f and n) are used in this thesis for field measurements and for hydrodynamic modelling. f is dimensionless and has physical interpretation being widely used in resistance measurement research (Ferguson, 2007), while n is the resistance parameter present in the energy equation widely used for hydraulic modeling (eg. HEC-RAS).

There are different methodologies to estimate the Physical Resistance Parameter (PRP) based on field data and observations (Marcus et al., 1992): empirical equations, photography’s, or tables (Wohl, 1998). Methods based on tables and photography’s consist of finding a reach similar than the one under study which is intrinsically biased. A better option is the use of empirical equations. These equations require variables that are easily measurable and needs to consider at-a-site as well as between-site effects on resistance to be reliable (Bathurst, 2002; Ferguson, 2007). Nevertheless, available formulas to estimate f may have errors of around 30% because they were developed through the average of variations in multiple sites (Bathurst, 2002). There are different types of empirical equations such as Semilogarithmic (Bathurst, 1985), Exponential (Bathurst, 2002), and Nondimensional Hydraulic Geometry Equations (Ferguson, 2007), each of them tested under different conditions: different morphologies, flume and field data. The field data is limited to rivers in the United States and Europe, but field data from an Andean river is limited to Romero et al. (2010). Thus; a first step in this work is to determine the best equation to predict resistance in all the available reaches and then to propose a procedure to find its parameters.

Hydraulic models (HM) are intended to replicate the flow of a fluid (Teng et al., 2017). Furthermore, One-dimensional HM are still used and are considered a good predictor of river and canal hydraulic modeling when adequate topographic data is available (Cook & Merwade, 2009; Horritt & Bates, 2002). These models are popular due to a low computational demand and low investment in data collection since only point measurements of flow and water depth are required (Horritt & Bates, 2002; Teng et al., 2017). One-dimensional HM include some assumptions to represent the reality mathematically leading to structural errors (Bozzi et al., 2015). Moreover, there are errors in input data, model parameters and calibration data leading to model output uncertainties (Jung & Merwade, 2012). Thus, there is not a single set of optimal parameters, instead there is a set of parameters which has the same model performance which is called equifinality. A methodology called Generalized Likelihood Uncertainty Estimation (GLUE) is available to consider equifinality and to study the resistance parameter in one-dimensional HM needed to obtain representative results (Wohl, 1998). The Effective Resistance Coefficient (ERC) found with GLUE is a resistance parameter which contains the different processes playing important effects on model results (Horritt & Bates, 2002), but is not necessary the same as the physical resistance parameters (PRP). Hence, based on the important role of resistance parameter in HM,

it seems crucial to know the conditions when there is a marked difference between PRP and ERC. Indeed, those discrepancies could affect model performance.

Deep learning is a technique able to approximate the behavior of a system based on data input (Raissi et al., 2017b; Tartakovsky et al., 2020). In some physical systems the availability of data is limited, so the introduction of the governing physics as additional information in deep learning has resulted in the so-called Physics-Informed Deep Learning (PIDL) (Raissi et al., 2017b). The inclusion of physical laws in the deep learning technique reduces dependency on large, high-quality data sets and provides a robust model with physical significance (Raissi, Yazdani, et al., 2018; Wang et al., 2020). The computations of the derivatives in deep learning are through Automatic Differentiation (AD) (Wang et al., 2020). AD refers to a family of techniques where the derivative calculation is divided into elementary operations where symbolic differentiation is used, then the values are stored and accumulated to generate the overall derivative value (Güneş Baydin et al., 2018). PIDL can solve forward and inverse problems. In a forward problem, the training points are obtained from boundary and initial conditions where the conservative equations are enforced to obtain a stable solution (Mao et al., 2020). An inverse problem consists of deducing the hidden quantities such as parameters using scattered and noisy observations (Raissi et al., 2017a). Physics Informed Deep Learning has been successfully used to solve hydraulic benchmark cases (Mao et al., 2020; Raissi et al., 2017a, 2017b; Wang et al., 2020). Consequently, PIDL is an promising methodology to test in mountain rivers to predict the water level profile as well as to calibrate the resistance parameter being both important problems during hydrodynamic modelling.

One of the most challenging cases for modelling in mountain rivers is the analysis of Step-pool. This is a common morphology in mountain rivers with a staircase shape where risers are steps and pools are treads (Maxwell & Papanicolaou, 2001). Steps are generally formed of different materials, such as alluvial boulders, large wood debris, or bedrock (Curran & Wohl, 2003; MacFarlane & Wohl, 2003); while pools are made of finer granulometric materials (Lee & Ferguson, 2002). In steps, water jets are produced where the flow is supercritical. When the water falls into the pools, a hydraulic jump is produced, forming air pockets (Chin & Wohl, 2005). This morphology plays an important environmental and hydraulic role in steep rivers (MacFarlane & Wohl, 2003), helping the oxygen transfer to the water body. However, due to the process described, its hydraulic modeling is defiant. In this thesis, we have employed a widely used hydrodynamic model HEC-RAS to simulate different river reaches as well as PIDL. PIDL has gained interest in the hydraulic field due to the use of conservation laws. Based on the literature review, it is the first time that HEC RAS and PIDL results are compared in the simulation of mountain rivers.

Finally, there are two important aspects to be discussed. First, it is important to notice that the term roughness refers to the flow resistance produced when water flows above or through a certain roughness element. Thus, resistance and roughness parameter in this case are the equivalent. Second, all the reaches under analysis have a unidimensional preferential flow, so the use of one-dimensional models approach make sense. In Table 1.1 some advantages and disadvantages of different dimensional models are explained.

Table 1.1: Advantages and disadvantages of different models

Model	Advantage	Disadvantage
One-dimensional	Less computational demand More simple mathematical formulation Punctual field data needed for validation	The results are cross-sectional averages. Some physical phenomena are not considered e.g. turbulence, interaction main channel-flood plain
Two and Three Dimensional	More complex mathematical formulation Include additional physical phenomena The output provides distributed data	Requires more modeler experience High computational demand Much more detailed distributed field data is required

1.2 Objectives

In this thesis, resistance has been researched from two points of view. Firstly, a Physical Resistance Parameter (PRP) which is measured through field measurements. Secondly, an Effective Resistance Coefficient (ERC) based on GLUE experiments comparing the predictability of models with different resistance values. Given that PRP and ERC are available, the aims of this research project has therefore been:

- To compare the fitting performance of several empirical resistance equations to predict velocity in mountain rivers. Then, to develop a new methodology to estimate the parameters of the best equation.
- To assess two important parameters in a hydrodynamic model for steady state flow: resistance factor and Representative Friction Slope Method (RFSM) applying GLUE methodology on HEC-RAS modelling. The calibrated resistance parameter found with GLUE (ERC) is compared with the resistance parameter obtained through field measurements (PRP). Furthermore, the influence of the RFSM is determined during the energy equation solution in HEC-RAS modelling.
- To use Physics Informed Deep Learning as an alternative method to calibrate resistance factor in mountain rivers having results comparable to GLUE.

1.3 Thesis outline

Figure 1.1 depicts a graphical description of the different aims of this thesis and how they relate with each other until reaching PIDL. This model uses the results and measurements of all the working packages.

Chapter 2 deals with several aspects of mountain rivers required to understand next chapters. The key aspects of the literature review can be listed as follows: Resistance Partitioning, Common Morphologies, Resistance Field Measurements, Resistance Coefficient Evaluation, and Unsteady Resistance.

Chapter 3 deals with the estimation of Physical Resistance Parameter (PRP) to estimate mean velocity in the studied reaches. Furthermore, different empirical equation to estimate flow resistance as well as to estimate mean velocity were tested. The equation with the best predictability was studied deeply to find a methodology to estimate its parameters.

The GLUE experiments to find Effective Resistance Coefficient (ERC) and the effect of varying Representative Friction Slope Method (RFSM) when energy equation is solved in HEC-RAS is given in Chapter 4. Furthermore, a comparison between PRP and ERC is done under different dissipative conditions at different reaches.

In chapter 5 a PIDL model was assembled for open channels with different profiles and a real case for forward problems. The same PIDL structure was used to solve an inverse problem in a real case and to compare results with chapter 4.

2 Flow resistance literature review

2.1 Introduction

Studies in mountain streams have evolved from the analysis of grain resistance from straight reaches to analyze more resistance components at different bed morphologies. Jarrett (1984) developed an investigation of grain resistance in 21 straight and uniform high-gradient reaches at Rocky mountains of Colorado. Bathurst (1985) studied total resistance with a combination of field and flume data. Field data came from riffles and other typical steep mountain reaches in British mountains. Bathurst (2002) research of grain resistance is based on literature data with uniform flow reaches. Maxwell & Papanicolaou (2001) performed a flume experiment to determine geometric as well as resistance characteristics of step-pools. Lee & Ferguson (2002) combined field and flume experiments to study step-pools formed by boulders, bedrock, and not large woody debris (LWD) where the resistance length scale was modified. Aberle & Smart (2003) develops a flume study with different bed profiles since the hydraulic resistance change with bed surface and not with a characteristic diameter. Curran & Wohl (2003) studied the effect of LWD on resistance in 20 step-pools. Wilcox & Wohl (2006) did a flume experiment where the effects on resistance of different LWD configurations is obtained. Ferguson (2007) developed nondimensional hydraulic geometry equations (NDGH) based on field velocity data from different countries. Wilcox & Wohl (2006) did a flume experiment where the effects on resistance of different LWD configurations is obtained. Ferguson (2007) developed nondimensional hydraulic geometry equations (NDGH) based on field velocity data from different countries. The data includes morphologies such as runs, riffle, pool-riffle, and step-pool without woody debris or bed rock. Comiti et al. (2007) use field data plus additional published data of majority step-pools to research modifications in NDGH equations. The inclusion of relative steepness to these equations provides the best result. Pagliara et al. (2008) simulates rock chutes with crushed stone and smooth lead hemispheres. It was showed that the increase of boulder concentration increases the formation of eddies behind boulders due to the higher interaction of water surface with particle surface. Comiti et al. (2009) studied the change in resistance characteristics in step-pools at nappe and skimming flow. Romero et al. (2010) took data of five steep rivers in Cochabamba Bolivia to test the applicability of several empirical equations. Zimmermann (2010) used flume experiments to investigate the consequences of modifications in a NDHG where the resistance length was modified and an additional term was added. David et al. (2010) researched nine step-pools, five cascades, and one plane-bed. This data was used to look for correlation of resistance parameter f with different control variables. Cascade and step-pool has different control variables due to the dominance of a certain resistance components. Besides; when the predictability of empirical equations is analyzed, it is required separate data according to bed morphology. Rickenmann & Recking (2011) used 2890 field measurements to test the velocity predictability of new dimensionless variables to develop a new NDHG. Nitsche et al. (2012) investigates the results of six reaches in the swiss alps including plane bed/riffle, step-pool, and cascade morphologies complemented with eight other Swiss mountain streams. First, they find through a dimensional analysis the dimensionless variables found by Rickenmann & Recking (2011). Second, all the data collapsed to a single power law of both dimensionless variables including a prefactor which correlate with boulder density independently of the resistance length for NDHG.

The goal of the current chapter paper is to provide an overview of certain aspects of field resistance. An explanation and suitability of the application of Resistance Partitioning is given in Section 2.2. Section 2.3 introduces common morphologies present in mountain rivers. In this section there is a geometric as well as resistance description of each one. Section 2.4 and Section 2.5 illustrates methodologies to measure field resistance and methodologies for its prediction. Finally, section 2.7 contains information related with non-stationary resistance.

2.1 Resistance partitioning

2.1.1 Methodology description

Partitioning methodology considers that the total hydraulic resistance is composed of multiple components both independent and additives (Wilcox et al., 2006). Indeed, the components are grain and form resistance.

Grain resistance is generated due to the interaction of water with bed material along the river (bed-resistance) (Curran & Wohl, 2003). In contrast to Plane Rivers, where grain resistance is not important at high flows, in Mountain Rivers with a bed of coarse poorly sorted clasts, bed forms, and small relative depth, this resistance component becomes representative (Aberle & Smart, 2003). Grain resistance is composed of skin friction and drag force. The former one is the viscous and shear dissipation created by the vertical distribution of velocities while the latter is created by a pressure gradient which opposes flow when water interacts with an obstacle (Wohl, 2000).

Form resistance is the degradation of energy due to flow obstacles that create drag forces, pressure differences, flow separation and macroscale resistance (Curran & Wohl, 2003; Ferro & Giordano, 1991). This component depends on the geometry of the obstacle, changes in channel alignment, cross-sectional shape, slope, and flow velocity (Ferro & Giordano, 1991). Spill resistance is a component that is part of the form resistance, it occurs due to sudden deceleration of water resulting of hydraulic jumps, extreme turbulence and vertical falls produced in the tumbling flow (Curran & Wohl, 2003).

Assuming the concept of Resistance Partitioning, then the Friction slope, S_f , can be divisible into the Friction slope due to the grain resistance, $S_{f-grain}$, and Friction slope due to the bed forms, S_{f-form} (Eq.(2.1)).

$$S_f = S_{f-grain} + S_{f-form} \quad (2.1)$$

Combination with the Darcy–Weisbach resistance equation produces the Eq. (2.2)

$$\frac{f U^2}{8 g R} = \frac{f_{grain} U^2}{8 g R} + \frac{f_{form} U^2}{8 g R} \quad (2.2)$$

A simplification of parameters produces Eq. (2.3) where f_{grain} and f_{form} are the friction factors to grain resistance and bed forms respectively.

$$f = f_{grain} + f_{form} \quad (2.3)$$

2.1.2 Limitations

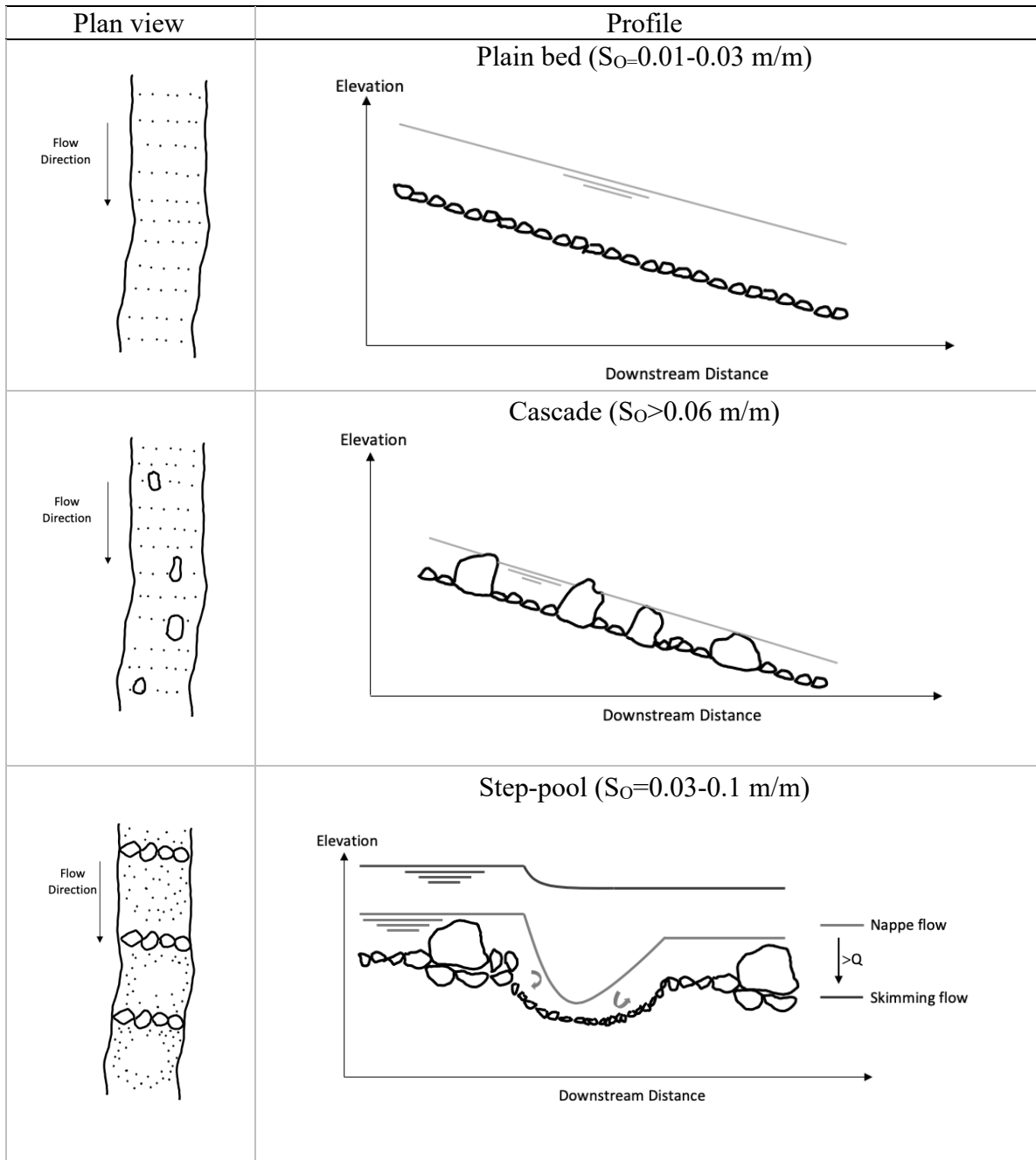
Although resistance partitioning is a widely applied methodology, there is controversy in its use. According to Zimmermann (2010), resistance partitioning is not entirely useful in mountain rivers since bed material, such as boulders and cobbles, generates at the same time f_{grain} and f_{form} . These phenomena can be illustrated in the flume study developed by Wilcox et al. (2006). In that study flow resistance is mainly created by bed sediments, spill over step-pool bed forms, and large woody debris (LWD). The results of this study showed that:

- Partitioning estimates are highly sensitive to the order in which the components are calculated: measured or left-over terms in Eq. (2.3).
- Left-over parameter is over-estimated since it contains the interactions of resistance components.
- The combined effect of LWD and spill over-steps dominates flow resistance.
- Grain resistance is a small component of total resistance.

2.3 Common bed morphologies in mountain rivers

Early mountain rivers studies did not have a standard description of the morphologies present in a river reach. Jarrett (1984) did not provide a description of studied morphologies. In that study, a wide range of reach characteristics is covered. Bathurst (1986) studied two types of sites; in the first one, a river-reach compound of riffle and pool at both sites, upstream and downstream, while the second one, a boulder bed without pools is described. Marcus et al. (1992) describes the longitudinal characteristics of the bed material along the reaches. In 1997, Montgomery & Buffington (1997) proposes for the first time a standardization of the different types of morphologies present in the mountain rivers based on common characteristics in field observations. Moreover, in alluvial channels five-reach types are recognized: cascade, step-pool, plane bed, pool riffle, and dune-riffle. More recently, David et al. (2010) presented a study in which mountain rivers morphology is dominated by plane- beds, cascade, and step-pool.

Table 2.1: Mountain river morphology, schemes adapted from (Chin & Wohl, 2005; Comiti et al., 2009; Maxwell & Papanicolaou, 2001; Montgomery & Buffington, 1997)



2.3.1 Plane bed

2.3.1.1 Description

Plane bed morphology occurs in straight-aligned channels where bed material consists on cobbles and gravels (Montgomery & Buffington, 1997), Refers to Table 2.1. In this morphology, there is no regular bed form patterns (David et al., 2010).

2.3.1.2 Resistance characteristics

In this morphology there is interaction of water with bed material only which produces grain resistance and form resistance.

2.3.2 Cascade

2.3.2.1 Description

Cascade presents a longitudinal and transversal disorganization of cobbles and boulders (Table 2.1). Around and over these particles the flow pattern is: wake, jet and tumbling flow (Montgomery & Buffington, 1997).

2.3.2.2 Resistance characteristics

The presence of particle with intermediate diameter bigger than 64mm (boulders and cobbles) produces different dissipative processes besides skin friction. At low flows, these big bed material protrude above water level producing wave drag (David et al., 2010). Most of the energy dissipation is produced by jet and wake flow around big clast which produces tumbling flow and turbulence (Montgomery & Buffington, 1997).

2.3.3 Step-pool

2.3.3.1 Description

Step-pool is the most common morphology in gravel beds and have a staircase regular pattern (Maxwell & Papanicolaou, 2001), Refers Table 2.1. Steps are composed of alluvial boulders (MacFarlane & Wohl, 2003), large wood debris (LWD), a combination of both, or bed rock (Curran & Wohl, 2003) while Pools are behind every step, where finer material is trapped (Lee & Ferguson, 2002).

Step-pools has important hydraulic and environmental function in steep rivers (MacFarlane & Wohl, 2003). Steps reduce the available potential energy to be transformed into kinetic energy for sediment transport (Chin & Wohl, 2005). In pools, the flow velocity is reduced resulting in a limitation of conveyance of hazardous flooding events downstream (MacFarlane & Wohl, 2003) as well as the deposition of sediment and nutrients. The former phenomena improve aquatic habitat and water quality (Curran & Wohl, 2003; MacFarlane & Wohl, 2003). Step-pools regulates resistance through vertical adjustment of bed and uniformly spaced steps. This is accomplished with the relation $H/L/S_o$ (H step height; L step length) having a constant range of 1 to 2 (Chin & Wohl, 2005).

Step-pools flow patterns is called Nappe flow (Comiti et al., 2009) having a change between subcritical and supercritical flow. There is supercritical flow at step lip where a water jet is form and plunge into the next pool where air pockets and hydraulic jump is formed producing the change from supercritical to subcritical flow (Tumbling flow) (Chin & Wohl, 2005).

The presence or not of Large Wood Debris (LWD) at step lips influence the geometric characteristics (Wilcox & Wohl, 2006). LWD occurrence increases step height (Curran & Wohl, 2003) and pool length. On the other hand, its absence produces step-pools with higher frequency of steps but with smaller step height and pool length (MacFarlane & Wohl, 2003).

2.3.3.2 Resistance characteristics

In Step-pools, both steps and pools contribute with form resistance. In steps there is an interaction of flow with step-forming material producing flow separation, channel expansion and contraction due to boulders and irregularities (Curran & Wohl, 2003). Furthermore, in pools there is water deacceleration as a consequence of a hydraulic jump producing spill resistance (Chin & Wohl, 2005).

The presence of LWD influences all resistance components in step-pools (MacFarlane & Wohl, 2003). LWD reduce f_{grain} due to the damming effect that occurs in pools increasing water depth and relative submergence (d/D_{xx} ; d water depth and D_{xx} is a characteristic bed material diameter)(MacFarlane & Wohl, 2003; Wilcox & Wohl, 2006). f_{form} is influenced by changes in the channel-width leading to variations in channel-form increasing the resistance component (MacFarlane & Wohl, 2003). LWD forms higher steps with longer pools where bigger hydraulic jumps are formed and more energy is dissipated (MacFarlane & Wohl, 2003). Hence, f_{spill} is higher because this resistance component depends on the height and length step ratio (H/L). Wilcox & Wohl (2006) developed a flume experiment with homogenous bed material stick to the bed where LWD are simulated with PVC pipes. This study concludes that the position, density, orientation, and length of LWD has diverse effects on resistance.

2.4 Resistance field measurement

2.4.1 Description

Several methods have been proposed in the literature to estimate the parameters required for resistance measurement, one of the main causes of the wide variety existing in predictive equations. Equations based on uniform flow are used to estimate field resistance, one of the most used is the Darcy–Weisbach resistance Eq. (2.4).

$$f = \frac{8 g R S_f}{U^2} \quad (2.4)$$

Where:

g gravitational acceleration ($L T^{-2}$)

R Hydraulic radius (L)

S_f Energy slope (-)

U Velocity ($L T^{-1}$)

According to Aberle & Smart (2003), there are two general ways to collect data in mountain rivers. In the first methodology, a specific cross-section is chosen where: area, water level, and velocity (using current meter) are measured. So, the discharge is obtained through the continuity equation (Eq.(2.5)). In this methodology, for each cross-section m water-depth measurements at constant width intervals (Δw_i) must be taken to obtain a mean water-depth (Eq. (2.6)). Area (A) is obtained with integration of those depths. Note that this methodology depends on the selection of representative cross-sections in the river-reach. In the second methodology, discharge, and velocity are measured using tracers. The mean-depth is calculated using the continuity equation (Eq. (2.5)). This methodology may provide better results because the velocity is determined by using tracers instead of the current meter. The current meter in Mountain Rivers could present difficulties due to its low relative immersion submergence.

$$Q = U A = U w d \quad (2.5)$$

Where:

U velocity ($L T^{-1}$)

A cross sectional area (L^2)

w wetted width (L)

d mean depth (L)

$$d = \frac{\sum d_i \cdot \Delta w_i}{\sum \Delta w_i} \quad (2.6)$$

Where:

d_i measured depth at certain $n \cdot \Delta w_i$ (L)

Geometric characteristics in Mountain Rivers are measured by using theodolite and stadia rod (MacFarlane & Wohl, 2003), laser theodolite (David et al., 2010), total station (Curran & Wohl, 2003; Lee & Ferguson, 2002), and LIDAR (Yochum, 2010). Additionally, the reach under study is commonly divided into cross sections perpendicular to the primary flow (MacFarlane & Wohl, 2003). The number of cross sections varied from three (Bathurst, 1985) to ten or eleven (MacFarlane & Wohl, 2003). Therefore, the parameters in Eq. (2.4) are averaged values of all the cross sections

that structure the river-reach studied. The longitudinal profile is measured through thalweg points (Curran & Wohl, 2003; MacFarlane & Wohl, 2003; Yochum, 2010) so that the mean bed slope (S_O) is obtained with a linear regression of collected points (David et al., 2010).

The gradient of the energy line in the river, S_f , is calculated with Eq. (2.7) which can be approximated with S_w (Water surface gradient) or S_O (Bed slope). Bathurst (1985) got better results when $S_f = S_w$ approach is used, attributing these results to small velocity head gradient, local resistance effects and velocities in mountain rivers which hide the long-stream changes. David et al. (2010) studied a step-pool while Yochum & Bledsoe (2010) studied step-pool, cascade, and plane bed reaches; both studies considered the S_w approach. On the other hand, the use of S_O produces a difference in resistance estimation of +/- 5% when Eq. (2.4) is applied (Lee & Ferguson, 2002). Marcus et al. (1992) states that the difference between S_f and S_O can reach 30% at bankfull stage.

$$S_f = S_w + \frac{(1-k) \cdot \frac{\Delta \cdot \alpha \cdot U}{2 \cdot g}}{L} \quad (2.7)$$

Where:

S_f Energy gradient (-)

S_w Water surface slope (-). $S_w = S_O + \frac{\partial d}{\partial x}$

d water level (L)

U velocity ($L T^{-1}$)

L reach length (L)

g gravity acceleration ($L T^{-2}$)

The application of the Tracer Slug Injection (TSI) methodology, where discharge and velocity are measured, in shallow, turbulent and morphological complex mountain rivers has become a viable alternative given the satisfactory results obtained (Curran & Wohl, 2003; Wilcox & Wohl, 2006). In the literature, two tracers are the most widely used: Rhodamine WT (David et al., 2010; Yochum, 2010) and Salt (Aberle & Smart, 2003; Curran & Wohl, 2003; Lee & Ferguson, 2002; MacFarlane & Wohl, 2003; Wilcox & Wohl, 2006).

In TSI methodology, a certain amount of tracer mass is punctually injected at a certain distance upstream from the measurement device. The devices to be installed are a fluorometer or an electrical conductivity probe, for the Rhodamine WT or the salt, respectively. These devices register the pass of the tracer wave in the river. Hence, for Rhodamine WT a change in fluorescence over time is obtained while for salt a change in conductivity is recorded. Then, both tracers' curves through calibration parameters are converted into concentration curves in time.

In this thesis TSI has been applied using salt. The distance between injection point and measurement point is the mixing length. According to Hudson & Fraser (2005a) a safe mixing length must be at least 10 times the channel width. The conductance curve should have a strong signal where the difference between the baseline and the peak conductivity should be 50-100 $\mu S/cm$. Besides, the peak must be less than the suggested sensitivity toxicity threshold: 400 $\mu S/cm$. The conductance curve should be smooth with no irregularities such as: double peaks or extended tails. In this research, during discharge and velocity measurements all the previous criteria was followed to ensure an adequate quality of the conductance curves.

Flow is measured using the mass balance criterion, where tracer mass conservation is applied (Hudson & Fraser, 2005b), Eq. (2.8) and (2.9). Velocity is calculated by dividing the reach length (Thalweg distance) and the time-of-travel (Curran & Wohl, 2003; MacFarlane & Wohl, 2003; Yochum, 2010). The time-of-travel can be obtained from one concentration or two concentration curves of the tracer.

$$Q = \frac{M}{\sum C_t \cdot t_{in}} \quad (2.8)$$

Where:

M tracer mass [M]

C_t Concentration [$M L^{-3}$]

t_{in} time interval [T]

$$C_t = (EC_t - EC_0) \cdot CF \quad (2.9)$$

EC_t Fluorescence or conductivity [$L^{-1}M^{-2}T^{-3}I^{-1}$]

EC_0 Natural fluorescence or conductivity in the water body

CF conversion factor to transform into concentration [-]

Different methodologies have been proposed to estimate the time-of-travel from the concentration curve, some detailed hereafter. The centroid time-of-travel consists of the time corresponding to the center of mass of the concentration curve (Figure 2.1), Eq. (2.10). Indeed, this methodology has been used with two concentration curves in different studies (Curran & Wohl, 2003; David et al., 2010; Lee & Ferguson, 2002). Even though David et al. (2010) considers this methodology as consistent, Zimmermann (2010) posits this methodology underestimate velocity. First arrival time-of-travel is the time when the concentration starts to increase, and peak time-of-travel corresponds to the time of peak concentration. These techniques are considered to vary with the reach length (Curran & Wohl, 2003), however the peak time-of-travel was used in the research of MacFarlane & Wohl (2003). According to Zimmerman (2010), the harmonic time-of-travel methodology provides better performance when a single probe is used. In addition, Waldon (2004) considers that the harmonic procedure is adequate when the factor to be determined in a relationship is in the denominator. Note that a wrong determination of travel time can affect the resistance prediction process.

$$t_c = \frac{\int_0^{\infty} t \cdot C(x,t) \cdot dt}{\int_0^{\infty} C(x,t) \cdot dt = I_x} \quad (2.10)$$

Where:

t Integration variable [T]

$C(x,t)$ Concentration at a certain point x at time t [$M L^{-3}$]

t_c Centroid traveling time [T]

$$t_H = \frac{1}{\int_0^{\infty} \frac{px(t) \cdot dt}{t}}; px(t) = \frac{C(x,t)}{I_x} \quad (2.11)$$

Where:

t_H Harmonic travel time [T]

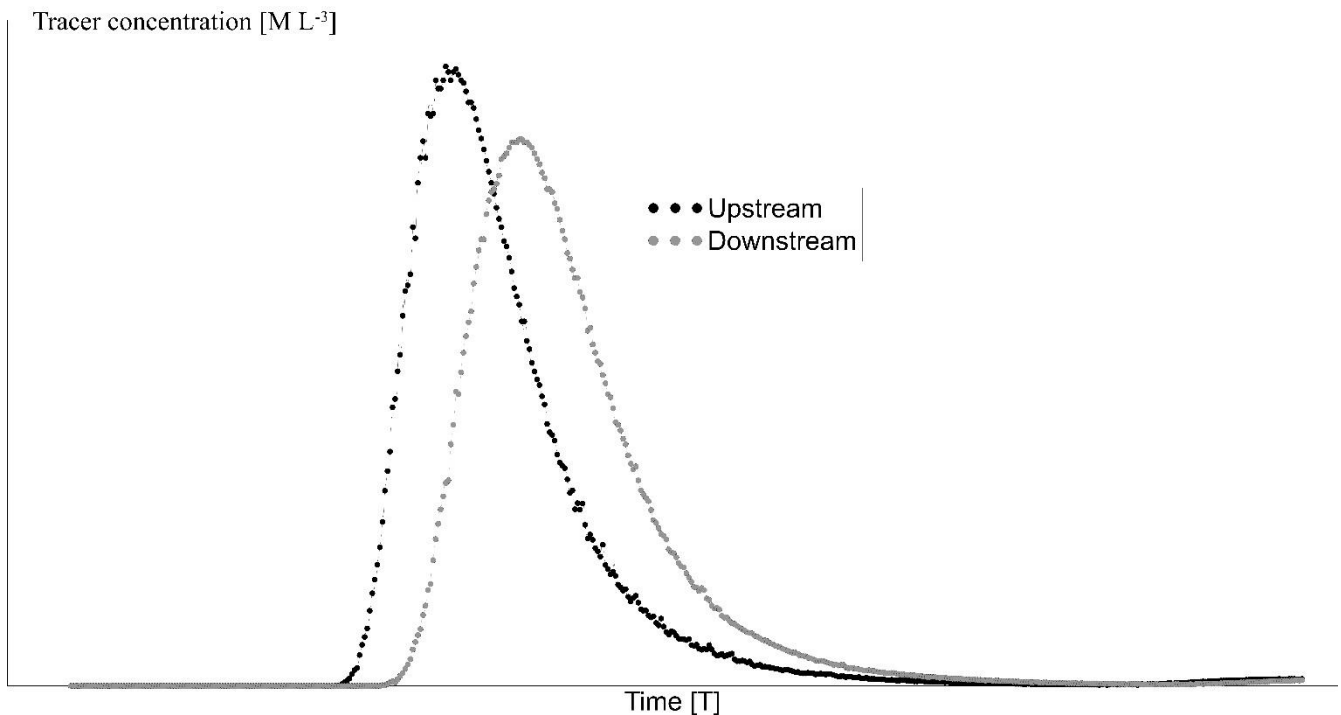


Figure 2.1: Conductance-time curves

The methodology to sample bed material is called pebble counting. In this methodology a particle is randomly picked from the riverbed and its intermediate axes is measured. Once a certain number of particles are sampled, a cumulative distribution function regarding to the bed size material is created and the percentiles of the bed material can be calculated (e.g. D_{84}) (Wolman, 1954).

The sampling process is based on a grid system where the reach is divided into transects in which a sample frame is used. There are several devices to measure the intermediate axes such as rulers, calipers, templates, or pebble box (Bunte & Abt, 2001).

According to the literature, the number of particles to be sampled varies according to the morphology under study. In a study reach containing riffle with pools or a boulder-cobble bed, 100 particles are sampled following the Wolman sampling technique (Bathurst, 1985, 2002; Marcus et al., 1992; Wolman, 1954), but if the study reach includes multiple bed forms such as plane bed, step-pool, and cascades the number of particles increase to 300 particles (David et al., 2010; Yochum, 2010). In step-pools, the Wolman method is applied for step-forming and pool-forming material which means to sample 100 particles from each one (Curran & Wohl, 2003; MacFarlane & Wohl, 2003). Note that an increase in the number of samples decreases the estimation error in the distribution of bed material. The precision-sample size relationship is not linear (Bunte & Abt, 2001).

A summary of diverse methodologies used to estimate different variables according to the literature is presented in Table 2.2.

Table 2.2: Field measurement methodologies

Reference	So range	Experiment Type	Velocity measurement methodology	Depth determination	Observations
(Jarrett, 1984)	0.2-4%	Natural	Current-meter	NA	Uniform flow conditions with straight reaches and minimal vegetation. 21 rivers. Flow range: 0.34-128.27 m ³ s ⁻¹ Velocity range: 0.27-2.64 m s ⁻¹
(Bathurst, 1985)	0.398-3.73	Flume and Natural	NA	For methodology which considers non-uniformity in the flow (velocity head gradient), depth was measure as a weighted average with the cross-section width	Most of the data has a relative submergence 0.43<d/D ₈₄ <7.1. Flow range: 0.14-0.19 m ³ s ⁻¹
(Bathurst, 2002)	0.1-5%	Natural	NA	Hydraulic radio	27 sites under ideal conditions with uniform and in bank flow
(Maxwell & Papanicolaou, 2001)	3-7 %	Flume	NA	NA	Flume experiment where natural sediment was obtained
(Lee & Ferguson, 2002)	3-18%	Natural	Reach averaged velocity and flow calculated with salt injection	Calculated through continuity Equation d=q/U	There is an error analysis. Flow error is determined through replication. There is an estimation of width error which influence other variables error such as d, R, (1/f) ^{1/2} . Flow range: 0.6-3.8 m ³ s ⁻¹ Velocity range: 0.7-2.1 m s ⁻¹
(Aberle & Smart, 2003)	Two profiles So=7.5% and So=2.1%	Flume	Velocity is measured by salt dilution	Once the velocity and width has been measured, depth is determined using the continuity Equation considering a rectangular cross-section.	Data covered d/D ₈₄ <5
(Curran & Wohl, 2003)	0.071-0.18 m m ⁻¹	Natural	Salt tracer injection	NA	Study oriented to determine the effect of Large Woody Debris in step-pools. f _{spill} is the left-over variable with an effect of 90% of total resistance. However, authors caution of these

					values due to f_{form} estimation.
(Wilcox et al., 2006)	0.05, 0.10, and 0.14 m m^{-1}	Flume	Reach averaged velocity calculated with salt injection	Calculated through continuity Equation $d=q/U$	The sensibility to the partitioning results is analyzed by using four methodologies to calculate grain, spill, and debris resistance. Flow range: 0.004-0.064 m^3s^{-1} Velocity range: 0.27-2.64 ms^{-1}
(Ferguson, 2007)	0.07-21%	Natural	Some of the data uses salt wave travel time	Continuity Equation, $d = \frac{q}{wU}$, Q and U determined by tracers	Between VPE and NDHG, NDHG follows the trend of the data over most of the range of data
(Comiti et al., 2007)	8% to 21%	Natural	Velocity is measured with salt dilution, with the lag between conductivity peaks	Once the velocity and width has been measured, depth is determined using the continuity equation considering a rectangular cross section.	Two analysis at-a-site to know how resistance is affected by relative submergence, channel slope and other variables. Between-site analysis to obtain field-based dimensionless Eq.s more reliable over a wide range of flow conditions. Flow range: 0.08-1.86 m^3/s Velocity range: 0.2-1.4 m/s
(Pagliara et al., 2008)	2.4-8.8%	Flume	NA	Evaluated from Manning	Test of resistance in long chutes using smooth lead spheres. Flow range: 0.001-0.04 m^3/s
(Comiti et al., 2009)	14%	Flume	Velocity is measured through salt injection and measurement with two conductivity probes	Calculated through continuity Equation $d=q/U$	During experiments skimming and nappe flow was tested as well as flow resistance partitioning. Flow range: 1-16 m^3/s
(Romero et al., 2010)	3 reaches per river: Lower zone 1.1-3% Intermediate zone 1.4-10.2% Upper zone 2.1-11.3%	Natural	NA	NA	Data taken from 5 rivers during dry season only. Reaches does not have vegetation. Flow range: 0.027-2.37 m^3/s

(Zimmermann, 2010)	3 to 23 %	Flume	Velocity is measured through salt injection and measurement with two conductivity probes	Continuity Equation with estimations of mean velocity	There is an analysis of uncertainty to know if the error between observed and predicted f is due to measurement uncertainties or unexplained error. Flow range: 0.001-0.009 m^3/s Velocity range: 0.2-1 m/s
(David et al., 2010)	0.017-0.195 m/m	Natural	Rhodamine WT dye tracer measured by fluorometer	LIDAR scans to calculate a reach average depth from multiple cross sections	In this study q^* have proved to represent relative grain submergence and differences in flow. Besides, in cascades there is close relation R/D_{84} with resistance implying dominance of grain resistance. In step-pools R/H explain a great proportion of resistance variability and indicates the submergence of steps. Flow range: 0.01-1.85 m^3/s Velocity range: 0.11-2.07 m/s
(Rickenmann & Recking, 2011)	0.004-24	Natural	Several methods	Two cases: 1) d is an input in the formulations 2) Q is used as input. Darcy-Weisbach and a certain resistance Equation are combined to obtain the hydraulic radius (R). R in narrow rivers is equal to depth (d)	Improve of the previous NDHG Eq. obtained by Ferguson (2007). Flow range: 0.01-1950 m^3/s Velocity range: 0.03-4.3 m/s
(Nitsche et al., 2012)	2-38%	Natural	Continuity Equation, Trace Travel time: Uranine and Sodium Chloride	The depth is solved from an equivalent cross-section using the measured flow and reach-averaged velocity.	Use of data from six stream reaches including plane-bed, cascade, and step-pool plus eight additional swiss mountain streams. Flow range: 0.0005-40 $m^3 s^{-1}$

(Cedillo et al., 2021a)	3.16-9.3	Natural	Trace Travel time: Sodium Chloride	Continuity Equation	Data from six reaches including: Two step-pools, three cascades, and one plane bed.
-------------------------	----------	---------	------------------------------------	---------------------	---

2.4.2 Measurement

In the process of measurement and estimation of resistance there are two sources of uncertainty, the first component is related to the assumptions assumed to the flow pattern called Data analysis and the second one associated to the uncertainty in the measurements themselves (Bathurst, 1985).

Data analysis considers the physical simplifications made in the presented mathematical formulation. As an illustration, Equation 2.4 is valid for uniform flow, an assumption that is generally not maintained in Mountain Rivers where the depth and slope of the water surface change from one section to another over time (Bathurst, 1985).

During the direct measurement of a physical quantity, that quantity has a possible range of values in which the value can oscillate (Eq. (2.12)) due to the uncertainty in measurement process. The sources of uncertainties can be classified and then quantified using the standard deviation, δX . Three sets of uncertainty are differentiated, which are due to: Resolution, Random, and Systematic errors.

Resolution error (δX_{res}) deals with instrument resolution uncertainty. When a quantity is measured an instrument only provides a value with a certain accuracy, so the true value can oscillate between a certain range which is the resolution. The measurement variation has a uniform probability distribution. The uncertainty due to resolution error according to Fornasini (2008) is given by Eq. (2.13).

Random errors (δX_{cas}) appear when repeated measurements of the same variable give different values due to parameters that act independently, simultaneously, and randomly. The distribution of random errors corresponds to a normal distribution of means for discrete data, Eq. (2.14).

Systematic error (δX_{sys}) are a constant deviation from all measurements and are produced, for example, by the lack of calibration of the measuring instrument. The distribution of systematic error depends on the available data.

Total uncertainty is the combination of Resolution and Systematic error or Random and Systematic error. Resolution and Random errors are not combined since are mutually exclusive (Fornasini, 2008). The combination is a quadratic sum Eq. (2.16).

$$X_O \pm \delta X \quad (2.12)$$

Where:

X_O : Central Value

δX : Uncertainty associated with the measure of a quantity X. It should contain two significant digits.

$$\delta X_{res} = \frac{\Delta X}{\sqrt{12}} \quad (2.13)$$

Where:

ΔX : In case of analog devices ΔX is the distance between instrument ticks, while for digital instruments is the unit value of the least significant digit.

$$\delta X_{cas} = \sqrt{\frac{1}{N(N-1)} \sum_{i=1}^N ((x_i - m^*)^2)} \quad (2.14)$$

Where:

N: Number of measurements taken

xi: measurement value

m*: average of the measurements (Eq. 2.15)

$$m^* = \frac{1}{N} \sum_{i=1}^N x_i \quad (2.15)$$

$$\delta X_{tot} = \sqrt{\sum (\delta X_i)^2} \quad (2.16)$$

The resistance is calculated using direct measurements of variables made in the field. Such measurements inherently carry on an error, which leads to an error in the calculation of resistance being quantified with the methodology called propagation of uncertainty. This procedure was used by Mrokowska, Rowiński, et al. (2015) to determine the uncertainty in shear velocity and by Mrokowska, Rowiński et al. (2015) for uncertainty in resistance for unsteady conditions. Thus, Darcy–Weisbach resistance parameter depends on R, Sf, and U (Eq. (2.4)) and its uncertainty is obtained with Eq. (2.17).

$$\delta f = \frac{\partial f}{\partial R} \cdot \delta R + \frac{\partial f}{\partial S_f} \cdot \delta S_f + \frac{\partial f}{\partial U} \cdot \delta U \quad (2.17)$$

Comiti et al. (2007) claims that error in geometry measurements has a significant effect on resistance in Mountain Rivers. The main source of uncertainty is in the depth measurement due to the disturbance produced when introducing the measurement instruments. In addition, the estimated error in measurement of distances and median axes is $\pm 1\%$ and $\pm 5\%$, respectively (Bathurst, 1985). The velocity and discharge have an uncertainty of $\pm 5\%$ when two probes to measure the salt wave were used. Moreover, for indirect measurements the corresponding uncertainties are: d:12%, R: 22%, and $\left(\frac{1}{f}\right)^{\frac{1}{2}}$: 17%.

Uncertainty affects the predictability test of empirical equations (Lee & Ferguson, 2002; Zimmermann, 2010). Indeed, it makes difficult to know whether the difference between measured and predicted resistance values is due to lack of predictivity of the equations or due to uncertainty of measurements. Furthermore, a known effect of uncertainty is to create dispersion between measured and predicted variables that determine the validity of adjusting the parameters of the law-flow (Lee & Ferguson, 2002; Zimmermann, 2010). Zimmermann (2010), implemented a methodology based on the parameters of Eq. 2.19.

$$U_{res} = U_{pred} - U_{meas} \quad (2.18)$$

Where:

U_{res} Residual values

U_{pred} Predicted value

U_{meas} Measure value

$$\delta_{U_{res}} = \delta_{U_{meas}} + \delta_{U_{pred}} + \delta_{U_{mean-bias}} \quad (2.19)$$

$\delta_{U_{res}}$ Cumulative error

$\delta_{U_{meas}}$ Uncertainty associated with measurement of variable U

$\delta_{U_{pred}}$ Uncertainty associated with prediction of variable U

$\delta_{U_{mean-bias}}$ Difference between mean U predicted and mean U measured

This methodology considers an unexplained difference between measured and predicted values when U_{res} is bigger than $\delta_{U_{res}}$.

2.5 Resistance coefficient evaluation

2.5.1 Methodologies

Different methods are useful to evaluate the resistance coefficient, more or less rigorous, with conceptual or empirical basis. The following are described, no desire to be exhaustive; Photography approach, Component Methods (Marcus et al., 1992), Tables (Yochum, 2010), and Empirical Equations (Zimmermann, 2010).

In Photography approach, a sequence of photographs describing the characteristics of the channel under study, such as slope and width, are related with a resistance value. This method questioned for its extreme simplicity; does not consider the variability of the resistance coefficient, highly dependent on flow, in Mountain Rivers (Marcus et al., 1992).

The tables present estimates for the components of a channel, such as the bed material and the floodplain. A value is provided within a certain range. Note that the precision of the method is questionable.

Component method is the decomposition of flow resistance into skin and form resistance components (Jarrett, 1985). Cowan developed a procedure, based on influencing factors, to estimate a resistance value. Six of them are highlighted as fundamental in Eq. (2.20).

$$n=(n_0+n_1+n_2+n_3+n_4) \cdot m \quad (2.20)$$

where: n_0 : base resistance, n_1 : cross section irregularities, n_2 : channel variation, n_3 : obstructions, n_4 : channel vegetation, and m : degree of meandering. Each component is determined from a table of values based on the reach description under study.

Empirical equations are mathematical expressions that relate flow resistance to certain geometric features or flow characteristics in a reach. Different types of mathematical expressions have been developed to predict resistance under specific conditions of flow and morphology, under the assumption of uniform flow and with different ways of measuring data (Aberle & Smart, 2003; Lee & Ferguson, 2002; Romero et al., 2010).

2.5.2 Resistance prediction Eq. types

There is not an agreement about how to relate flow resistance with bed characteristics in mountain rivers (Lee & Ferguson, 2002), so it was not surprised to find several types of equations to predict resistance parameter in a direct or indirect way.

Equations based on a logarithmic approaches, Eq. (2.21) depicts the general form of these equations coming from the boundary layer theory (Aberle & Smart, 2003). κ is the Von Karman constant usually take as 0.4 (Ferguson, 2007), however there is the need of calibration when applied for shallow rivers. The value of Br depends on cross- sections or relative submergence values (Aberle & Smart, 2003). A widely used version of these equations is Keulegan Equation obtaining by an integration of the semilogarithmic velocity profile through the flow depth (Ferguson, 2007; Lee & Ferguson, 2002). Keulegan formula is used as a measurement of grain resistance during flow resistance partitioning (Comiti et al., 2009; Wilcox & Wohl, 2006). k_s is the resistance depth which is usually a multiple of a bed material percentile $k_s=m \cdot D_{xx}$ (Wilcox & Wohl, 2006). Following this further, this type of Equation has provided unexpected good results in Lee & Ferguson (2002), a step-pool study, through the changing of k_s parameter where the best result was found with $k_s=step \cdot D_{50}$.

$$\sqrt{\frac{8}{f}} = \frac{1}{\kappa} \cdot \ln \left(\frac{d}{k_s} \right) + Br \quad (2.21)$$

Potential expression, Eq. (2.22) shows the general form of these Equations (Zimmermann, 2010). A special case of this expression is Manning-Strickler where the parameter b is $1/6$ (Ferguson, 2007). This type of Equations were not considered a good approximation for step-pools in Comiti et al. (2009).

$$\sqrt{\frac{g}{f}} = a \cdot \left(\frac{R}{k_s}\right)^b \quad (2.22)$$

Field techniques are equations which relate a flow resistance parameter with only a bed size percentile, so it is valid for skin resistance only (Marcus et al., 1992). Additionally, it is not expected to work well in step-pools considering the research of David et al. (2010) where there was no a single variable which provides a good flow resistance prediction in steep-pools.

Regime Equations, these expressions relate the resistance parameter with geometric characteristics of the reach. They can be used only for grain resistance calculation (Marcus et al., 1992). The Equation got by Jarrett (1984) (Eq. (2.23)) is an example obtained from a wide range of channel types.

$$n = 0.39 \cdot S_o^{0.38} \cdot R^{-0.16} \quad (2.23)$$

Non-Dimensional Hydraulic Geometry (NDHG), these Equations relate a non-dimensional velocity (U^* Eq.(2.25)) with a non-dimensional unitary flow parameter (q^* Eq.(2.26)) as is shown in Eq. (2.24) (Ferguson, 2007). Rickenmann & Recking (2011) did a variation of Eq. (2.24) where c_3 is equal to zero and effect of slope is taken into account in the modification of U^* (Eq. (2.28) and q^* (Eq. (2.27))). In Comiti et al. (2007), there is a direct relation of f and q^* (Eq. (2.29)) where the exponents are expected to change depending on the reach morphology. The upside of using these expressions is the not supposition of a velocity distribution or flow regime and for Eq. (2.24) there is no assumption of a resistance parameter (Zimmermann, 2010). Moreover, the term q^* is not affected by measuring data errors (Ferguson, 2007). In addition; q^* combined with S_o explain most of the variation of resistance variations so an expression containing both is expected to have good prediction capabilities (Comiti et al., 2007; David et al., 2010). Besides; for step-pool reaches q^* represents the flow regime for differentiation between nappe and skimming flow while for cascades, q^* describe better the f variability than relative submergence (David et al., 2010).

$$U^* = a^{c_1} q^{*c_2} S_o^{c_3} \quad (2.24)$$

$$U^* = \frac{U}{\sqrt{g D_{84}}} \quad (2.25)$$

$$q^* = \frac{q}{\sqrt{g D_{84}^3}} \quad (2.26)$$

$$q^{**} = \frac{q}{\sqrt{g S_o D_{84}^3}} \quad (2.27)$$

$$U^{**} = \frac{U}{\sqrt{g S_o D_{84}}} \quad (2.28)$$

$$f = -10.47 q^{*-1.13} S_o^{1.12} \quad (2.29)$$

Variable Power Equation (VPE) are obtained through the addition of Manning-Strickler formula and the Resistance Law, so the effects of deep water and shallow water are considered in one single expression. VPE limits, as relative submergence tends to infinite or zero, converges to Manning-Strickler formula or Resistance Law. This formulation (Eq. (2.30)) provides the best results in Ferguson (2007), following the tendency of resistance data as flow varies.

$$\left(\frac{8}{f}\right)^{\frac{1}{2}} = \frac{a_1 \cdot a_2 \cdot \frac{d}{D_{xx}}}{\sqrt{a_1^2 + a_2^2 \cdot \left(\frac{d}{D_{xx}}\right)^{\frac{5}{3}}}} \quad (2.30)$$

As seen above, there are different types of equations with different versions depending on the calibration data limiting the applicability. Those equations should be tested in new geographical regions where data is becoming available, for example the Andean region where only one study was found (Romero et al., 2010) and the regressions resulted in a simple logarithmic based Equation. Beyond that, at some places where the available data is scarce due to lack of funding, accessibility, or lack of required equipment limiting available data. Hence, the develop of correction factors for simpler expressions within a reasonable uncertainty seems needed. To conclude this analysis, Table 2.3 presents some resistance equations mentioned in the literature.

Table 2.3: Empirical Resistance Equations

Reference	Type of resistance	Resistance relation type
(Jarrett, 1984)	Grain-skin	$n=0.39 \cdot S_f^{0.38} R^{-0.16}$
(Bathurst, 1985)	Total resistance	$\left(\frac{8}{f}\right)^{1/2} = 5.62 \log\left(\frac{d}{D_{84}}\right) + 4$
(Bathurst, 2002)	Grain-skin	$\left(\frac{8}{f}\right)^{1/2} = 3.84 \left(\frac{d}{D_{84}}\right)^{0.547} \quad S_O \leq 0.8\%$
		$\left(\frac{8}{f}\right)^{1/2} = 3.1 \left(\frac{d}{D_{84}}\right)^{0.93} \quad S_O \geq 0.8\%$
(Maxwell & Papanicolaou, 2001)	Total resistance in step-pools	$\sqrt{\frac{8}{f}} = -3.73 \log\left(\frac{d_{\text{step}} D_{84}}{L d}\right) - 0.8$
(Lee & Ferguson, 2002)	Total resistance in step-pools	$\left(\frac{1}{f}\right)^{0.5} = 2.03 \cdot \log\left(12.2 \frac{R}{k_s}\right) \left(1 - 0.1 \frac{k_s}{R}\right)$ $k_s = \text{step } D_{50}$
(Aberle & Smart, 2003)	Total resistance in step pool	$\sqrt{\frac{8}{f}} = 0.91 \frac{d}{s}$
		Variable Power Eq.
		$\left(\frac{8}{f}\right)^{1/2} = \frac{a_1 a_2 (d/D_{84})}{[a_1^2 + a_2^2 (d/D_{84})^{5/3}]^{1/2}}$ $a_1: 6-7; a_2: 2.36$
		Nondimensional Hydraulic Geometry
(Ferguson, 2007)	Grain-skin	$U^* = a_1^{0.6} \cdot q^{*0.4} \cdot S^{0.3} \quad \text{Deep flow}$
		$U^* = a_2^{0.4} \cdot q^{*0.6} \cdot S^{0.2} \quad \text{Shallow Flow}$
		$U^* = \frac{U}{\sqrt{g D_{xx}}}$
		$q^* = \frac{q}{\sqrt{g D_{xx}^3}}$
(Comiti et al., 2007)	Total resistance in step pool and cascades	$f = 10.47 q^{*-1.13} S_O$

		$\left(\frac{g}{f}\right)^{1/2} = A + B \ln\left(\frac{d}{D_{84}}\right)$ $A = \varepsilon B$ $B = -7.82 S_O + 3.04$
(Pagliara et al., 2008)	Grain-skin	$\varepsilon = 1.4 \text{ if there is no boulders}$ $\varepsilon = 1.4 \cdot e^{-2.98 \Gamma} \text{ otherwise}$ $\Gamma = \frac{N_B \pi D_{xx}^2}{4 w L_{ij}}$
(Comiti et al., 2009)	Total resistance in step-pools	$U^* = 1.18 q^{*0.82} \text{ Nappe flow}$ $U^* = 1.1 q^{*0.38} \text{ Skimming flow}$ $U^* = 1.24 q^{*0.83} \text{ All data}$
(Romero et al., 2010)	Grain-skin	$f = 1.210 \ln(S_O) + 6.254$
(Zimmermann, 2010)	Total resistance in self formed cascades reaches	$U^* = 3.5 \left[q^{*0.55} S_O^{0.32} \frac{PL^{-0.14}}{w} \right]$ $U^{**} = 1.443 q^{**0.6} \left[1 + \left(\frac{q^{**}}{43.78} \right)^{0.8214} \right]^{-0.2435}$
(Rickenmann & Recking, 2011)	Total resistance	$U^{**} = \frac{U}{\sqrt{g S_f D_{84}}}$ $q^{**} = \frac{q}{\sqrt{g S_f D_{84}^3}}$

2.5.3 Use of D_{84} in resistance equations

There is an extensive use of D_{84} in resistance equations, for example as resistance length (Bathurst, 1985, 2002; Maxwell & Papanicolaou, 2001; Pagliara et al., 2008) or in Non-Dimensional Hydraulic Geometry equations where non-dimensional velocities and unitary flow use D_{84} (Comiti et al., 2007; Ferguson, 2007; Rickenmann & Recking, 2011). Moreover, the reason behind this widely use of D_{84} in resistance equations may be attributed to the research of Bathurst (1985). This study concludes D_{84} provides a three-dimensional view of the bed composition since is related with the percentage of cross section and bed area covered by projecting boulders. However, some studies have shown that D_{84} is not a good description of the bed material in step-pools. Aberle & Smart (2003) in a step-pool study found D_{84} is not representative of the height of the resistance layer since it cannot measure the vertical resistance extent or the irregular bed structure. Further, for step-pool there are other options instead of D_{84} such as s (standard deviation of bed elevations). Lee & Ferguson (2002) based on flume and field data in step-pool systems tested a logarithmic equation (Eq. (2.21) type). In this study, the resistance height was tested with different grain size percentiles and microtopographic parameters. The best result was found when $k_s = m \cdot \text{step } D_{50}$ where m has a variation between 1.6 to 2.6. Moreover, step D_{84} failed to consolidate all the resistance sources.

2.5.4 Resistance equations: error and requirements

The knowledge of the empirical resistance equation uncertainty is important since it allows to be concern of the possible resistance values and to be considered at any application. Jarrett (1984) regime equation based on slope and hydraulic radius have an average error of 28 %, which increases as the relative submergence decrease below 7. The error found by Bathurst (2002) to standard resistance equations is on average 30 %. The error is attributed to the focus on between-site variations and measurement difficulties. Furthermore, David et al. (2010) posits that due to different resistance components at different reaches the use of empirical resistance equations in other mountain reaches can reach an error of 66%.

A resistance equation must fulfill certain conditions to be consider as useful. It should contain easy to measure parameters, to be obtained from a wide range of flow data (Jarrett, 1984), to consider at-a-site as well as between-site variations (Bathurst, 2002). Moreover, David et al. (2010) states that resistance variability is better explained by a combination of control variables and the relation of those control variables changes as a function of the morphology.

An incorrect determination of resistance factor may lead to an incorrect determination of traveling time, mean velocity flow, and produce instability in one dimensional and two-dimensional models (Yochum, 2010).

2.6 Unsteady resistance

Until now resistance has been analyzed from a steady point of view. However; during the passing of a flood wave, resistance and the hydraulic behavior of the river has different patterns. The passing of a flood wave is unsteady flow requiring the use of 1-D flow “Saint-Venant” equations Mrokowska, Rowí, et al. (2015). Those equations are obtained by applying conservation of mass (“Continuity equation Eq.(2.32)”), and the Newton’s second law (“Momentum conservation equation Eq. (2.33)”) to a finite element. In Eq. (2.33) $\frac{\partial h}{\partial x}$ is the hydrostatic pressure term, $\frac{U}{g} \cdot \frac{\partial U}{\partial x}$ represents the advective acceleration, $\frac{1}{g} \cdot \frac{\partial U}{\partial t}$ is the local acceleration, $\frac{\partial z}{\partial x}$ represents the bed slope, and S_F is the friction slope (Mrokowska, Rowí, et al., 2015).

Under unsteady conditions, the friction slope S_F is obtained from the momentum equation (Eq. (33)). where each partial derivative is evaluated from measured data at different cross sections (Knight, 1981). Nevertheless, measurements has a high resolution in time but not in space, so the analysis of $\frac{\partial h}{\partial x}$ is complex. Mrokowska, Rowiński, et al. (2015) compare different differential quotients during the calculation of shear velocity in a flume experiment resulting a central difference quotient the most convenient way to estimate $\frac{\partial h}{\partial x}$. This approximation was used in Mrokowska, Rowí, et al. (2015) to estimate Manning coefficient , friction slope and shear velocity in order to know the viability of simplifications in momentum equation.

Depending on the wave, some terms of momentum equation (Eq. (2.33)) can be omitted, nevertheless according to Mrokowska, Rowí, et al. (2015) in upland rivers all the terms should be considered. Furthermore, Knight (1981) used the full set of Eq. (2.33) in an estuary to determine S_F and Darcy-Weisbach equation (Eq. 2.4) to determine f , in this research the surface slope is the dominant term.

Vegetation have shown to have influence in the resistance patterns. When experiments are carried out in a river or flume with an in-bank flow with no influence of vegetation, the resistance pattern consist on a descending parameter during the rising branch of the hydrogram followed by an ascension in the falling branch (Graf & Qu, 2004; Mrokowska, Rowí, et al., 2015). On the other hand, a different pattern was found in the field experiment developed by Sellin & van Beesten (2004) where there was low, bankfull, and overbank flow data in a compound channel with berm vegetation. Resistance was calculated using a single channel method where Manning resistance parameter is calculated in a nominal cross section. The resulting resistance patterns for a single flood wave pass change in comparison with the previous explained case. During the recession limb there is an increase in the discharge capacity which means a decrease of the resistance due to flattening of vegetation. Sellin & van Beesten (2004) also analyzed resistance patterns in a period of three months. The resistance for in-bank flow was characterize by a high frequency noise, while the resistance corresponding to rain generated flows producing flow in a compound channel has lower frequencies and irregular oscillations. In the former case there is a decrease of resistance value when dry period returns and the presence of a new resistance plateau.

The rating curve is the relation Discharge (Q)-Water Depth (d). Moreover; when uniform flow is used the energy gradient S_F is approximated with bed gradient S_0 , and the relation Q-d is unique. On the other hand, when S_F is

calculated with Saint-Venant Equation, the rating curve has loop shape (Graf & Qu, 2004). Besides, the loop shape has been observed during flume (Graf & Qu, 2004) as well as field measurements (Sellin & van Beesten, 2004) where its width indicates the importance of the pressure terms as well as inertia terms in the Saint-Venant Equations. Additionally, the presence or absence of sediment transport can alter the shape of the rating curve as well as its pattern (Graf & Qu, 2004).

Unsteady flow produces variations of resistance as hydrograph varies. Furthermore, there is data scarcity for this type of flow. Thus, it seems necessary to increase the unsteady experiments specially at field conditions. The patterns of resistance found will be of great importance to improve modelling prediction in the future.

$$d \cdot \frac{\partial U}{\partial x} + U \cdot \frac{\partial d}{\partial x} + \frac{\partial d}{\partial t} = 0 \quad (2.32)$$

$$\frac{1}{g} \cdot \frac{\partial U}{\partial t} + \frac{U}{g} \cdot \frac{\partial U}{\partial x} + \frac{\partial d}{\partial x} + \frac{\partial z}{\partial x} = -S_F \quad (2.33)$$

$$\frac{\partial d}{\partial x} = \frac{d2(t) - d1(t)}{2 \cdot \Delta x} \quad (2.34)$$

$$U = C \cdot \sqrt{R_h \cdot S_0} \quad (2.35)$$

$$U = C \cdot \sqrt{R_h \cdot \left(S_0 - \frac{1}{g} \cdot \frac{\partial U}{\partial t} - \frac{U}{g} \cdot \frac{\partial U}{\partial x} - \frac{\partial d}{\partial x} \right)} \quad (2.36)$$

2.7 Conclusions

In the current paper two aspects of resistance has been analyzed: resistance partitioning and resistance prediction. In resistance partitioning, an analysis of its application with the most common morphology found in rivers step-pools is used to illustrate the use of this methodology, then an analysis of its viability in mountain rivers is done. In resistance prediction, important aspects are treated such as different formulations, error, field methodologies to take data for prediction and measurement, and its uncertainty. Finally, some analysis of the unsteady case is done to illustrate the variation present in resistance when flood waves pass.

Mountain rivers has different characteristics than plain rivers such as shallow flows, with small relative submergence, on average subcritical flow and S-shape velocity profile. The most common morphologies are cascade, step-pool, and plane beds.

Resistance partitioning considers that total resistance is composed of additive linear components, but mountain bed material influences different resistance components with different proportions. In a flume experiment, where different resistance components were measured under different orders, the leftover component was the biggest since it contained the different resistance component interactions. Thus, resistance partitioning is an interesting methodology to have a partial idea of the contribution of resistance components, nevertheless depending on the applied methodology the results may differ and the unmeasured resistance components will be bigger (Wilcox & Wohl, 2006).

There are different empirical equations to predict resistance. Furthermore, the use of a certain resistance equation in a reach should be done with caution since it was obtained under different conditions having an error which can reach 66 %. These equations use D_{84} as resistance height. However, for step-pool case the use of a multiple of step D_{50} or standard deviation of bed (s) is more advisable to reflect the resistance bed structure. Hence, an adequate determination of the resistance height according to local conditions bed as well as flow conditions is necessary.

There is controversy about the approximation of S_F with S_0 or S_w . Some authors state the mountain rivers conditions do not produce an important difference of S_F with S_0 , but an error as high as 30% can be present. Indeed; before carrying out any simplification for S_F , it is necessary to check the kinetic energy gradient. In a

next step, a comparison of S_F and S_O should be done only then is possible to be sure the uncertainty introduced by any simplification.

Velocity measurements using tracers divide authors opinion since there are different methodologies which are applied in different studies. Thus, it seems interesting to compare different methodologies under different flow and bed conditions. The validation data will be obtained with other methodology such as current meter where possible.

Direct as well as indirect measurements should contain an uncertainty value. During comparison of resistance equation fitting, an uncertainty methodology should be applied to know if the lack of predictability of a certain equation is due to incapacity to follow the resistance pattern or uncertainty in its measurement or prediction. The highest uncertainty is introduced by water depth measurement according to the reviewed literature.

The resistance pattern during the pass of a flood wave depends on the presence or not of vegetation, and there are certain common patterns for in bank flow. Additionally, the energy gradient S_F under unsteady conditions is obtained through Saint-Venant equations, which means the field measurement of each component in the differential equation, nevertheless the resistance parameter uses relation for uniform flow since there is no a better approximation.

Chapter 3

3 Flow resistance prediction in headwater mountain streams morphologies

Redrafted from:

Cedillo, S., Sánchez-Cordero, E., Timbe, L., Samaniego, E., & Alvarado, A. (2021). Resistance Analysis of Morphologies in Headwater Mountain Streams. *Water*, 13(16), 2207. <https://doi.org/10.3390/w13162207>

Abstract: River flow velocity is determined by the energy available for flow motion and the energy fraction lost by flow resistance. We compared the performance of different equations for the Darcy-Weisbach resistance coefficient (f) and empirical equations to predict flow velocity. The set of equations was tested using data from the Quinuas headwater mountain river in the Andean region. The data was collected in three Cascades, two Step-pools, and one Plane-bed covering a wide range of velocity magnitudes. The results reveal that nondimensional hydraulic geometry equations (NDHG) with a Nash-Sutcliffe efficiency index (EF) varying from 0.6–0.85 provide the most accurate velocity prediction. Furthermore, the study proposes a methodology applicable to all morphologies for defining the NDHG parameters using easily measured field data. The results show an improvement in predictability with EF values in the range of 0.81–0.86. Moreover, the methodology was tested against data from the literature, which was not divided into morphologies providing EF values of around 0.9. The authors encourage the application of the presented methodology to other reaches to obtain additional data about the NDHG parameters. Our findings suggest that those parameters could be related to reach characteristics (e.g., certain characteristic grain size), and in that case, the methodology could be useful in ungauged streams.

Keywords: bed resistance; Cascade; mountain river; Plane-bed ; Step-pool; streams and rivers

3.1 Introduction

Prediction of the mean velocity in a river is important from a scientific and practical point of view. Nondimensional hydraulic geometry equations (NDHG) are capable of directly estimating the mean velocity but have parameters that vary according to the river morphology (Comiti et al., 2007). Indirect mean velocity estimation using the Manning, Chézy, or Darcy-Weisbach equations is also common. Predictive empirical equations (PEEs) are focused mainly on the prediction of the Darcy–Weisbach (f) dimensionless resistance parameter, which has a physical meaning. However, PEEs face several challenges in mountain rivers. First, each PEE is derived under different flow conditions and river morphologies, using different measuring techniques (Aberle & Smart, 2003). Second, mountain river characteristics such as steep slopes (bed slope (S_0) greater than 0.2%) (Papanicolaou et al., 2004), an average depth comparable to bed material size (Ferguson, 2007), and a coarse, poorly sorted clast (Bathurst, 2002) result in resistance patterns that differ from plane rivers. Third, mountain river morphologies such as Step-pools (Chin & Wohl, 2005; Curran & Wohl, 2003; David et al., 2010; MacFarlane & Wohl, 2003), Cascades (Montgomery & Buffington, 1997; Nitsche et al., 2012), and Plane-beds (David et al., 2010) add complexity to resistance analysis as each morphology possesses different resistance characteristics. Authors have estimated PEE uncertainties of 30% (Bathurst, 2002) and 66% (David et al., 2010) in mountain rivers. Hence, an analysis of PEE for mountain streams under different flow, geographical, and dissipative conditions is needed to improve velocity estimation approaches.

Nondimensional hydraulic geometry equations (NDHG) relate dimensionless velocity to dimensionless unitary flow (U^*-q^* or $U^{**}-q^{**}$), providing a direct estimation of velocity. Ferguson (2007) obtained this expression when bed shear stress and the generalized power law were related by the term $(8/f)^{0.5}$ to produce a U^*-q^* expression. Rickenmann & Recking (2011) modified U^* and q^* by adding the energy slope, resulting in $U^{**}-q^{**}$. These variables were found by Nitsche et al. (2012) in applying a dimensional analysis. NDHG equations have been successfully calibrated in different experiments. Comiti et al. (2007) used 177 velocities and flow resistance data from Cascades and Step-pools. Comiti et al. (2009) developed a flume study investigating the resistance at the nappe and skimming flow in Step-pools. Zimmermann (2010) conducted 31 experiments in a flume for Cascades. Nitsche et al. (2012) used data from the Swiss Alps in Plane-bed/riffle, Step-pool, and Cascade morphologies; they found a prefactor for the relation $U^{**}-q^{**}$ that depends on the boulder concentration. The NDHGs cited in the literature possess different parameters; some NDHGs differ in equation structure, which limits their applicability.

Studies around the world have yielded several types of PEEs. Jarrett (1984) used discharge data at 21 reaches with uniform flow and minimal vegetation in the Rocky Mountains of Colorado to study different reach conditions. After several regressions, the resulting equation expressed n proportional to S_F (Energy Slope) and R (Hydraulic Radius). Bathurst (1985) found a semilogarithmic relation $((8/f)^{0.5} = f(\log(d/D_{84}))$; d : mean water depth and D_{84} : 84th percentile of the grain-size distribution) for the resistance parameter using measured data in upland British rivers, data from previous studies, and flume data. Bathurst (2002) used data from the literature with uniform flow and a certain range of flows, slopes, and bed material from the United Kingdom, the US, and the Czech Republic. These data were used to calibrate two exponential equations for resistance depending on the reach slope. Maxwell & Papanicolaou (2001) performed a flume experiment with a natural river gravel bed, producing a semilogarithmic equation for resistance prediction in Step-pools. Lee & Ferguson (2002) studied resistance in Step-pools using field and flume data. Field data were collected at sites meeting certain slope range, grain size, accessibility, and morphology requirements. A semilogarithmic equation was obtained, but the best option for resistance length was D_{50} of the step material. Aberle & Smart (2003) conducted a flume experiment investigating the resistance in Step-pools. They found that the standard deviation of bed elevation (s standard deviation of residuals between the linear trend of bed elevation and the bed elevation) is a better representation of resistance height in an exponential equation. Ferguson (2007) based his analysis on data from riffles, runs, Step-pools, and pool-riffles in the UK, the US, New Zealand, and Italy to calibrate a variable power equation for shallow and deep flows. Romero et al. (2010) derived a logarithmic relation for resistance depending on the riverbed slope using data from five rivers in Bolivia. According to Wohl (2013), there is not a best empirical equation to predict the resistance parameter in mountain rivers because the characteristics of mountain rivers make it difficult to estimate resistance.

This study tested the performance of eleven empirical resistance equations with the objective of mimicking the measured velocity for the most common morphologies at the headwater of an Andean Mountain river. The applied approach guaranteed interpretation of the suitability of each equation for three morphologies: Cascade, Step-pool, and Plane-bed. The test showed that NDHG equations are the best option for all morphologies. The novelty of this study lies in the development of a methodology that enables the derivation of NDHG equation parameters through regression analysis. The proposed approach improves the estimation of velocity, resistance parameters, and traveling time in mountain rivers.

3.2 Materials and methods

3.2.1. River reach

For this study, experimental data were collected from a 1500 m longitudinal section in the headwaters of the Quinuas river (Figure 3.1), located in the province of Azuay, Ecuador. The river section is situated between 0 + 000 at 3664.4 masl and 1 + 431.13 at 3605.77 masl, with a mean slope of 4%. This reach was selected given the relatively large variation in river morphology consisting of three Cascades, two Step-pools, and one Plane-bed. Table 3.1 presents pictures and schemes of each morphology to illustrate its bed characteristics. The geometric characteristics of each morphology are presented in Table 3.2. The reach length was measured along the thalweg; the bed slope (S_0) for each morphology was obtained through linear regression of thalweg points.

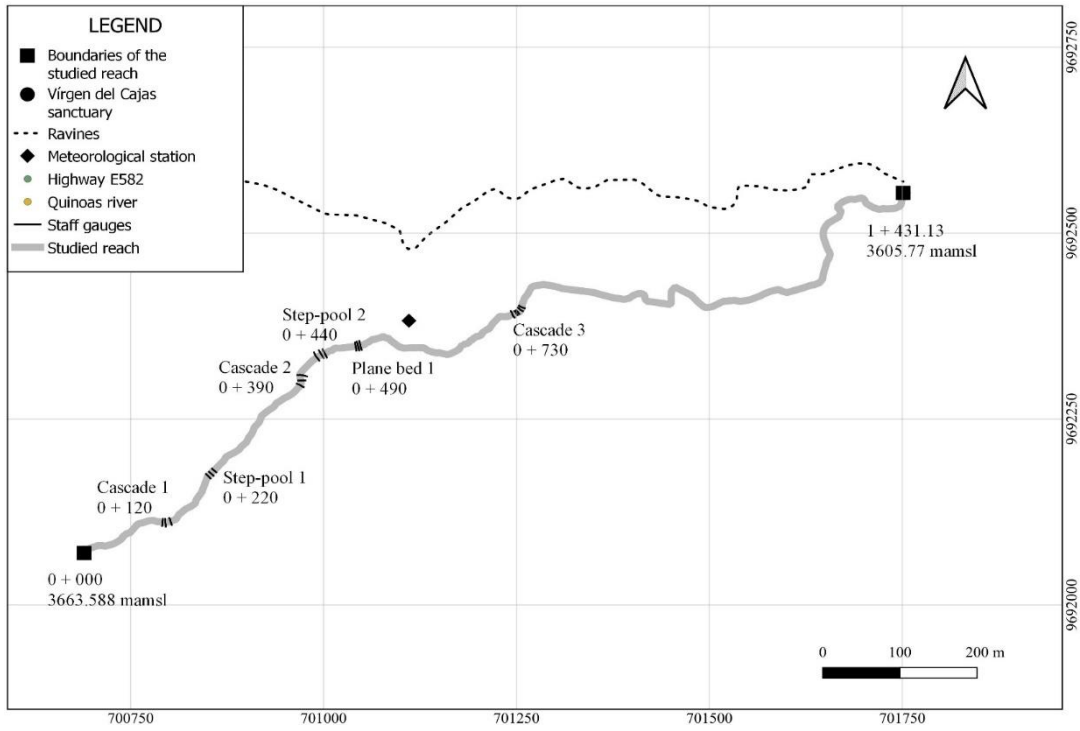


Figure 3.1: Plan view of the studied 1500 km river reach showing the sequence of the sub-reaches and the location of the meteorological station.

Table 3.1: Longitudinal profiles and pictures of Cascade, Step-pool, and Plane-bed.

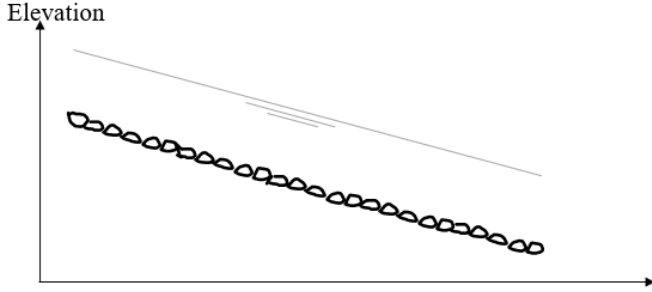

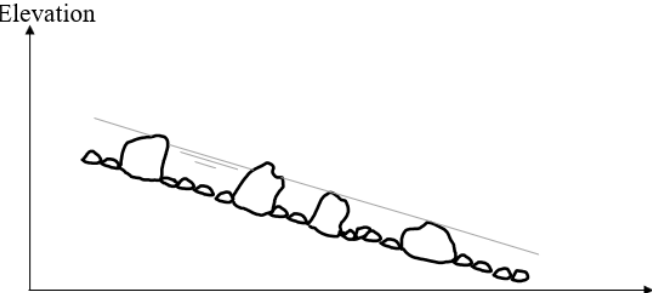

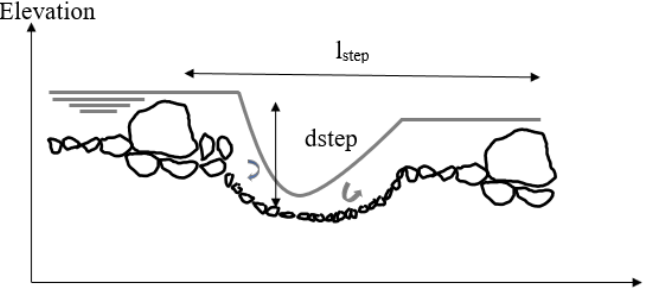

Profile	Picture
<p data-bbox="360 320 475 349">Plain bed</p>  <p data-bbox="379 663 608 692">Downstream Distance</p>	
<p data-bbox="373 772 466 801"><i>Cascade</i></p>  <p data-bbox="373 1111 608 1140">Downstream Distance</p>	
<p data-bbox="368 1216 470 1245"><i>Step-pool</i></p>  <p data-bbox="368 1554 603 1583">Downstream Distance</p>	

Table 3.2: Average geometry characteristics of the studied reaches.

Reach	Length (m)	So (%)	$s_{\Delta z}$ (m) ¹	s (m) ²	k_3 (m) ³	d_{step} (m) ⁴	l_{step} (m) ⁴	Measured Manning Range
Cascade 1	11.95	8.82%	0.041	0.022	0.287			0.120–0.264
Step-pool 1	12.22	6.10%	0.288	0.177	0.435	0.491	6.61	0.108–0.414
Cascade 2	14.58	9.30%	0.282	0.179	1.299			0.139–0.510
Step-pool 2	11.82	8.08%	0.197	0.107	0.336	0.442	3.49	0.178–0.472
Plane-bed 1	6.26	3.16%	0.039	0.017	0.197			0.036–0.242
Cascade 3	18.08	8.50%	0.427	0.214	0.474			0.142–0.456

¹ $s_{\Delta z}$ is the standard deviation of the difference between consecutive thalweg points. Adapted from Lee & Ferguson (2002).

² s is the standard deviation of residuals between the linear trend of bed elevation and the corresponding bed elevation points Lee & Ferguson (2002).

³ k_3 is the average of the maximum difference of each consecutive triplet of points in the thalweg. Adapted from Lee & Ferguson (2002).

⁴ d_{step} and l_{step} represent the height and spacing of the steps in the Step-pool morphologies, respectively. See illustration in Table 3.1 (Curran & Wohl, 2003).

The river cross-section (XS) in the reaches without abundant vegetation was measured with a differential GPS Trimble® R6 instrument; in reaches with abundant trees, a total station Sokkia® 550 RX was used. The average geometry of each reach was calculated from three XSs, as shown in Table 3.2, except for Cascade 3, where the reach was divided into five XSs. The wetted width (w) at each cross-section was estimated with a measuring tape, excluding the width of the boulders stretching above the water level. The average depth (d) at each XS was computed using the continuity equation assuming a rectangular XS (Eq. (3.1)). These values were averaged per reach to yield a weighted average water depth (Aberle & Smart, 2003).

$$Q=U A=U w d \quad (3.1)$$

where Q is the discharge ($m^3 s^{-1}$), U is the mean flow velocity ($m s^{-1}$), A is the XS area below the water surface (m^2), w is the wetted width at the water surface (m), and d is the mean water depth (m).

The resistance parameter was estimated using field measurements of discharge, velocity, and energy slope. The discharge was measured using the dilution-gauging method because in small streams, especially in low-flow conditions, measuring flow using the standard wading rod method is difficult and inaccurate. The dilution-gauging method is based on measuring the dilution of a known volume of conservative salt tracer (Hudson & Fraser, 2005a). NaCl was used for its low cost and wide use in small river studies (Curran & Wohl, 2003; MacFarlane & Wohl, 2003; Moore, 2005; Wilcox & Wohl, 2006). Velocity was evaluated through the reach length and the subtraction of time-of-travel from conductance curves read upstream and downstream of the reach. Two HOBO U24-00 freshwater conductivity data loggers with a resolution time of 1.0 s were placed upstream and downstream of the reach. The traveling time of each conductance curve was calculated using the harmonic method (Nitsche et al., 2012). Energy slope (S_F) was estimated as the water surface slope (S_w) (Bathurst, 1986; David et al., 2010). Pebbles were counted to estimate bed material distribution (Bunte & Abt, 2001). The number of sampled elements was 400 for each reach. Data were taken at flow magnitudes from $0.03 m^3 s^{-1}$ to almost $1 m^3 s^{-1}$. During that flow range, there was in-bank flow. However, only for the highest flow reaches such as Plane-bed and Step-pool received bank full flow. The Cascades did not reach bank full flow because of its high slope. Table 3.2 depicts the range of Manning's coefficient measured at each studied reach. Hence, the data range presents a complete overview of different velocity magnitudes, which are closely related to the resistance characteristics. The resistance parameter used in this study is the Darcy-Weisbach resistance

coefficient (f); most literature from the last three decades has used this parameter given its physical interpretation and dimensionless units (Ferguson, 2007). f is estimated with Equation (3.2).

$$(8/f)^{0.5} = U / (g R S_f)^{0.5} \quad (3.2)$$

where g is the gravitational acceleration ($m s^{-2}$), R represents the hydraulic radius (m), S_f is the energy slope, and U is the velocity ($m s^{-1}$).

3.2.2. Empirical resistance equations

The equations tested for velocity prediction are listed in Table 3.3. Most of the equations estimate the resistance parameter as $(8/f)^{1/2}$. The velocity was computed using Equation (3.2). Estimations of NDHG equations derive flow velocity through the following steps: (1) Estimation of dimensionless unitary flow; (2) estimation of dimensionless velocity with the NDHG equation; (3) velocity estimation with the dimensionless unitary velocity definition.

Table 3.3: Resistance equations tested in this chapter.

Reference	Code	Type of Resistance	Equation
(Bathurst, 1985)	BA1985	Total resistance	$(8/f)^{0.5} = 5.62 \log(d/D_{84}) + 4$ <p>D_{84} corresponds to the 84th percentile of the grain-size distribution.</p> <p>d is the mean water depth</p>
(Bathurst, 2002)	BA2002	Grain-skin	$(8/f)^{0.5} = 3.84 (d/D_{84})^{0.547}; S_0 \leq 0.8\%$ $(8/f)^{0.5} = 3.1 (d/D_{84})^{0.93}; S_0 \geq 0.8\%$ <p>S_0 is bed slope</p>
(Maxwell & Papanicolaou, 2001)	MaPa2002	Total resistance in Step-pool	$(8/f)^{0.5} = -3.73 \log\left(\frac{d_{step} D_{84}}{l_{step} d}\right) - 0.8$
(Lee & Ferguson, 2002)	LF2002	Total resistance in Step-pool	$(1/f)^{0.5} = 2.03 \log(12.2R / k_s)(1 - 0.1k_s/R)$ <p>$k_s = D_5, D_{16}, D_{25}, D_{50}, D_{75}, D_{84}, D_{95}, S, S_{\Delta z}, k_3, l_{step}, d_{step}$</p> <p>$D_{xx}$ corresponds to the xxth percentile of the grain-size distribution.</p> <p>$s, S_{\Delta z}, k_3, l_{step}$, and d_{step} has been define in Table 3.1 and Table 3.2</p>
(Aberle & Smart, 2003)	AbSm2003	Total resistance in Step-pool	$(8/f)^{0.5} = 0.91 d/s$
(Ferguson, 2007)	(a) FeVPE2007 (b) FeNHGE2007	Grain-skin	<p>(a) Variable Power Equation</p> $(8/f)^{0.5} = [c_1 c_2 (d/D_{84})] / [c_1^2 + c_2^2 (d/D_{84})^{5/3}]^{0.5}$ <p>$c_1: 6 - 7; c_2: 2.36$</p> <p>(b) Nondimensional Hydraulic Geometry</p> <p>Deep flow:</p> $U^* = a_1^{0.6} q^{*0.4} S_f^{0.3}$ <p>Shallow Flow:</p>

			$U^* = a_2^{0.4} q^{*0.6} S_f^{0.2}$ $U^* \text{ and } q^*:$ $U^* = U/(gD_{xx})^{0.5}$ $q^* = q/(gD_{xx}^3)^{0.5}; D_{xx}=D_{84}$
(Comiti et al., 2007)	Co2007	Total resistance in Step-pool and Cascade	$f = 10.47q^{*-1.13} S_0$
(Comiti et al., 2009)	Co2009	Total resistance in Step-pool	$U^* = 1.18q^{*0.82} \text{ Nappe flow}$ $U^* = 1.1q^{*0.38} \text{ Skimming flow}$ $U^* = 1.24q^{*0.83} \text{ All data}$ $U^* \text{ and } q^*:$ $U^* = U/(g D_{xx})^{0.5}$ $q^* = q/(g D_{xx}^3)^{0.5}; D_{xx}=D_{84}$
(Romero et al., 2010)	Ro2010	Grain-skin	$f = 1.210\ln(S_0) + 6.254$
(Zimmermann, 2010)	(1) Zi12010 (2) Zi22010	Total resistance in self-formed Cascade reaches	$(1) U^* = 1.45q^{*0.55} S_0^{0.32}$ $(2) U^* = 3.5[q^{*0.55} S_0^{0.32} 1_{\text{step}}^{-0.14} / w]$ $U^* \text{ and } q^*:$ $U^* = U/(g D_{xx})^{0.5}$ $q^* = q/(g D_{xx}^3)^{0.5}; D_{xx}=D_{84}$ <p>w is water surface width</p>
(Rickenmann & Recking, 2011)	RiRe2011	Total resistance	$U^{**} = 1.443q^{**0.6} [1 + (q^{**}/43.78)^{0.8214}]^{-0.2435}$ $U^{**} = U/(gS_f D_{84})^{0.5}$ $q^{**} = q/(gS_f D_{84}^3)^{0.5}$

3.2.3. Statistical performance metrics

Generally, statistical metrics provide information about a single aspect or projection of the model error. Thus, it is advisable to use a combination of metrics to assess the overall model performance (Chai & Draxler, 2014). In this study, six metrics were selected: the root mean square error (RMSE), a qualitative methodology in which larger model errors have more weight than smaller ones (Chai & Draxler, 2014; Willmott & Matsuura, 2005); the logarithm of RMSE to determine the model prediction capacity for low values (Ferguson, 2007); the prediction errors (PE) counting the number of predicted values that are greater than twice or less than half as large as the observed values (Ferguson, 2007); the average standard error of estimation (S_x), which gives the mean percentage of the model error relative to the observations (Romero et al., 2010); the Nash–Sutcliffe efficiency index (EF), a metric widely used to determine the model goodness-of-fit with flexibility and reliability (McCuen et al., 2006; Merz & Blöschl, 2004; Nayak et al., 2013); the mean average error (MAE) considered by (Willmott & Matsuura, 2005) is a better indicator of the average error than RMSE. Ritter & Muñoz-Carpena (2013) provided a table with a range of EF values, a useful tool for interpreting the score of the model goodness-of-fit.

RMSE and MAE are transformed into a relative version for some analyses. Hence, these two metrics are divided by the average of the observed values and multiplied by 100 to obtain a percentage.

3.2.4. Determination of NDHG parameters

In this research, a methodology to determine the NDHG equation parameters is proposed. The Rickenmann & Recking (2011) dimensionless velocity (Eq. (3.4)) and unitary flow (Eq. (3.5)) obtained by Nitsche et al. (2012) in the dimensional analysis are used in this process. The form presented in Eq. (3.3) was selected for the methodology development.

$$U^{**} = a_1 q^{**a_2} S_f^{a_3} \quad (3.3)$$

$$q^{**} = q / (g S_f D_{84}^3)^{0.5} \quad (3.4)$$

$$U^{**} = U / (g S_f D_{84})^{0.5} \quad (3.5)$$

where q ($m^2 s^{-1}$) is the unitary flow ($q = Q w^{-1}$) and D_{84} (m) corresponds to the 84th percentile of the grain-size distribution.

Eq. (3.3) was linearized through the application of logarithms:

$$\log(U^{**}) = \log(a_1) + a_3 \log(S_f) + a_2 \log(q^{**}) \quad (3.6)$$

Eq. (3.6) resembles the equation of a line:

$$y = m x + a \quad (3.7)$$

where the parameters m and a are related to Eq. (3.6) and expressed as Eqs. (3.8) and (3.9):

$$m = a_2 \quad (3.8)$$

$$a = \log(a_1) + a_3 \log(S_f) \quad (3.9)$$

where \mathbf{m} and \mathbf{a} are values from the linear regression of U^{**} and q^{**} . However, there are two equations with three unknowns in the system to be solved. An additional equation, Eq. (3.10), was obtained from Ferguson (2007), who used the generalized power law and the bed shear stress.

$$U/U_* = c(d/D_{xx})^b \quad (3.10)$$

where U_* is the shear velocity ($m s^{-1}$) and D_{xx} is a characteristic grain size (m) taken here as D_{84} ; c and b are constant parameters.

In Eq. (3.10), U_* and d are replaced with their definitions. After a mathematical process, Eq. (3.11) is obtained, which is the same obtained by Ferguson (2007). This equation contains parameter m_0 , defined in Eq. (3.12).

$$U^{**} = c^{1-m_0} S_f^{(1-m_0)/2} q^{**m_0} \quad (3.11)$$

$$m_0 = (2b + 1)/(2b + 3) \quad (3.12)$$

Combining Eqs. (3.8), (3.9), and (3.11), we derived the parameters in Eq. (3.3). Eqs (3.13)–(3.15), are expressed as

$$m = a_2 = m_0 \quad (3.13)$$

Thus, the slope m of the regression is equal to m_0 .

$$a_3 = (1 - m)/2 \quad (3.14)$$

$$a_1 = 10^a / S_f^{a_3} \quad (3.15)$$

3.2.5. Variance decomposition methodology (VDM)

VDM decomposes the variance of the total error, as shown in Eq. (3.17). The variance of the total error increases as the model output increases. To obtain a constant variance independent of the model output magnitude, a Box–Cox transformation was applied.

Both observed and predicted values of velocity are transformed using Equation (3.16). λ is calibrated through the minimization of the variance of the error of the transformed predicted and measured velocities. The resulting lowest variance is taken as the total residual error variance in Eq. (3.17). The observation error variance for velocity is based on an error of 5% obtained by Lee & Ferguson (2002).

$$B(Y) = (Y^\lambda - 1)/\lambda \quad (16)$$

$$S_e^2_Y = S_e^2_{Y-Y_o} - S_e^2_{Y_o} \quad (17)$$

where Y is the model output variable, S is the standard deviation, $S_e^2_{Y-Y_o}$ is the total residual error variance, $S_e^2_Y$ is the model error variance, and $S_e^2_{Y_o}$ is the observation error variance.

3.2.6. Test with data from literature

An additional performance test was developed using data available from the literature. Jarrett (1984) provides data from 21 reaches in the Rocky Mountains of Colorado. However, data from two reaches could not be used because D_{84} data was not available. Bathurst (1985) presents data from 16 British rivers. Both data sets were joined comprising 121 measurements with flows ranging from 0.137 to 129 $m^3 s^{-1}$, for this data set the morphology of each reach was not specified.

The proposed methodology used 50% of the data randomly chosen to estimate a_1 , a_2 , and a_3 (Figure 3.2) and predict U^{**} with the remaining 50% of the data. Moreover, Zimmermann (2010), the best fitting equation for Cascade and Step-pool, was used to predict the same data. In this equation, instead of using S_o , S_F was used since this parameter was provided in the dataset.

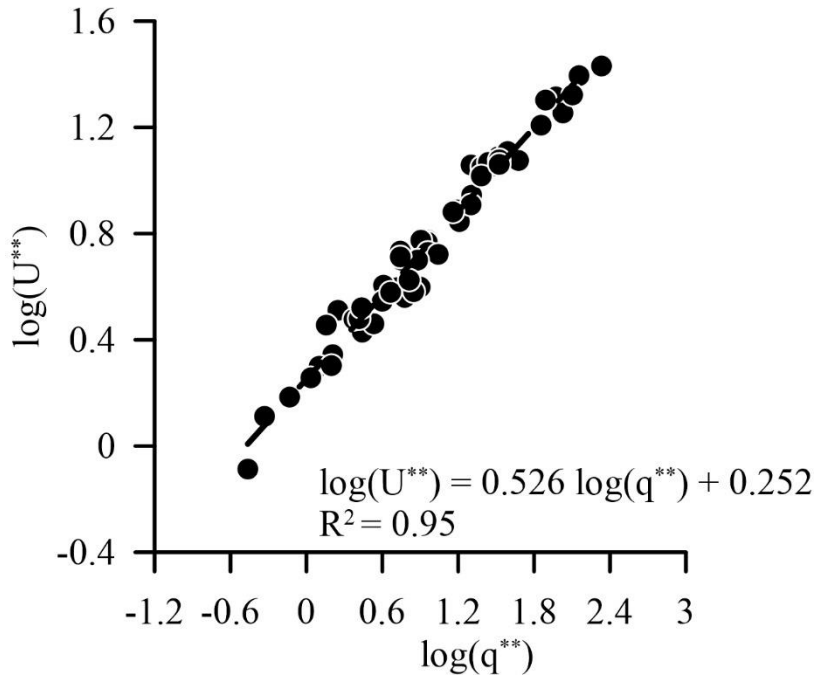


Figure 3.2: Linear regression of Eq. (3.3) for 50% of the data provided in (Jarrett, 1984) and (Bathurst, 1985) randomly chosen.

3.3 Results

3.3.1 Best fitting equation

The performance of the empirical equations listed in Table 3.3 was compared with the measured velocities in the Cascades, Step-pools, and Plane-bed. Table 3.4 presents the NDHG equations with the best fitting properties for the Cascade, Step-pool, and Plane-bed river reaches. For Cascades and Step-pools, the Zi12010 equation (Zimmermann, 2010) is the best; for the Plane-bed, the Co2009 equation (Comiti et al., 2009) performs best, except for the S_x metric for which the FeNHGE2007 (Ferguson, 2007) fits best.

Table 3.4: Statistical fitting metrics for Cascade, Step-pool, and Plane-bed morphologies.

Morphology	Name	RMSE	RMSElog	PE	S_x	MAE	EF
Cascade	Zi12010	0.061	0.066	0	16.761	0.046	0.834
	FeNHGE2007	0.102	0.099	0	26.936	0.078	0.536
	Co2007	0.104	0.127	1	25.546	0.078	0.514
Step-pool	Zi12010	0.085	0.096	0	26.582	0.062	0.731
	FeNHGE2007	0.137	0.132	1	39.106	0.102	0.294
	RiRe2011	0.141	0.137	1	40.786	0.107	0.253
Plane-bed	Co2009	0.153	0.102	0	28.914	0.108	0.631
	FeNHGE2007	0.162	0.116	0	23.485	0.122	0.585
	RiRe2011	0.164	0.117	0	23.719	0.123	0.577

The metrics indicate that performance depends on the morphology. For Cascades, the Zi12010 prediction performs well according to (Ritter & Muñoz-Carpena, 2013). The relative RMSE and MAE are similar, 16% and 12%, respectively. For Step-pools, Zi12010 performs acceptably. The difference between relative RMSE (23%) and MAE (17%) is the same as for Cascades, approximately 5%, indicating that there are no significant differences between residual magnitudes for these morphologies. For the Plane-bed, Co2009 demonstrated unsatisfactory performance, with a higher difference between relative RMSE (30%) and MAE (21%) than for Cascades and Step-pools, indicating higher residual values than for the other morphologies. The best equations for all morphologies do not have cases with predicted and observed values (PE) that differ by a factor greater than two or less than 0.5. The model error relative to the observed value (S_x) illustrates that for a Plane-bed the best equation is FeNHGE2007. The Co2009 equation omits S_F , and FeNHGE2007 includes S_F . The morphology with the lowest model error relative to the observed value is Cascade (17%); Step-pool and Plane-bed have similar values (approximately 25%).

3.3.2. Estimation of NDHG Parameters

Implementation of the proposed methodology to calculate the NDHG exponents first requires a check that $\log(q^{**})-\log(U^{**})$ follows a linear trend. Figure 3.3 indicates a linear tendency for all of the morphologies, with a coefficient of determination (R^2) greater than 0.85 for all fittings, although the slope m and the independent factor a vary considerably between the studied morphologies.

The estimated coefficients of NDHG for each morphology are presented in Table 3.5. Parameter a_1 varies from 1.73–2.31; the value range of parameter a_2 depends on the morphology and is 0.75 for the Plane-bed, considerably higher for Cascades and Step-pools (0.48–0.57). The opposite is true for a_3 ; the Plane-bed value (0.12) is less than the values for Cascades and Step-pools (0.21–0.26).

Table 3.5: NDHG exponents based on the proposed methodology.

Morphology	m	a	S_0	a_1	a_2	a_3	a_2/a_3
Cascade 1	0.478	0.089	0.088	2.31	0.48	0.26	1.83
Cascade 2	0.590	0.034	0.093	1.76	0.59	0.21	2.88
Cascade 3	0.569	0.056	0.085	1.94	0.57	0.22	2.64
Plane-bed 1	0.751	0.185	0.032	2.36	0.75	0.12	6.02
Step-pool 1	0.565	0.064	0.061	2.13	0.57	0.22	2.60
Step-pool 2	0.531	-0.019	0.081	1.73	0.53	0.23	2.26

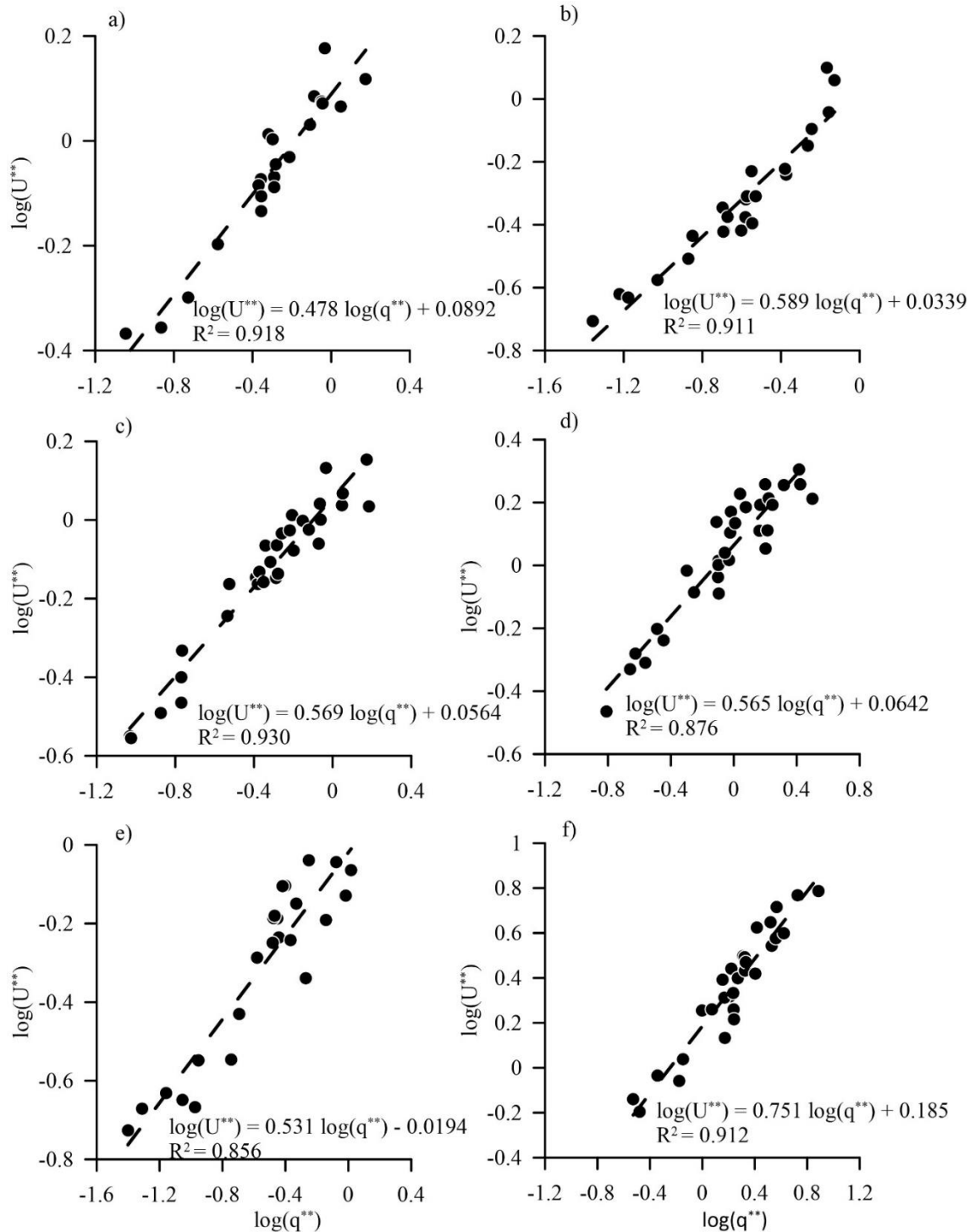


Figure 3.3: Linear regression of Equation (3): (a) Cascade 1; (b) Cascade 2; (c) Cascade 3; (d) Step-pool 1; (e) Step-pool 2; (f) Plane-bed.

Table 3.6 shows the performance metrics of the NDHG equations according to the proposed methodology (NDHGCA, NDHGSP, and NDHGPB). Comparison of Table 3.4 and Table 3.6 reveals that the proposed approach produces improved quality metrics. The derived equations demonstrate good performance according to the EF metrics. The difference between relative RMSE and MAE has been reduced to 4.6% on average for all morphologies; the residual magnitudes are uniform. The model error relative to the observed values decreases significantly for Step-pool and Plane-bed morphologies; the improvement in the Cascade morphology is less evident. PE illustrates that the proposed NDHG equations did not produce any point with predicted and observed values that differ by a factor of less than 0.5 or greater than two.

Table 3.6: Comparison of proposed NDHG equations with previously best-performing empirical equations.

Morphology	Name	RMSE	RMSElog	PE	S_x	MAE	EF
Cascade	NDHGCA	0.055	0.052	0	11.865	0.037	0.863
Step-pool	NDHGSP	0.070	0.076	0	18.208	0.052	0.817
Plane-bed	NDHGPB	0.098	0.076	0	19.101	0.076	0.848

3.3.3. Variance decomposition methodology (VDM)

The calibration required for the Box–Cox transformation provides the following data: Cascade, $\lambda = 0$; Step-pool, $\lambda = 1$; Plane-bed, $\lambda = 0$. When $\lambda = 0$, the Box–Cox transformation is a logarithmic transformation $BC(Y) = \log(Y)$. The use of calibrated parameters allows the decomposition of the variance, as shown in Table 3.7. Table 3.7 reveals that most of the error variance is contained in the model output. There are slight differences in the variance of observation errors, but analysis can be conducted based on the ratio of the relative to total residual error variance. Hence, the Cascade morphology exhibited the largest observation error variance, followed by Plane-bed and Step-pool. The calibration data was used to calculate the band presented in Figure 3.4; for all three morphologies, approximately 70% of the data is inside the band.

Table 3.7: Variance decomposition methodology for the studied morphologies.

Term	Cascade		Step-Pool		Plane-Bed	
	Value	%	Value	%	Value	%
Se2Yo	8.986E-05	3.336	6.786E-05	1.367	1.532E-04	2.532
Se2Y	0.00260	96.664	0.00490	98.633	0.00590	97.468
Se2Y-Yo	0.00269	100.00	0.00496	100.00	0.00605	100.00

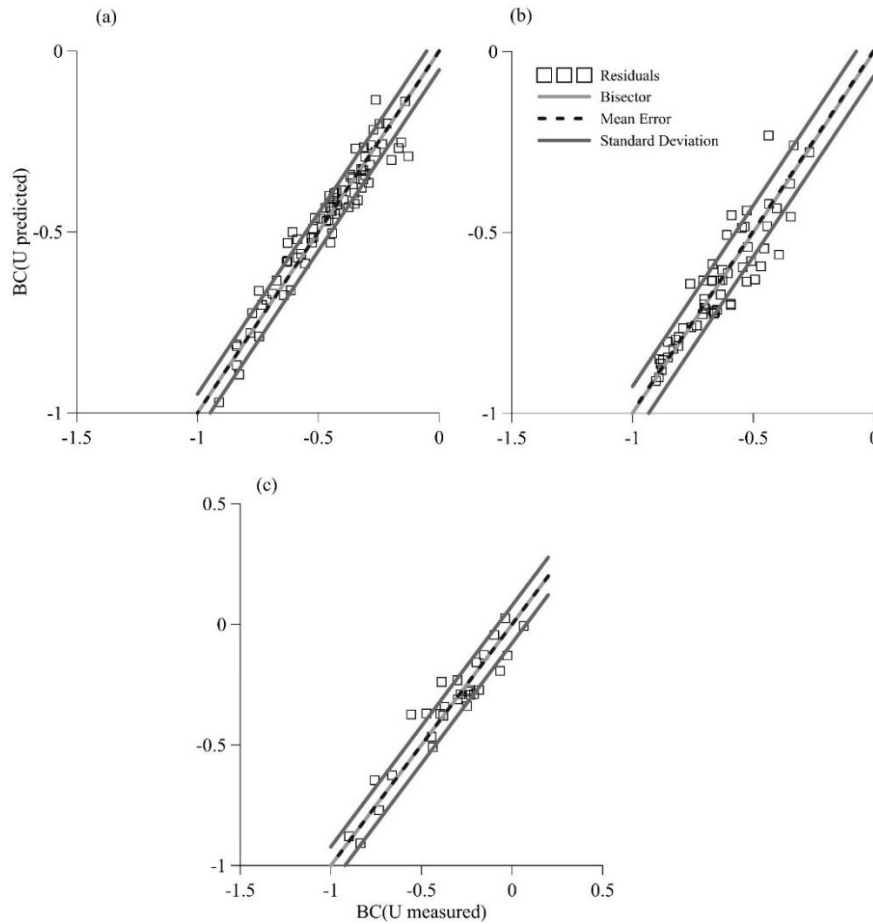


Figure 3.4: Plot of observed and predicted velocity values: (a) Cascade; (b) Step-pool; (c) Plane-bed.

3.3.4. Test with data from literature

Figure 3.2 depicts the linear regression of U^{**} and q^{**} of randomly chosen 50% of literature data. The regression provides the information needed to estimate a_1 , a_2 , and a_3 . The obtained equation was called NHDGlit. Table 3.8 compares the performance of NHDGlit and Zi12010. In this Table, three metrics have been used: RMSEa and MAEa are dimensionless versions of RMSE and MAE, defined as a percentage of the observations mean, and EF is the Nash–Sutcliffe efficiency index. RMSEa and MAEa depict a marked predictive superiority of NHDGlit against Zi12010. According to EF, NHDGlit has a very good performance rating, however, Zi12010 EF shows an unsatisfactory performance rating (Ritter & Muñoz-Carpena, 2013).

Table 3.8: Comparison of the proposed NDHG equation (NHDGlit) with the previously best-performing empirical equation.

Method	RMSEa (%)	MAEa (%)	EF
Zi12010	53	43	0.296
NHDGlit	19	13	0.910

3.4 Discussion

3.4.1 Characteristics of NDHG equations

Bathurst (2002) suggested that a resistance equation needs two parameters, one representing at-a-site resistance variation, and the other representing between-site resistance differences. At-a-site variations are usually related to the relative submergence d/D_{84} (Maxwell & Papanicolaou, 2001). According to Bathurst (1985), D_{84} provides a 3-D image of the bed material disposition. However, Aberle & Smart (2003) state that D_{84} is not a good resistance height for Step-pools. Indeed, q^* is considered a better at-a-site parameter, as any measurement error affects the observed and predicted values (Ferguson, 2007). In this study, the same function is attributed to q^{**} , as the equation structure is the same. The difference between q^* and q^{**} is that q^{**} comprises S_F in its denominator. The between-sites parameter, S_F (Zimmermann, 2010), represents the change in morphology

(Bathurst, 2002). Moreover, it is expected that the exponents in non-dimensional hydraulic equations change with morphology (Comiti et al., 2007).

In NDHG equations, the dimensionless unitary flow is less sensitive to measurement errors (Ferguson, 2007), and its combination with S_0 explains most of the resistance variation (Comiti et al., 2007; David et al., 2010). These equations do not assume any distribution of velocity or resistance parameter (Zimmermann, 2010). The velocity distribution in mountain rivers has an S-shape (Bathurst, 1985); in low-land rivers, the velocity distribution is semi-logarithmic. When Eq. (3.1) is used to calculate velocity, there is an assumption of uniform flow; this is not the case for mountain rivers, which are characterized by changes in water depth and surface slope at each XS (Bathurst, 1985). However, there is no better alternative for relating a resistance parameter with velocity. Dimensionless equations are preferred for the following reasons: (1) the exponents are also dimensionless; (2) in these equations, the common physics for all of the reaches are taken from empirical data (Parker et al., 2003, 2007).

3.4.2 NDHG parameters

Previous studies proposed constant exponents for NDHG equations (Comiti et al., 2009; Ferguson, 2007; Zimmermann, 2010). However, Nitsche et al. (2012) identified variability in a_1 . Nitsche et al. (2012) used data from six reaches with different morphologies and eight other Swiss mountain streams. In addition, a_1 depends on the concentration of boulders Γ ; the term containing slope was not included in their equation and a_2 was fixed as 0.6. Nevertheless, we found a_1 , a_2 , and a_3 to have different values for each studied site. According to the proposed methodology, these coefficients depend on the regression parameters of $\log(q^{**})-\log(U^{**})$ and the energy slope. Hence, this methodology requires collecting field data at different flow magnitudes, which is not possible in all cases. The authors consider that regression parameters \mathbf{m} and \mathbf{a} may be related to bed material or profile characteristics. Lacking sufficient data, we could not conduct this analysis. However, it would be possible to find an expression for \mathbf{m} and \mathbf{a} with additional data.

NDHG parameters depict certain patterns as a function of the reach morphology. The order of magnitude of a_2 (~ 0.5) and a_3 (~ 0.2) for Cascades and Step-pools are the same as in the literature; this is not the case for the Plane-bed. The relation between a_2 and a_3 is key to the importance of at-a-site variations compared to between-site variations in resistance. In Cascades and Step-pools, the at-a-site variation parameter has an exponent (a_2) that is 2.4 times larger on average than the between-site variation parameter (a_3). In a Plane-bed, this difference increases to 6.02 (a_2/a_3), illustrating that the effect of between-site variations in resistance is not relevant in a Plane-bed, which is logical, as there are no periodic bedforms in a Plane-bed. Ferguson (2007) found an a_2/a_3 ratio of 3:1 in pool-riffles, riffles, runs, and Step-pool reaches. This ratio is close to the value obtained for Cascade 2 in Table 3.5. Zimmermann (2010) conducted flume experiments in self-formed Cascade streams with a resulting a_2/a_3 ratio of 1.71, like the result for Cascade 1 in Table 3.5. Thus, the relations estimated with the proposed methodology are like those found in the literature for field and flume experiments.

The values for a_1 obtained with the proposed method are clearly higher than those presented in the literature. The a_1 value in our research varies from 1.83–2.87. Ferguson (2007) provided a value in the range of 1–1.74. Zimmermann (2010) obtained a value of 1.45. The difference in the values may be due to the data used to derive the equation. In this study, when a_1 , a_2 , and a_3 were obtained, each site was analyzed independently. However, in the other studies, data from different reaches were used to calibrate the equations. The separation of the reaches is due to the different at-a-site and between-site variations of resistance, which led us to believe that the parameters are dependent on the regression parameters and relate to the reach characteristics.

The values of \mathbf{m} and \mathbf{a} follow an evident pattern. Plane-bed values are higher than Cascade and Step-pool values. According to the results, this may be explained by smaller \mathbf{m} and \mathbf{a} values at higher resistance complexity.

3.4.3 Variance decomposition methodology (VDM)

Table 3.7 represents the variance decomposition of the NDHG equations for the analyzed morphologies. The trend shows that the variance of the observation error is higher in Cascades and Plane-beds than in Step-pools. Cascade and Plane-bed conductivity sensors cannot be installed in places without turbulence; these morphologies have bed material of significant size, which contributes to turbulence. In contrast, Step-pool data is collected from pools with a nearly stationary flow and smaller bed material. Moreover, Cascades and Plane-beds have the same calibration parameter for Box–Cox transformation ($\lambda = 0$); Step-pools have a calibration parameter of $\lambda = 1$.

Table 3.7 clearly indicates that model error variance (Se^2_Y) is the main component in the variance decomposition methodology. This term comprises different model output variances resulting from the model structure, the input, and the parameters. The model structure component is expected to be small because the NDHG equations represent the best equations for all examined morphologies. There was not a better equation structure for the performance of these equations. The inputs for this model are flow, gravity, wetted width, energy slope, and D_{84} . The energy slope is approximated with the water level; the water level had an error of 1.5% of the standard deviation uncertainty. Wetted width had less than 0.14% of the standard deviation uncertainty. These values were computed through repeated measurements from different morphologies. Flow has an error of 5% according to Lee & Ferguson (2002), who used tracers for flow and velocity measurement. The bed material 84th quartile (D_{84}) was obtained after sampling 400 particles at each reach to obtain the bed material distribution. Some studies sampled only 100 particles in studying pool-riffles and boulder-cobble beds (Bathurst, 1985, 2002; Marcus et al., 1992). The number of samples increased to 300 particles when additional morphologies were examined (David et al., 2010). It is evident that increasing the number of samples decreases the estimation error in the bed material distribution, given that the input parameters have a small influence on the model error variance. Hence, most of the model error variance corresponds to the parameters a_1 , a_2 , and a_3 . Table 3.4 presents the performance of different versions of NDHG equations with diverse parameter values. Figure 3.4 shows the band encompassing the mean error \pm standard deviation, which for a normal distribution includes 68.26% of the data. Given that 70% of the points fall inside the band for all morphologies, the normal distribution assumption is justified and the confidence interval of the model equals 70%.

The use of standard deviation of bed elevations (s) has been tested as characteristic resistance length in multiple studies, however, s provides good results only in some of them. Aberle & Smart (2003) have successfully used s (s from 4.6 to 14.6 mm) as a resistance parameter in a power equation in Step-pools to predict $(8/f)^{0.5}$ based on flume data. Lee & Ferguson (2002) (s ranged from 0.068–0.257) use field and flume data from Step-pools to find an equation to predict $(1/f)^{0.5}$. A log law equation provided good results when the effective resistance was step D_{84} . Nitsche et al. (2012) (s lies in the range of 0.07 to 0.47) found an NDHG equation whose dimensional macro resistance parameters to calculate velocity and dimensionless unitary flow was D_{84} . In this study (s range 0.022 to 0.214) different equations were tested, some of them with different representations of effective resistance, but NDHG equations provided the best fitting, and a new methodology to determine its parameters has improved fitting performance. All the NDHG equations used in this research utilize D_{84} to estimate velocity and dimensionless unitary flow, so this term seems to work well for these types of equations.

3.5 Conclusions

In this research, the flow resistance in three morphologies of a headwater mountain river was studied, in three Cascades, two Step-pools, and one Plane-bed. Each reach was divided into three to five XS where staff gauges were installed. Field measurements of water level and wetted width were collected at each XS. For each reach, flow and mean velocity were computed for different water level conditions. Different empirical equations for velocity prediction were tested using goodness-of-fit metrics. The equation with the best performance was calibrated to find expressions for its exponents. Moreover, variance de-composition methodology was used to estimate the uncertainty of the proposed method. As a final step, data from the literature was used to test the proposed methodology.

The findings clearly indicate that the best equations for the studied morphologies are NDHG equations; no other type of equation exhibited similar performance. A methodology to find the NDHG exponents was proposed using logarithmic regression, the bed shear stress, and the generalized power law. The resulting equations for the exponents in the NDHG equations have variations according to the type of reach and depend on regression parameters, namely the slope and the independent terms (m , a). The derived Step-pool and Cascade ratios (a_2/a_3) are in accordance with data from the literature; for the Plane-bed, this ratio is larger due to the small influence of the between-site resistance variation component in this morphology. Besides, the proposed methodology was successfully used to predict data from the literature. The applicability of the proposed approach for estimating the exponents of NDHG equations can certainly be improved with additional data (experimental measures and other morphologies). As the m and a parameters may follow a certain pattern, this methodology is useful for ungauged streams.

Chapter 4

4 Assessment of calibrated and measured based resistance parameter

Redrafted from:

Cedillo, Sebastián, Esteban Sánchez-Cordero, Luis Timbe, Esteban Samaniego, and Andrés Alvarado. 2021. "Patterns of Difference between Physical and 1-D Calibrated Effective Resistance Parameters in Mountain Rivers." *Water* 13 (22): 3202. <https://doi.org/10.3390/W13223202>.

Abstract: Due to the presence of boulders and different morphologies, mountain rivers contain various resistance sources. To correctly simulate river flow using 1-D hydrodynamic models, an accurate estimation of the flow resistance is required. In this article, a comparison between the physical resistance parameter (PRP) and effective resistance coefficient (ERC) is presented for three of the most typical morphological configurations in mountain rivers: cascade, step-pool, and plane-bed. The PRP and its variation were obtained through multiple measurements of field variables and an uncertainty analysis, while the ERC range was derived with a GLUE procedure implemented in HEC-RAS, a 1-D hydrodynamic model. In the GLUE experiments, two modes of the Representative Friction Slope Method (RFSM) between two cross-sections were tested, including the variation in the resistance parameter. The results revealed that the RFSM effect was limited to low flows in cascade and step-pool. Moreover, when HEC-RAS selected the RFSM, only acceptable results were presented for plane-bed. The difference between ERC and PRP depended on the flow magnitude and the morphology, and as shown in this study, when the flow increased, the ERC and PRP ranges approached each other and even over-lapped in cascade and step-pool. This research aimed to improve the resistance value selection process in a 1-D model given the importance of this parameter in the predictability of the results. In addition, a comparison was presented between the results obtained with the numerical model and the values calculated with the field measurements

Keywords: effective resistance coefficient; physical resistance parameter; HEC-RAS; mountain-rivers; representative friction slope method; bed resistance

4.1 Introduction

Flow resistance in a river is given by the energy losses due to the interaction of water with its flowing contour. In 1-D and 2-D models, based on Saint-Venant/shallow water equations, the energy losses are expressed by an "effective resistance coefficient," a parameter that encompasses the different levels of energy dissipation (Morvan et al., 2008). Thus, the parameter in question becomes an adjustment parameter for the correct prediction of results. The 1-D hydrodynamic model remains a suitable option for the numerical simulation of rivers, an approach that requires less computation and field data and that has been used widely for many years in river engineering (Cook & Merwade, 2009). The inherent uncertainties present in the application of a 1-D hydrodynamic model lead to discrepancies between the "effective resistance coefficient" (ERC) and the "physical resistance parameter" (PRP) calculated using field measurement data.

The sources of uncertainty in hydrodynamic models can be categorized into two main groups: natural and epistemic (Teng et al., 2017). Natural uncertainties deal with the natural variation in a phenomenon (Papaioannou et al., 2017), while epistemic uncertainties are related to the lack of knowledge of a system. These uncertainties include: (a) model structure, due to simplifications performed in the model to bring a natural phenomenon into a mathematical representation (Blasone et al., 2008; Pappenberger et al., 2005) (b) solution procedure, how the equations are solved (energy equation, momentum and mass balance equation); (c) topography, for the geometric description of the study area (Cook & Merwade, 2009); (d) input and output data (Teng et al., 2017); and (e) model parameters such as the Manning resistance coefficient. One of the methods to study model uncertainty, with increasing popularity, is the Generalized Likelihood Uncertainty Estimation (GLUE), which considers the existence of a set of parameters and model structures with a similar performance reproducing validation data (Aronica et al., 2002; Beven & Binley, 2014; Blasone et al., 2008; Bozzi et al., 2015).

GLUE is a Bayesian Monte Carlo method that recognizes the presence of errors in calibration data, model structure, and boundary conditions, rejecting the concept of a unique global optimum parameter set, instead accepting the existence of different parameter sets that are similar in producing good fit model predictions

(Beven & Binley, 1992; Blasone et al., 2008). In the literature, there are some studies where a certain GLUE framework has been used to study the effective resistance parameter. Pappenberger et al. (2005) performed a GLUE analysis in a 1-D unsteady flow experiment for two rivers with different boundary conditions and evaluation data. In that experiment, the resistance parameter and the weighting coefficient of the numerical scheme were varied in the GLUE framework. The type of boundary condition, evaluation data, geometry, and magnitude of the analyzed event influenced the combined likelihood curve behavior. The variation in the weighting coefficient did not alter the output of the model but influenced the number of valid runs. Bholia et al. (2019) performed a study in a 2-D unsteady HEC-RAS model with water height as calibration data. The reach was divided into five land uses, each with a certain range of resistance values. The uncertainty output bound was reduced from 1.26 m to 0.34 m (90% confidence interval) by constraining the objective function value for acceptable runs. Furthermore, there have been other investigations in which the GLUE framework was used to test different likelihood functions (Aronica et al., 1998; Jung & Merwade, 2012) or different types of calibration data (Aronica et al., 2002; Horritt & Bates, 2002). In those studies, a measured physical resistance value was not mentioned or compared with the obtained effective resistance value, but the distinction between both was emphasized (Pappenberger et al., 2005).

In this study, a calibration process of the effective resistance coefficient (ERC) obtained from the 1-D component of HEC-RAS using the GLUE methodology was performed and compared with the physical resistance parameter (PRP) derived from field data. Within the GLUE framework, the 1-D model was configured with two different approaches based on the representative friction slope method (RFSM) between two cross-sections: in Experiment 1, the RFSM was manually selected, and in Experiment 2, the RFSM was automatically chosen. In this research, all the data were collected during inbank flow conditions, implying that the ERC values correspond to the main channel resistance. The ERC values were assessed against field measurements in three different morphologies (step-pool, cascade, and plane-bed) and three different flow magnitudes (high, medium, and low). The results revealed that the RFSM influence on model performance was limited to the morphology and the magnitude of the flow, and that the effective and real physical parameters differed.

4.2 Materials and methods

4.2.1. Study area

The Quinuas reach, tributary of the Paute river basin, located between the eastern and western cordillera of the Andes in Ecuador, was selected for this study. The reach under-study has a length of 1.5 km and contains different morphologies such as plane-beds, cascades, and step-pools. The terrain level upstream of the reach (0 + 000) is 3664.4 m.a.s.l. and that downstream of the study reach is (1 + 431.13) 3605.77 m.a.s.l., resulting in an average bed slope of 4%. The following morphologies were selected in the 1.5 km river reach: Step-pool 1, Plane-bed 1, and Cascade 3 (see Figure 4.1 for their location), named herein in this article Step-pool, Plane-bed, and Cascade, respectively.

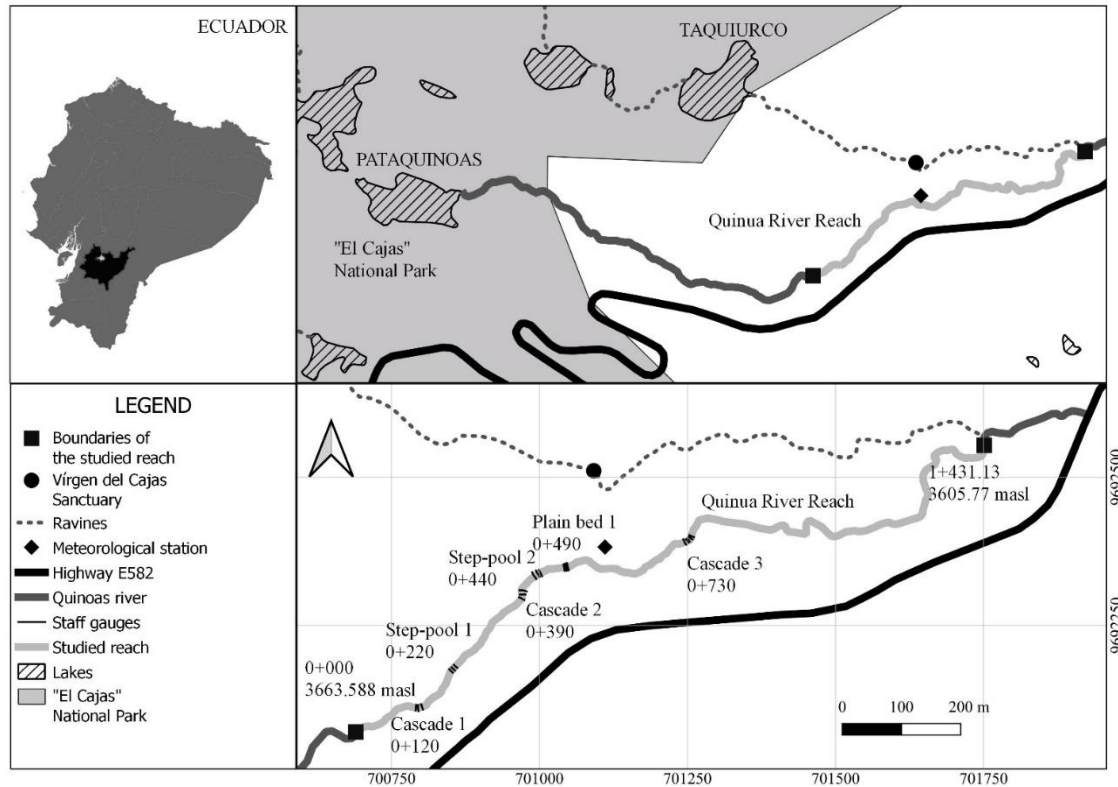


Figure 4.1: Location of the 1.5 km river reach with indication of the different morphologies.

4.2.2. Field data

Topographic information was gathered using a differential GPS (Trimble® R6) and total station survey (Sokkia® 550 RX) depending on the visibility. The objective was the capture of critical details with adequate measurement precision (see Figure 4.2). The measured cross-sections (XSs) were taken at certain relevant locations such as changes in bed slope or changes across XSs.

Three staff gauges were used for measuring the water levels in the Step-pool 1 and Plane-bed 1 reaches (Figures 4.2 a, c, respectively) and five staff gauges in the Cascade 3 reach (Figure 4.2b). In addition, at every staff gauge, the wetted width (w) was measured with a measuring tape, while the discharge (Q) was estimated using the dilution-gauging method with salt as a tracer (Hudson & Fraser, 2005a). Two HOBO U24-00 freshwater conductivity data loggers were placed upstream and downstream of the reach. These devices have an accuracy of 3%, a resolution of $1 \mu\text{S}/\text{cm}$, and a temperature range of -2 to $36 \text{ }^\circ\text{C}$. Figure 4.3 depicts the studied reaches and the used staff gauges.

The flow velocity (U) was determined using two conductance curves, located upstream and downstream in each reach, using the Harmonic methodology (Nitsche et al., 2012) for defining the travel time. The velocity was calculated as the ratio between the distance between staff gauges and the mean travel time. The Friction Slope (S_F) was approximated with the water surface slope (S_W) (David et al., 2010), and the bed material distribution size was estimated using the pebble counting approach (Bunte & Abt, 2001) with a sample of 400 particles. The resistance coefficient was initially determined with the Darcy–Weisbach equation (Eq. (4.1)) with average geometric values for the cross-section of the selected reach. Thereafter, the f coefficient was transformed into Manning's resistance parameter n using Eq. (4.2).

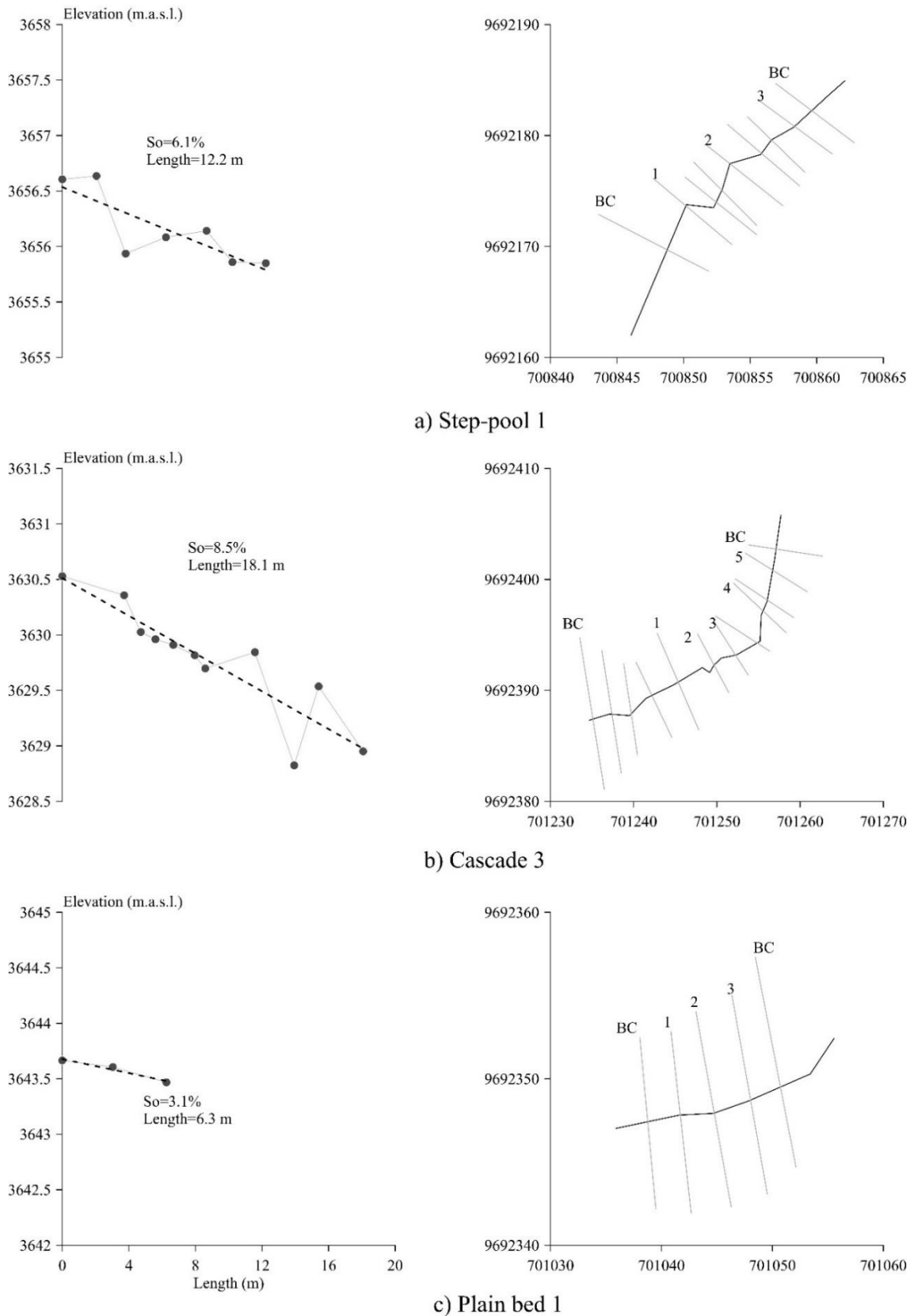


Figure 4.2: Profiles and topographic characteristics of morphologies under study. (a) Step-pool 1 (b) Cascade 3 (c) Plain bed 1.



a) Step-pool 1



b) Cascade 3



c) Plain bed 1

Figure 4.3 : Pictures of analyzed reaches. (a) Step-pool 1 (b) Cascade 3 (c) Plain bed 1.

$$f = (8 g R S_f) / U^2 \quad (4.1)$$

$$PRP = n = [(f R^{1/3}) / (8 g)]^{0.5} \quad (4.2)$$

4.2.3 Numerical scheme

The hydrodynamic model chosen in this research was the 1-D component of HEC-RAS, developed by the Hydrologic Engineering Center (HEC) of the United States Army Corps of Engineers. In this study, all simulations were performed assuming steady-state conditions. The energy equation (Eq. (4.3)) is solved between two adjacent XSs, while, in the case of not obtaining an equilibrium, the numerical algorithm uses the critical depth response given the specific condition. In cases of rapidly varying flow, HEC-RAS solves the momentum equation.

$$z_2 + y_2 + \alpha_2 U_2^2 / (2 g) = z_1 + y_1 + \alpha_1 U_1^2 / (2 g) + h_e \quad (4.3)$$

where z is the elevation of the main channel (m), y is the water depth (m), U is the velocity ($m s^{-1}$), g is the gravity acceleration ($m s^{-2}$), and h_e is the energy head loss (m) (Eq. (4.33)). The subscript in XS, 2 and 1, refers to upstream and downstream, respectively.

The energy head loss (Eq. (4.4)) comprises the loss due to resistance and contraction/expansion losses. Different methodologies are available to estimate the representative friction slope between two cross-sections (RFSM): the average conveyance equation (Eq.(4.5) ACE, the default methodology in HEC-RAS), the average friction

slope equation (Eq. (4.6) AFSE), the geometric mean friction slope equation (Eq. (4.7) GMFSE), and the harmonic friction slope equation (Eq. (4.8) HMFSE).

$$h_e = L \text{ RFSM} + C_C |\alpha_2 U_2^2 / (2 g) - \alpha_1 U_1^2 / (2 g)| \quad (4.4)$$

where L is the reach length (m), RFSM is the friction slope between two XSs, and C_C is a contraction expansion coefficient. RFSM is calculated using Eq. (4.5).

$$\text{RFSM} = [(Q_1 + Q_2) / (K_1 + K_2)]^2 \quad (4.5)$$

where Q is the flow rate ($\text{m}^3 \text{ s}^{-1}$) and K is the conveyance ($\text{m}^3 \text{ s}^{-1}$). RFSM can also be calculated using Eqs. (4.6), (4.7), or (4.8), respectively:

$$\text{RFSM} = (S_{F1} + S_{F2}) / 2 \quad (4.6)$$

where S_{F1} is the friction slope at the upstream XS and S_{F2} is the friction slope at the down-stream XS.

$$\text{RFSM} = (S_{F1} S_{F2})^{0.5} \quad (4.7)$$

$$\text{RFSM} = (2 S_{F1} S_{F2}) / (S_{F1} + S_{F2}) \quad (4.8)$$

As the velocity distribution of the water flow in a channel presents three-dimensional characteristics, it is necessary to correct it with the coefficients α and β to maintain the energy and momentum flux when the mean cross-section velocity is used (Knight et al., 2009). α is obtained with a flow-weighted average in the main channel and overbanks (Eq. (4.9)). Given that the experiments developed in the current research are inbank flow and the water surface is considered as horizontal (Pappenberger et al., 2005), α will be equal to one.

$$\alpha = [A_t^2 (K_{lob}^3 / A_{lob}^3 + K_{mc}^3 / A_{mc}^3 + K_{rob}^3 / A_{rob}^3)] / K_t^3 \quad (4.9)$$

where K_{lob} , K_{mc} , and K_{rob} are the conveyance at the left overbank, main channel, and right overbank ($\text{m}^3 \text{ s}^{-1}$), respectively; K_t is the total conveyance ($\text{m}^3 \text{ s}^{-1}$); A_{lob} , A_{mc} , and A_{rob} are the flow areas at the left overbank, main channel, and right overbank (m^2), respectively; and A_t is the total flow area (m^2).

For each study reach, the effect of the geometric description was analyzed. The topographic information (Figure 4.3) was used as a base to include additional XSs interpolated at equidistant distances (one meter, fifty centimeters, and twenty-five centimeters). At each run, the errors and warnings were checked and documented. The final geometric model for each reach was the one without any warning. This test used the physical resistance as the effective resistance for each case. The validation data to verify the performance of each model were the water levels in the staff gauges. These water levels were transformed into water levels relative to the deepest cross-section point. The water depth resulting from the model was transformed in the same way to be compared with the measurements. Ultimately, the HEC-RAS model was run under a steady-state condition with a mixed flow regime (i.e., subcritical and supercritical flow). The boundary conditions in the cross-sections labeled as BC in Figure 4.2 were normal depth. The validation data consisted of water levels taken from staff gauges labeled with a number in Figure 4.2.

4.2.4 The GLUE methodology

Two GLUE experiments with variable resistance values were performed for three different flows at each reach. Experiment 1 consisted of 5000 runs for each RFSM: ACE (Eq. (4.5)), AFSE (Eq. (4.6)), GMFSE (Eq. (4.7)), and HMFSE (Eq. (4.8)), while in Experiment 2, HEC-RAS internally selected the RFSM (8000 runs) based on profile type and flow regime. The GLUE process was implemented using the HEC-RAS Controller in Visual Basic Excel® (Microsoft Corporation manufacturer, Redmond, Washington, United States city, country) (Goodell, 2014). The range of resistance coefficients (Manning values) was selected to cover all the possible variations (Aronica et al., 1998) and considering a uniform distribution (Pappenberger et al., 2005). The range 0.03–0.5 was imposed using as a criterion for the minimum value recommended in Brunner (2021) for mountain streams and for the maximum value measured in the field campaigns. However, the step-pool resistance range needed to be extended up to 0.7 for low flows as the previous resistance range was not wide enough to capture a peak in the likelihood curve. In Experiment 1, each RFSM was identified with a number (1: Eq. (4.5), 2: Eq. (4.6), 3: Eq. (4.7), 4: Eq. (4.8)) and was selected considering a uniform distribution.

There is no universal likelihood function for GLUE experiments (Blasone et al., 2008); indeed, Jung & Merwade (2012) found that different likelihood functions produced different uncertainty bounds (5–95%) that did not produce important changes in the overall uncertainty quantification of an inundation map. In this research, the likelihood function included the sum of root-mean-square error (RMSE), mean average error (MAE), and the standard deviation of residuals (SDR). These metrics were normalized by applying Eq. (4.10). RMSE and MAE represent the residuals' mean having different weights in the average procedure, while SDR is a dispersion of the residuals measure. The likelihood value is one when the measurements exactly coincide with the modeling result.

$$\text{Likelihood} = 1 - \text{RMSE}/O_m - \text{MAE}/O_m - \text{MSDR}/O_m \quad (4.10)$$

where O_m is the observations' mean.

The range of PRP consisted on resistance parameters with a likelihood value having a difference less than 0.01 with the peak likelihood value.

4.2.5 Uncertainty measurement analysis PRP

The uncertainty of direct measurements such as wet width (w) and water level (η) were determined by repeating measurements. Resolution and random errors were combined in the measurements (Eq. (4.11)).

$$\text{Relative Uncertainty (\%)} = \delta X / X_o \quad (4.11)$$

where δX is the absolute uncertainty of X and X_o is the central value of the variable.

The uncertainty of indirect measurements (W in Eq. (4.12)), which was estimated based on direct measurements of X , Y , and Z , is given by Eq. (4.12) (Fornasini, 2008). The result of Eq. (4.12) was used to obtain the range of variations in W with Eq. (4.13).

$$\delta W = \left| \frac{\partial Q}{\partial X} \right|_o \delta X + \left| \frac{\partial Q}{\partial Y} \right|_o \delta Y + \left| \frac{\partial Q}{\partial Z} \right|_o \delta Z \quad (4.12)$$

$$W = W_o \pm \delta W \quad (4.13)$$

where δW is the absolute uncertainty of W , W_o is the central value of the variable, and W is the range of possible values of this variable.

4.3 Results

4.3.1 Likelihood curves

The results of the first GLUE experiment in which the resistance coefficient in the three morphologies was varied according to each RFSM method are presented in Figure 4.4.

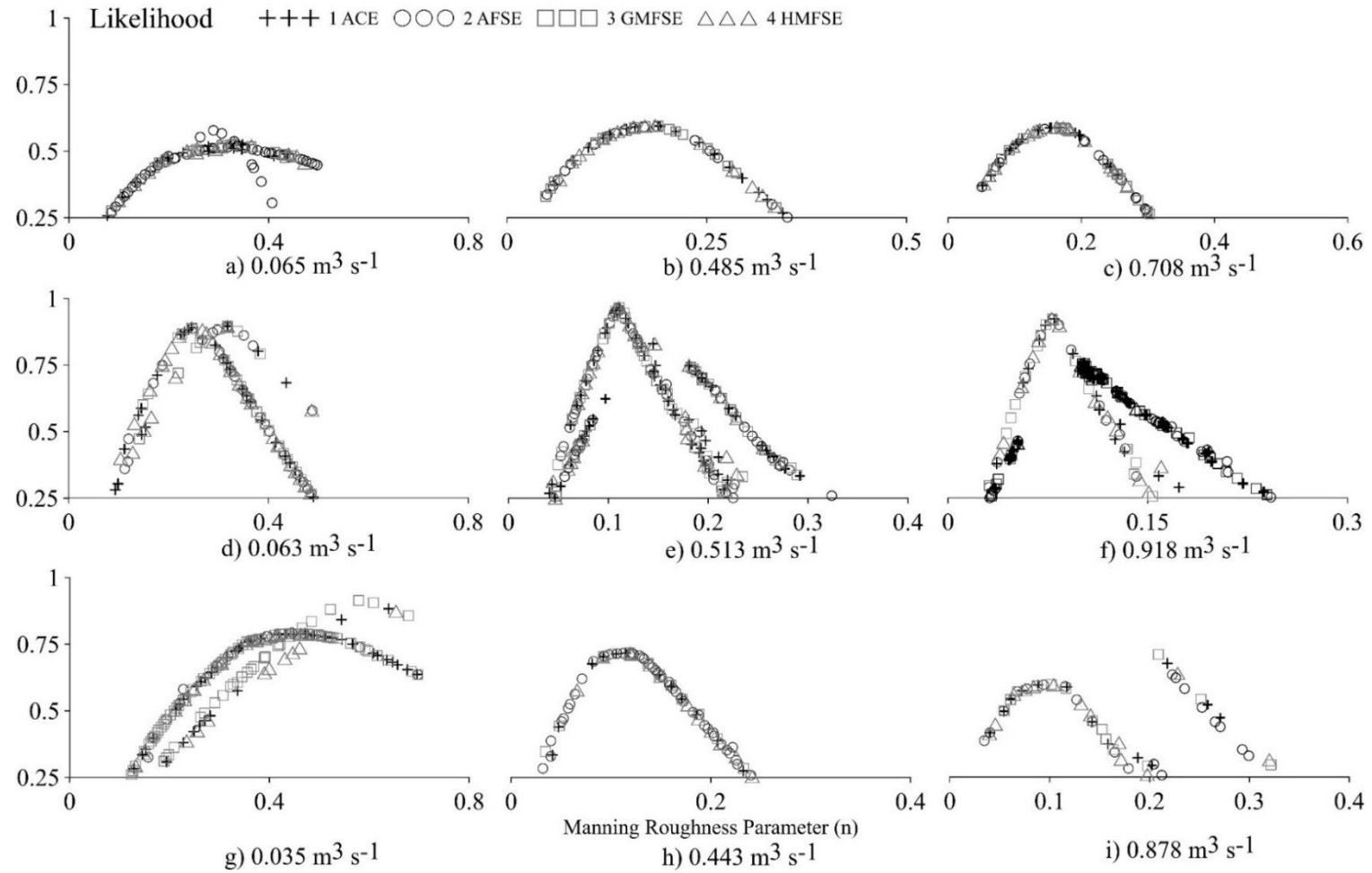


Figure 4.4: GLUE likelihood curves in Experiment 1: Cascade (a, b, c), Plane-bed (d, e, f), and Step-pool (g, h, i).

For practical purposes, only the points with a probability threshold greater than 0.25 are shown as lower values are considered as nonbehavioral by not providing relevant information.

Figure 4.4 reveals that the resulting likelihood curves are concave downward with one or two peaks depending on the flow magnitude and morphology. Cascade has two slightly different likelihood peaks for low flow, but for mid and high flows, there is only one performance peak. Plane-bed has two performance peaks for all flow magnitudes. Step-pool at low flow has two peaks, while at high flow, there is one peak in a concave downward curve in the left and one maximum in a linear pattern in the right. For mid flow, there is a single likelihood peak.

Figure 4.4a presents the formation of two likelihood curves; the higher performance curve has points from AFSE exclusively, while the lower performance curve is composed of points from all RFSMs. Figures 4.4d–f show the formation of two likelihood curves composed from all RFSM points. In the cases under study, the one in Figure 4.4g presents the formation of two likelihood curves, where it can be observed that the one with the best performance is composed only of the GMFSE points. Special attention should be given to the likelihood curves in Figure 4.4i, where the formation of a curve without concavity can be observed on the right side of the figure. Those results are further discussed in the Discussion section in the subsection Likelihood Curves. Cascade peaks have the lowest performance values (~0.6) in all cases under analysis (Figures 4.4a–c). Plane-bed has peak performance values greater than 0.89 (Figure 4.4d–f), while step-pool peak performance values decrease with flow magnitude, ranging from 0.91 to 0.61 (Figures 4.4 g–i).

The results of the second GLUE experiment (8000 runs) in which HEC-RAS selects RFSM are depicted in Figure 4.5. Step-pool and cascade show a linear horizontal likelihood trend (constant) with low-performance values. Plane-bed likelihood curves are presented in Figures 4.5d–f. The shapes of the curves present concavity downward with peak performance values greater than 0.89.

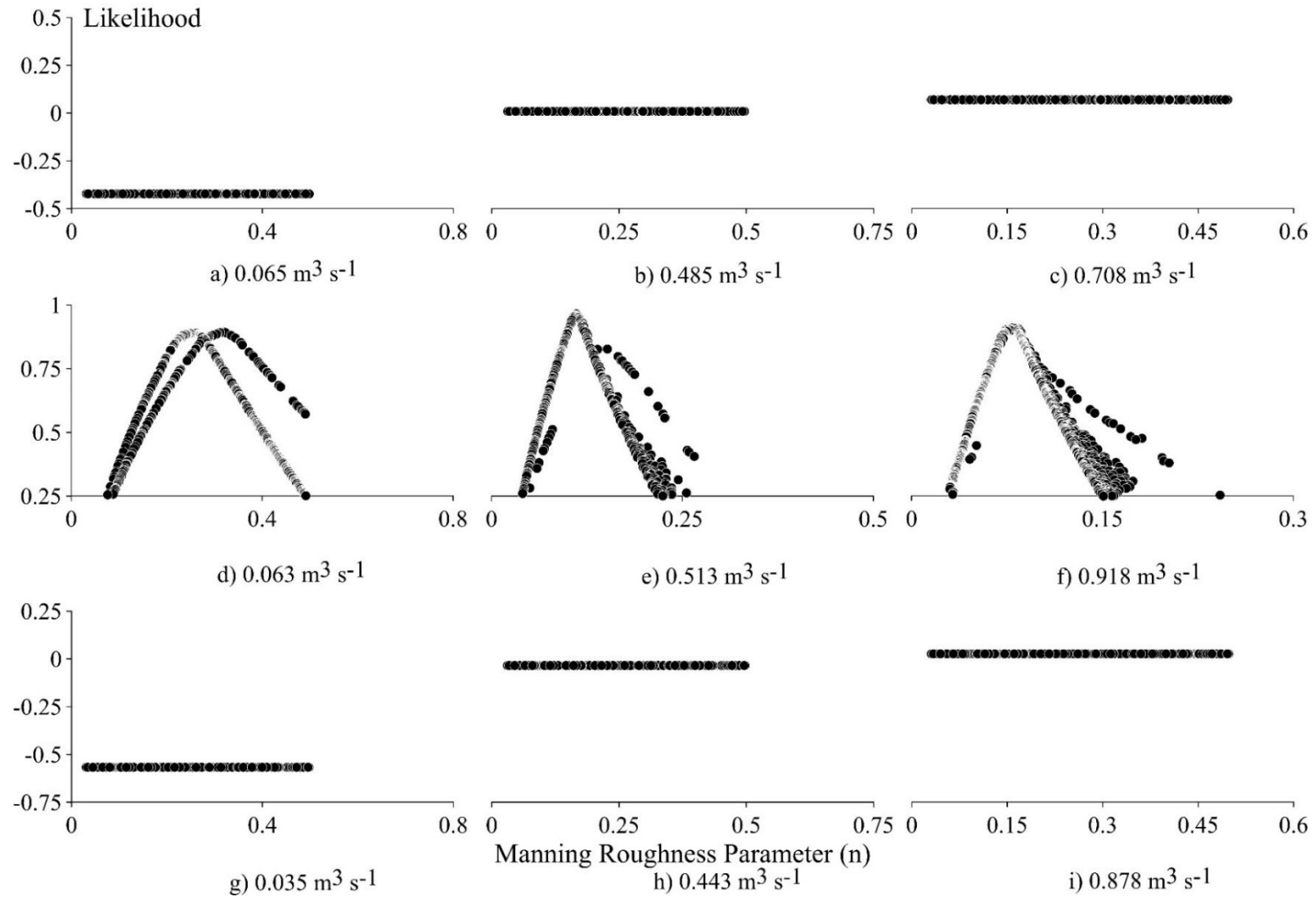


Figure 4.5: GLUE likelihood curves in Experiment 2: Cascade (a, b, c), Plane-bed (d, e, f), and Step-pool (g, h, i).

4.3.2 Field measurements uncertainty

Uncertainties in the direct measurement used to estimate the resistance parameter are the wetted width, water level, velocity, and flow. The wetted width uncertainty is less than 0.14% of the standard uncertainty, while water level (η) has a 1.5% of standard uncertainty; these values are comparable to those found by Lee & Ferguson (2002). The uncertainties for velocity and flow measurement were taken from Lee & Ferguson (2002) as 5% as tracers were used for the flow and the centroid method for the velocity calculation. The indirect measurement uncertainties are 10% for the water depth, comparable with the 12% obtained by Lee & Ferguson (2002), 10% for the hydraulic radius, 17% for the energy slope, and 19% for $(8/f)^{1/2}$. The former value is comparable with the value found by Lee & Ferguson (2002). Based on the above information, the Manning resistance parameter (n) uncertainty was estimated at 22% of the standard deviation.

4.3.3 Effective and measured resistance values

The value ranges of the effective resistance coefficient (ERC)—calibrated—and physical resistance parameter (PRP)—measured—for different flow rates in Experiment 1 (changing resistance and RFSM at the same time) are shown in Table 4.1 and Figure 4.6. The range of ERC values was obtained from the analysis of the maximum likelihood curves (Figure 4.4), while the range of PRP values was the result of the indirect n measurement and the uncertainty analysis. Table 4.1 compares the PRP, velocity, and Froude numbers measured in this study with those in the literature (Bathurst, 1985; Yochum et al., 2014).

The comparison in Table 4.1 shows that the values of the data calculated in the present study are among the measured ranges presented in the literature. An important aspect to emphasize is that the Froude number presents a value lower than that in all the sections studied despite the steep slopes. Jarrett (1984) stated that extreme turbulence, energy loss produced by the channel, cross-sectional variations, and interactions of the water with the boulders increase the resistance to flow. Jarrett (1984) noted localized areas of supercritical flow, for example, in areas where the flow passes over large clasts. In Figure 4.3, the same pattern can be noticed, in which, in certain areas, supercritical flow is presented.

The difference between the ranges of ERC and PRP decreases with the magnitude of flow (seen from a quantitative and qualitative point of view according to Table 4.1 and Figure 4.6, respectively). The range values in ERC and PRP overlap for medium and high flows in cascade, while in plane-bed, the range values do not. In step-pool, the range values in ERC and PRP intersect only at high flow rates. Table 4.2 illustrates the results of Experiment 2 where the RFSM values are selected by HEC-RAS. Cascade and step-pool GLUE experiments did not provide a valid response, as for all resistance values tested, there is equifinality with a low likelihood (below the threshold value).

The low flow ERC range for plane-bed, listed in Table 4.1, is higher than the interval stated on Table 4.2. The values of both experiments coincide in the lower limit while they differ in the upper limit, in which the value of experiment 1 is higher. The values for the remaining flow magnitudes are the same for both experiments. Given that the results of cascade and step-pool in Table 4.2 cannot be used, and the results of plane-bed differ between both experiments only at low flows without improving the peak likelihood, the comparison of ERC and PRP is based on the information in Table 4.1 in Section 4.4: Discussion.

Figures 4.7, 4.8, and 4.9 depict the field-measured water depths, as well as the water surface profile obtained with ERC and PRP (Refer to Table 4.1). Cascade water depth profiles show that the field data at 24.93 m can be predicted by neither of the parameters, resulting in a low likelihood value obtained for this morphology. Nevertheless, the use of ERC in the model results in a better prediction of points at 18.91 and 24.93 m at low flow. Moreover, for mid and high flow, the intersection of ERC and PRP values makes sense as there is no marked difference between both water surface profiles. Figure 4.8 shows a notable difference in the water surface profile between both resistance parameters in plane-bed.

ERC considerably increases the predictive capacity of the model, which means that it does not cross with PRP. Besides, all the field measurements are closely predicted when using ERC, resulting in the high likelihood values previously mentioned. Figure 4.9 illustrates that the use of ERC in step-pool improves the model predictability at low and mid flow, but at high flow, both parameters produce a similar water surface profile. This aspect justifies the intersection of ERC and PRP only at high flows. The descending likelihood value in step-pool is because of the descending prediction capacity to predict the field measurement at 4.2 m.

Table 4.1: Range of values for measured and calibrated n value for Experiment 1

Site	EFFECTIVE RESISTANCE COEFFICIENT (ERC)						PHYSICAL RESISTANCE PARAMETER (PRP)					
	Flow ($\text{m}^3 \text{s}^{-1}$)	GLUE range	Likelihood	Best RFSM	Value Measured	Measurement uncertainty range (PRP)	PRP range found in literature (Bathurst, 1985; Yochum et al., 2014)	Measured Velocity (m s^{-1})	Measured Depth (m)	Measured Froude Number	Range of Velocity in literature (m/s)(Bathurst, 1985; Yochum et al., 2014)	Range of Froude Number in literature (Bathurst, 1985; Yochum et al., 2014)
Cascade	0.065	0.286–0.295	0.58	Equation (5)	0.433	0.338–0.528	0.16–0.44	0.168	0.146	0.141	0.12–0.86	0.15–0.51
	0.485	0.173–0.192	0.6	All	0.223	0.174–0.272		0.496	0.282	0.298		
	0.708	0.143–0.180	0.59	All	0.199	0.155–0.243		0.606	0.337	0.333		
Plane-bed	0.063	0.241–0.333	0.89	All	0.161	0.126–0.196	0.027–0.189	0.184	0.109	0.179	0.177–3.72	0.15–1.17
	0.513	0.108–0.115	0.96	All	0.0594	0.046–0.073		0.699	0.212	0.485		
	0.918	0.076–0.081	0.92	All	0.043	0.034–0.053		0.916	0.277	0.556		
Step-pool	0.035	0.555–0.609	0.91	Equation (6)	0.414	0.323–0.505	0.12–0.96	0.125	0.117	0.117	0.12–1.61	0.13–0.92
	0.443	0.105–0.124	0.72	All	0.193	0.151–0.235		0.464	0.287	0.277		
	0.878	0.092–0.121	0.61	All	0.134	0.105–0.163		0.733	0.330	0.407		

Table 4.2: Range of values for calibrated n value for Experiment 2

Site	Flow ($\text{m}^3 \text{s}^{-1}$)	GLUE range (ERC)	Likelihood
Cascade	0.065	Equifinality for all the resistance range	-0.422
	0.485	Equifinality for all the resistance range	0.0095
	0.708	Equifinality for all the resistance range	0.0702
Plane-bed	0.063	0.241–0.267	0.89
	0.513	0.108–0.113	0.96
	0.918	0.076–0.081	0.92
Step-pool	0.035	Equifinality for all the resistance range	-0.567
	0.443	Equifinality for all the resistance range	-0.0345
	0.878	Equifinality for all the resistance range	0.026

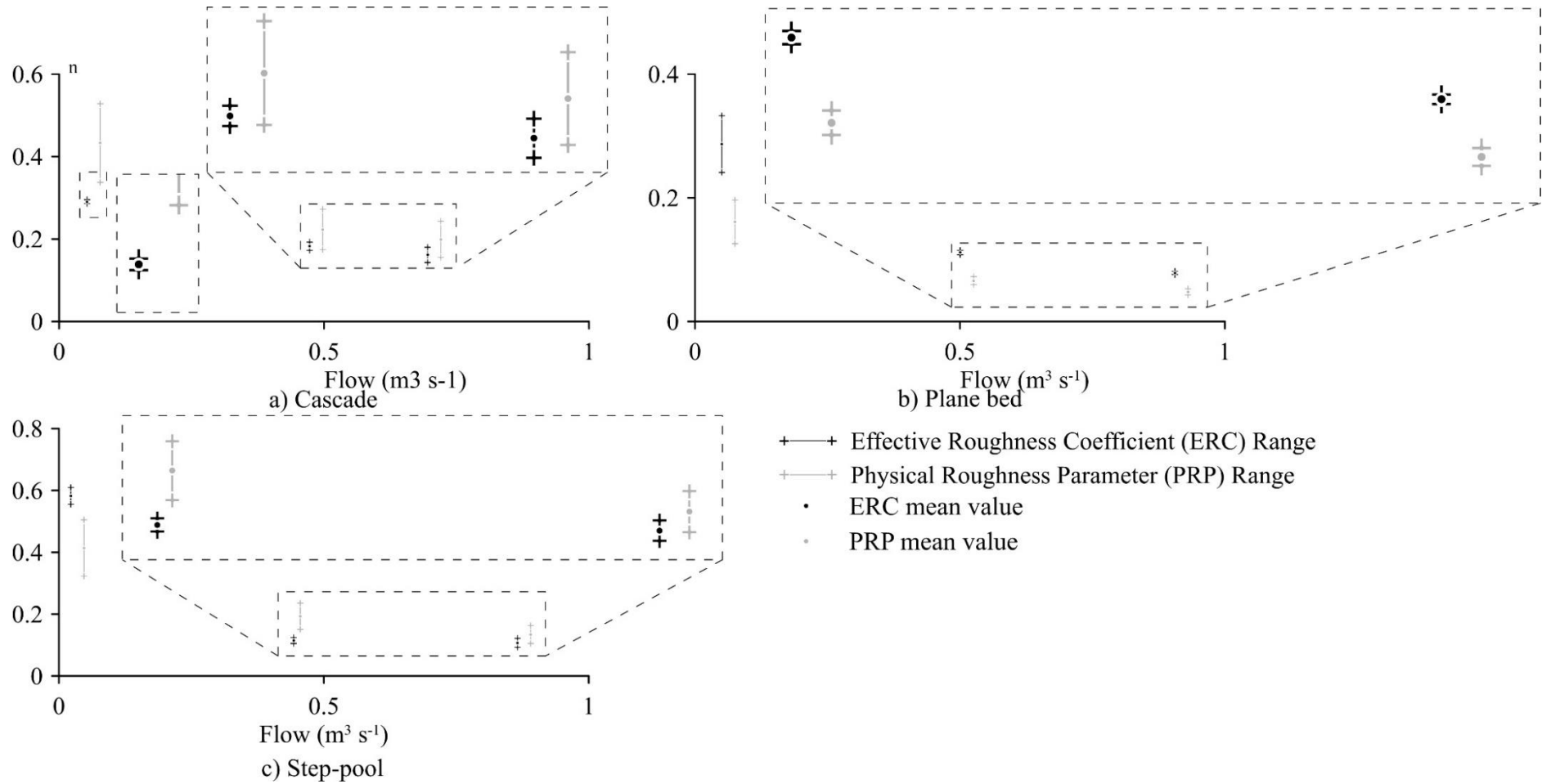


Figure 4.6: Comparison of measured and calibrated n values. (a) Cascade (b) Plane bed (c) Step-pool

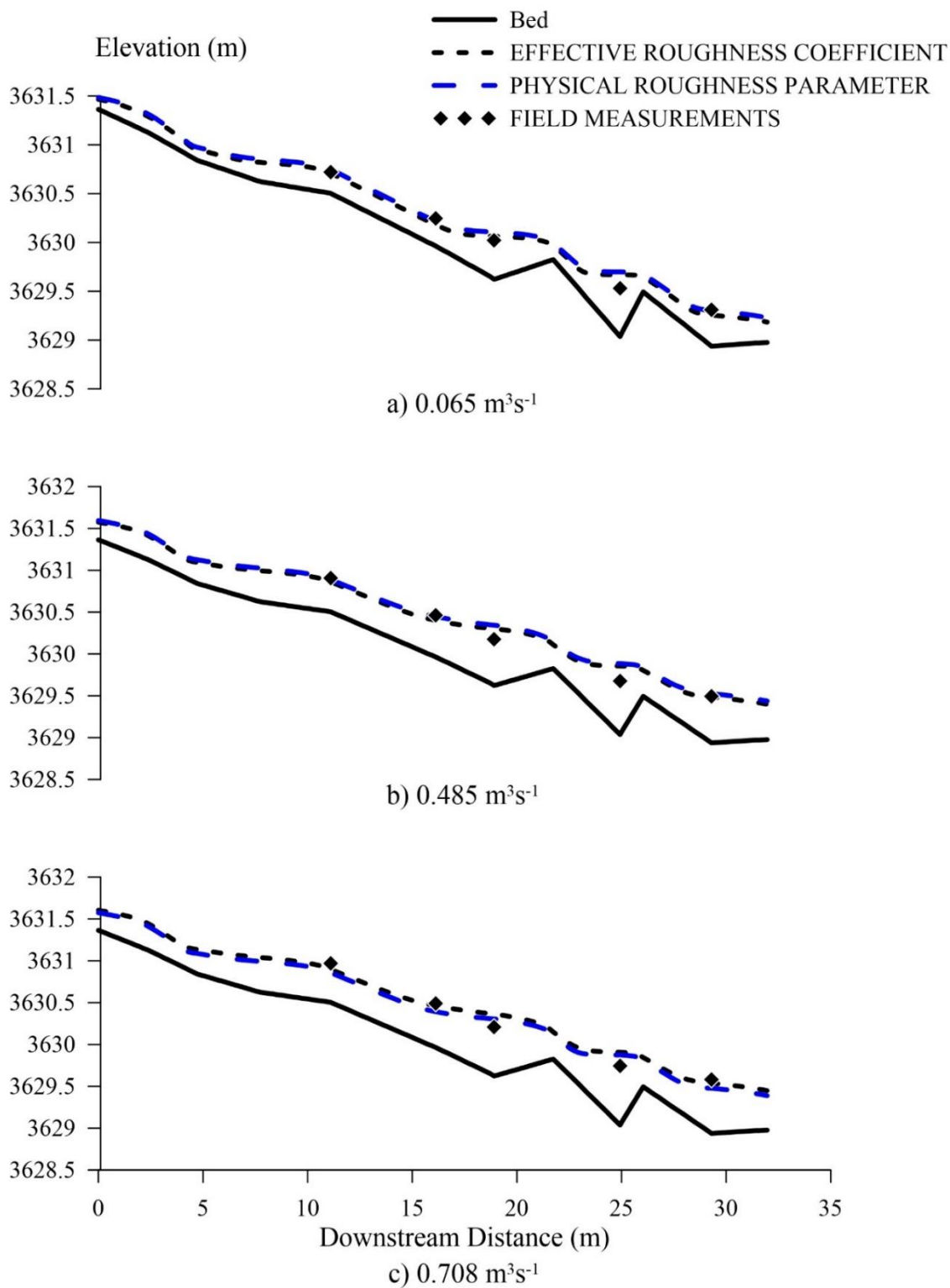


Figure 4.7: Water surface profiles using ERC and PRP in Cascade. a) $0.065 \text{ m}^3\text{s}^{-1}$ b) $0.485 \text{ m}^3\text{s}^{-1}$ c) $0.708 \text{ m}^3\text{s}^{-1}$

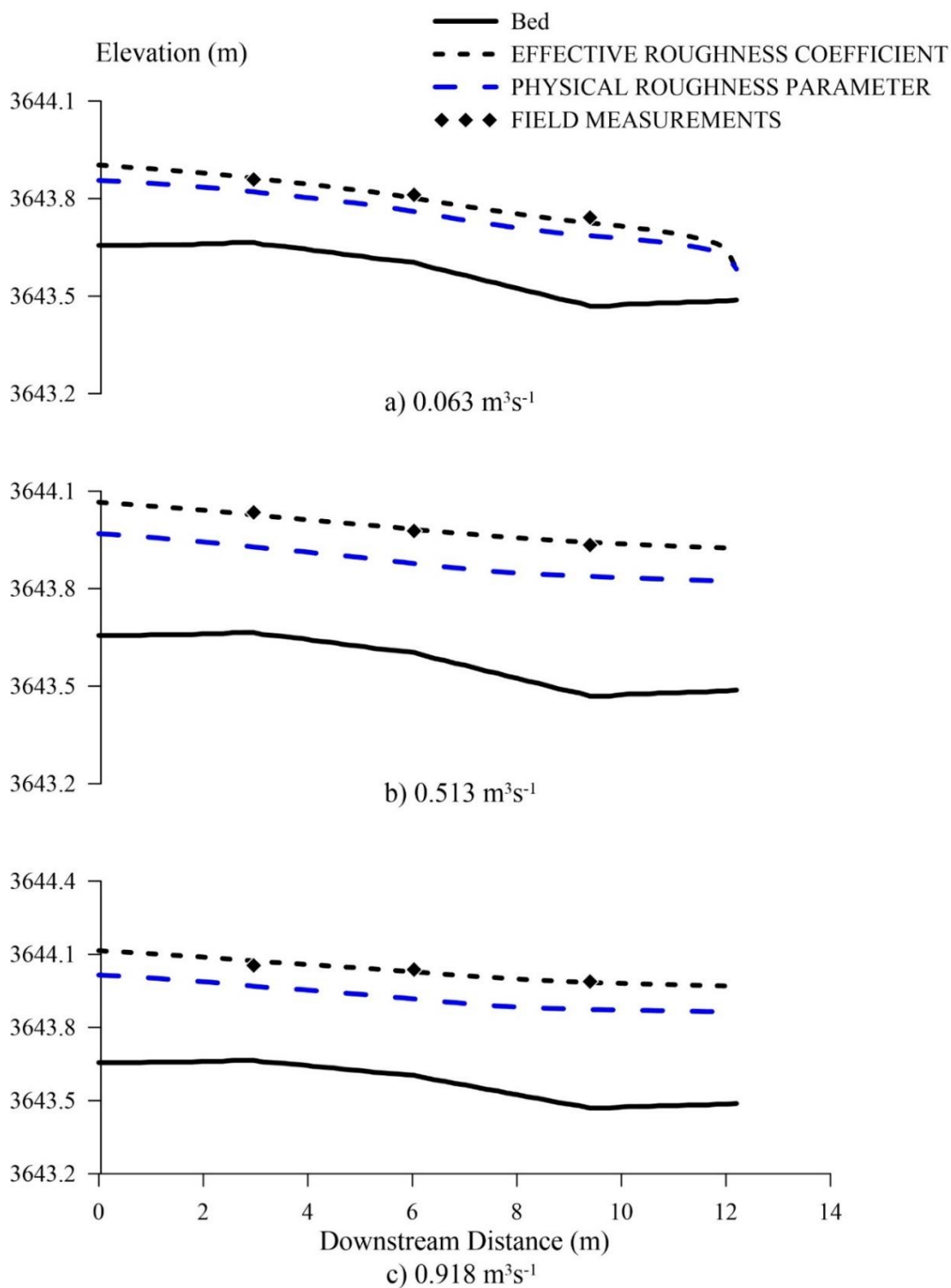


Figure 4.8: Water surface profiles using ERC and PRP in Plane-Bed. a) $0.063 \text{ m}^3\text{s}^{-1}$ b) $0.513 \text{ m}^3\text{s}^{-1}$ c) $0.918 \text{ m}^3\text{s}^{-1}$

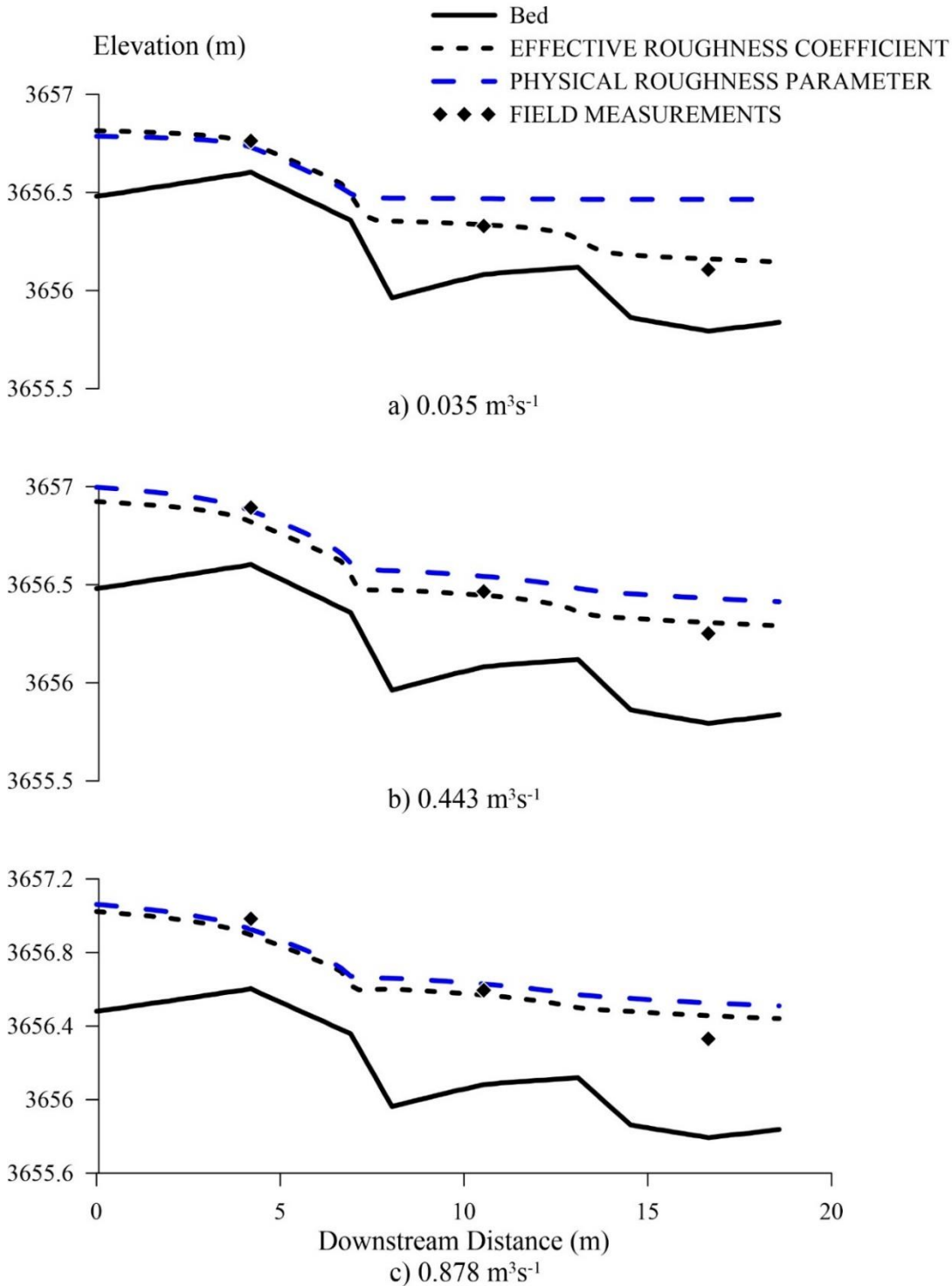


Figure 4.9: Water surface profiles using ERC and PRP in Step-pool. a) 0.035 m³s⁻¹ b) 0.443 m³s⁻¹ c) 0.878 m³s⁻¹

4.4 Discussion

4.4.1 Likelihood curves

Figure 4.4 shows that plane-bed for all flows (Figures 4.4d–f) and step-pool for high flows (Figure 4.4i) have two likelihood curves. The right-sided likelihood curve in plane-bed is formed when, in the solution, the HEC-RAS numerical model presents the critical depths as a response. This response occurs when, in the iterative process of solving the energy equation, a solution is not found under a specified tolerance given a maximum number of iterations. Note that a critical depth response is not expected in this morphology. Likewise, the curve on the right

side in step-pool is formed by the critical depths as responses from the numerical model. The shape of this likelihood curve does not allow a maximum value to be obtained, and it is ignored for analysis.

4.4.2 Likelihood peak values

In the 1-D numerical approach, horizontal water levels in the XS are assumed (Brunner, 2021); however, this assumption deviates from reality at certain morphologies in the headwater of mountain rivers.

The bed of cascade has randomly distributed large clasts (Montgomery & Buffington, 1997). The water interaction with boulders or cobbles produces both a jet flow and a wake flow around the particles, forming eddy currents behind obstacles, whereas the flow above the described particles produces a tumbling flow (Jarrett, 1984; Montgomery & Buffington, 1997). The physical process described contrasts with the measured water level at a single point near the bank, resulting in low performance in the outputs of the numerical model, and thus in low peak likelihood values for all flow magnitudes (~0.6 according to Table 4.1).

Plane-bed flow is closer to the 1-D numerical model assumptions as there are no bedforms, there is no tumbling flow, a (Montgomery & Buffington, 1997), leading to the representative water level measurement of the XS and the high peak likelihood values (~0.9 according to Table 4.1).

Step-pool presents a staircase shape (where risers are steps and pools are treads) with a tumbling flow pattern (Chin & Wohl, 2005). Water levels are measured in pools. At low flow, the effect of water plunging into pools does not produce a significant free-surface variation, while, as the flow increases, there is an appreciable free-surface variation. This causes the horizontal water level assumption to be invalid. This is the explanation behind the decline in the likelihood peak starting with a value of 0.9 at low flow and decreasing to 0.6 for high flow.

4.4.3 Friction slope methodology

Two studies were found in the literature investigating the influence of RFSM on the model performance when the energy equation is used. Laurenson (1986) tested different RFSM performances using analytical data. The validation data consisted of water levels from a cubic equation. According to this analysis, AFSE is the best and safest methodology to predict water levels. Artichowicz & Mikos-Studnicka (2014) tested four theoretical cases in a prismatic channel (three tranquil flows and one rapid flow) using the solution of the differential energy equation as validation data. In this study, the analyzed RFSM included all the methodologies available in HEC-RAS and some additional methods available in the literature. AFSE was the best methodology for tranquil flow; on the other hand, HMFSE was the best methodology for rapid flow. There are important differences between previous studies and the current study. First, the selection of the RFSM methodology does not influence most of the GLUE results except for cascades and step-pools at low flows (see Table 4.1). The cascade reach in this research could be considered similar to the rapid flow case in Artichowicz & Mikos-Studnicka (2014). However, in our study, the best RFSM for cascade at low flow was AFSE (Eq. (4.6)), unlike the HMFSE (Eq. (4.8)) obtained by Artichowicz & Mikos-Studnicka (2014). A possible explanation for this difference might be that the Artichowicz & Mikos-Studnicka (2014) test is performed in a prismatic flume without bed material, while cascade has boulders and cobbles interacting with the flow. Furthermore, the cascade results agree with Laurenson (1986) who advised AFSE. A case similar to step-pool could not be found in the literature. The best-performing RFSM for low flow was GMFSE (Eq. (7)). The authors believe that GMFSE is superior due to its resilience to outliers (Dodge, 2008); in this morphology, it is important that tumbling flow produces abrupt changes in the friction slope. In addition, neither Artichowicz & Mikos-Studnicka (2014) nor Laurenson (1986) had, in their study, big particles in the riverbed as in our case.

HEC-RAS chose RFSM (Experiment 2) based on both the profile type when it is subcritical or supercritical and the magnitude of the friction slope of the previous XS (Brunner, 2021). However, it seems that high slopes, large-scale resistance elements, slope breaks, or tumbling flow produce the same water levels for any resistance when this option is chosen, thus losing physical realism. Nevertheless, the use of this option in the plane-bed produced the same results as using any other of the four available methodologies. This could mean that the automatic selection of RFSM could be conditioned to lowland rivers.

4.4.4 Effective resistance coefficient (ERC) and physical resistance parameter (PRP)

Several GLUE studies on cascade, plane-bed, and step-pool were not found, as indicated by the relatively low number of references in the Introduction section; therefore, it is not possible to compare the likelihood curves with

other references. Moreover, none of the studies found in the literature made a comparison between effective and measured resistance values.

ERC contains the same energy dissipation process as PRP (Bhola et al., 2019; Wohl, 2013), but 3-D effects and geometry errors are not represented in the used 1-D model. Furthermore, in this study, the effect of inaccuracies in geometry is minimal due to the high precision of the used measuring equipment (total station and differential GPS), and the consideration of strategic points (slope changes, before and after steps) was considered in the studied reaches to obtain data.

The parameter α in the energy equation (Eq. (4.3)) must be considered when comparing ERC and PRP. α assumes a value equal to 1 because there is inbank flow only (see Eq. (4.9)), so there is no correction, due to the three-dimensional characteristic of the flow.

4.4.4.1 Low flow

For low flow rates in plane-bed and steep-pool morphologies, the range of ERC values is above the range of PRP values (Figures 4.6b,c, respectively), contrary to what is presented in cascade (Figure 4.6a). Through linear interpolation of the data in Table 4.3, it was found that, on average, 40% of the bed material in all morphologies under study protrudes above the water level at low flow flows, having an important influence on resistance. In cascade, the water level shows an alteration due to the interaction of the water with the large clasts (David et al., 2010). A lower value of ERC with respect to PRP could mean that the numerical model requires the increase in velocity to account for the jetting flow effect around boulders and cobbles (Montgomery & Buffington, 1997). Plane-bed and step-pool depict a similar pattern when comparing ERC with PRP. The water surface variation is significantly lower in plane-bed than cascade because there are fewer boulders and cobbles (see Table 4.3), and the flow velocity is lower, so the resistance is smaller. At step-pool, there is flow division at steps, so water plunges into the pool at multiple points, reducing the water surface variation. The higher ERC relative to PRP in plane-bed and step-pool may be due to the need of the model for a lower velocity.

Table 4.3: Bed material quartiles and mean depth for each morphology and flow magnitudes.

Site	Flow ($\text{m}^3 \text{s}^{-1}$)	d_{mean} (m) ¹	D_{50} (m) ²	D_{75} (m) ²	D_{84} (m) ²	D_{95} (m) ²
Cascade	0.065	0.145				
	0.485	0.282	0.0959	0.2526	0.3465	0.6529
	0.708	0.336				
Plane-bed	0.063	0.108				
	0.513	0.211	0.0795	0.1458	0.2185	0.3285
	0.918	0.277				
Step-pool	0.035	0.11				
	0.443	0.29	0.092	0.1721	0.2512	0.4695
	0.878	0.329				

¹ d_{mean} is a representative water level in the reach considering the XS as rectangular. It is calculated with average geometric values for all the XS having a staff gauge and the continuity equation; ² D_{xx} is the xxth percentile of grain size distribution.

4.4.4.2 Mid to high flow

According to Figure 4.6, the different pattern between ERC and PRP was preserved except for step-pool having the same pattern as cascade rather than the previous plane-bed pattern. In step-pool, as the flow increases, both ranges approach each other and overlap for the highest flow tested. The changing difference between ERC and PRP in step-pool may be attributed to a higher water surface deformation during tumbling flow. A higher flow leads to less flow division at steps, so there is a concentrated amount of water plunging into the pool. In cascade (Figure 4.6a), the bounds of ERC and PRP intersect for mid and high flow, but in plane-bed (Figure 4.6b), both ranges do not overlap. The possible reason could be the presence of vegetation near the main channel in plane-bed as can be observed in Figure 4.3c. At mid and high flows, the leaves of the vegetation interact with water, increasing flow resistance. This phenomenon cannot be represented in the model, so ERC may need to be modified to account for it.

4.5 Conclusions

The difference between the effective (ERC) and physical (PRP) resistance values of three typical morphologies found in mountain rivers (cascade, plane-bed, and step-pool) was analyzed. River flow, mean velocity, topographic data, water levels, and wetted width were monitored, and the measured resistance was estimated based on the average of the cross-sectional data. An effective value of the resistance parameter was derived in two GLUE experiments using the HEC-RAS controller to automate the simulations. The comparison between effective and physical resistance was limited to three flow magnitudes: low, mid, and high, because of the computational power required for the GLUE experiments and the available field data. The likelihood function was a combination of two measures of the mean residual and one measure of the standard deviation of residuals.

The research yielded two important findings. First, the RFSM influence (Experiment 1) on hydrodynamic models was limited to low flows. The results of the step-pool model were the most affected when different methodologies were used, and as a result, four different likelihood curves were found. When HEC-RAS selected the RFSM (Experiment 2) only for plane-bed, acceptable results were found. In cascade and step-pool, equifinal values were obtained for all resistance values, losing physical significance. Second, the highest difference between ERC and PRP was at low flows. As the flow increased, the difference between ERC and PRP ranges decreased and, in some cases, even overlapped. Cascade and plane-bed had opposing patterns when ERC was compared with PRP bounds, while step-pool ERC and PRP patterns depended on the flow magnitude. ERC is a key element in a hydrodynamic model, so a careful selection of the ERC value must be pursued considering morphologies and flow data. Future research could include a wider range of flow magnitudes to compare the different tendencies between effective and physical resistance values.

Chapter 5

5 Physics-informed neural network scheme to calibrate flow resistance in 1d steady-state open channel cases

Redrafted from:

Cedillo, S., Núñez, A.-G., Sánchez-Cordero, E., Timbe, L., Samaniego E., Alvarado A. (2022) Physics-Informed Neural Network water surface predictability for 1D steady-state open channel cases with different flow types and complex bed profile shapes. *Advanced Modeling and Simulation in Engineering Sciences*. [Online] 9 (1), 10. Available from: doi:10.1186/S40323-022-00226-8 [Accessed: 30 June 2022].

Abstract: The behavior of many physical systems is described by means of differential equations. These equations are usually derived from balance principles and certain modelling assumptions. For realistic situations, the solution of the associated initial boundary value problems requires the use of some discretization technique, such as finite differences or finite volumes. This research tackles the numerical solution of a 1D differential equation to predict water surface profiles in a river, as well as to estimate the so-called resistance parameter. A very important concern when solving this differential equation is the ability of the numerical model to capture different flow regimes, given that hydraulic jumps are likely to be observed. To approximate the solution, Physics-Informed Neural Networks (PINN) are used. Benchmark cases with different bed profile shapes, which induce different flows types (supercritical, subcritical, and mixed) are tested first. Then a real mountain river morphology, the so-called Step-pool, is studied. PINN models were implemented in Tensor Flow using two neural networks. Different numbers of layers and neurons per hidden layer, as well as different activation functions (AF), were tried. The best performing model for each AF (according to the loss function) was compared with the solution of a standard finite difference discretization of the steady-state 1D model (HEC-RAS model). PINN models show good predictability of water surface profiles for slowly varying flow cases. For a rapid varying flow, the location and length of the hydraulic jump is captured, but it is not identical to the HEC-RAS model. The predictability of the tumbling flow in the Step-pool was good. In addition, the solution of the estimation of the resistance parameter (which is an inverse problem) using PINN shows the potential of this methodology to calibrate this parameter with limited cross-sectional data. PINN has shown potential for its application in open channel studies with complex bed profiles and different flow types, having in mind, however, that emphasis must be given to architecture selection.

Keywords

Neural Network, Physic Informed Neural Network, Open Channel, Step-pool, Mountain River, Complex geometry

5.1 Introduction

Besides its extensive use for classification problems and for the search of patterns in data, Machine Learning techniques (ML) have shown a great capability as surrogate models to approximate the behavior of both artificial and natural systems. ML can find non-linear complex spatio-temporal functional relations for the big-data regimes (Rao et al., 2020; Tartakovsky et al., 2020). Nevertheless, ML has certain drawbacks affecting its performance. Firstly, it does not consider the system physics. Secondly, it depends on the quantity and quality of data to be robust and to attain convergence (Raissi et al., 2017b; Rao et al., 2020). In fact, in natural systems, the available data may be scarce because of the difficulty of measuring. To address this challenge, machine learning techniques can take advantage of the knowledge embedded in the laws of physics (Tartakovsky et al., 2020). This notion leads to the approach known as Physics-Informed Machine Learning. In particular, Physics-Informed Neural Networks (PINN) have been applied to solve both forward and inverse problems. Forward problems deal with the solution of Initial Boundary Value Problems (Mao et al., 2020; Raissi et al., 2017a). An inverse problem tackles the inference of quantities of interest such as parameters or hidden states of a system using a limited and potentially noisy set of observed data (Mao et al., 2020; Raissi et al., 2017a, 2017b).

An interesting feature of PINN is that the evaluation of derivatives is performed through automatic differentiation (AD) (He & Tartakovsky, 2021). AD consists of a family of techniques in which the evaluation of derivatives is exact without resorting to symbolic differentiation (Güneş Baydin et al., 2018). In addition, PINN does not require discretization points. In that sense, it can be classified as a meshless method. Collocation points, where the differential equations are evaluated, need to be provided (Raissi et al., 2017b).

Physics-informed machine learning has been used in many studies related to hydrodynamic (Raissi, Perdikaris, et al., 2018; Wang et al., 2020). Mao et al. (2020) solved 1- D and 2- D Euler equations for high-speed aerodynamic flow with Physics-Informed Neural Network (PINN). The results were not superior to traditional techniques for forward problems, but PINN results were superior in inverse problems. Guo et al. (2020) tested PIDL prediction capacity to solve different partial differential equations (PDE): 1- D wave equation, kdV Burger's equation, and Two-soliton solution of the Korteweg-De Vries Equation. In all cases, PIDL provides good predictability. However, the authors have not been able to find any application of PINN for mountain rivers. The modeling of a mountain river reach is a challenging task (Papanicolaou et al., 2004). A mountain river model must be able to deal simultaneously with Gradually Varied Flows (GVF, either only subcritical or only supercritical) and Rapid Varying Flows (RVF, transcritical: both subcritical and supercritical regimes are observed) (Sart et al., 2010). GVF present a slow variation of the flow depth profile with parallel streamlines. RVF have a fast change of water depth with streamlines having a pronounced curvature producing discontinuities in the solution (hydraulic jumps). RVF can produce spurious oscillations around discontinuities in a numerical model (Berger & Stockstill, 1995; Papanicolaou et al., 2004). To explore the ability of PINN to deal with these problems, different open channel cases with increasing complexity have been tested in this study.

The first two benchmark cases present GVF, where the solution is smooth. Thus, these cases were helpful to ensure that the developed PINN method provide correct answers. The next two benchmark cases deal with RVF. These cases were used to test the solution stability in case of discontinuities, which is crucial for the real cases. For RVF, two transitions were tested: supercritical to subcritical and subcritical to supercritical. All the previous cases give a clear picture of the PINN predictability performance. Then, it was tested in a more complex application: A mountain river reach. The natural system under analysis was a morphology called Step-pool, which is frequently found in mountain streams when bed slope varies from 0,04-0,2 (Maxwell & Papanicolaou, 2001). Step-pools are an alternation of step-pool units having a stair-case shape (Maxwell & Papanicolaou, 2001). A step-pool unit has a step commonly formed by boulders and cobbles but other materials such as large wood debris or bedrock are also found (MacFarlane & Wohl, 2003), and a pool having finer material (Maxwell & Papanicolaou, 2001). This morphology regulates flow resistance through a tumbling flow (MacFarlane & Wohl, 2003). A tumbling water flow, over or through steps, is supercritical until it falls into a pool and changes to a subcritical flow after a hydraulic jump (Chin & Wohl, 2005). Below steps is the place with the higher turbulence producing energy dissipation due to roller eddies, hydraulic jumps and velocity fluctuations (Chin & Wohl, 2005; MacFarlane & Wohl, 2003).

In this study, the steady case is considered, so the Energy Differential Equation (EDG) is used. The same equation is solved for this case by a widely used hydrodynamic model HEC-RAS (Brunner, 2021). EDG is expected to work well for GVF. However; EDG is not valid in RVF (Brunner, 2021), so spurious oscillations are expected. Indeed, the well-known software HEC-RAS uses a steady version of the momentum equation under some RVF conditions.

The goals of this Chapter can be listed as follows:

- To correctly solve the conservation equation using PINN for Rapidly and Gradually Varying Flows (RVF, GVF) in open channels with complex profiles in benchmark and real cases
- To use the previous experience to calibrate the resistance parameter using PINN with limited field data measurements

The remaining of this article is organized as follows. Section 2 provides the materials and methods applied in this article, including a description of the five studied cases, the PINN architectures implemented, a description of the HEC-RAS model and the metrics to compare PINN and HEC-RAS results. Section 3 compares the results of different PINN architectures, taking the HEC-RAS model as a baseline. An analysis of the performance of activation functions, neural network dimension, and PINN predictability is done in the Section 4 (Discussion). Section 5 highlights the main findings in the current research.

5.2 Materials and methods

5.2.1 Cases under study

5.2.1.1 Benchmark cases

PINN predictability was tested for four benchmark open channel cases with prismatic cross sections for the forward problem. Each case has different bed shapes producing different water surface profiles. The main idea is to test the ability of the method to approximate the solution of the differential equation for different flow regimes. Case 1 is

intended to represent the longitudinal profile of a river with a changing bed slope (Artichowicz & Mikos-Studnicka, 2014). Figure 5.1a depicts the bed profile having different inflection points. The cross-section is rectangular with a width (B) of 10 meters, a Manning's resistance value (n) of 0.03, and a flow (Q) of $15 \text{ m}^3 \text{ s}^{-1}$. In this case there is GVF in the whole channel; moreover, the flow regime is known to be subcritical.

Case 2 represents a case of rapid flow in a spillway where the slope increases downstream (Refer Figure 5.1b)(Artichowicz & Mikos-Studnicka, 2014). The flow regime in this case is also GVF, but now it is supercritical. The cross-section and Manning's resistance values are the same as in Case 1, but the flow is $22 \text{ m}^3 \text{ s}^{-1}$.

Figure 5.1c shows the profile for Case 3, which consists of two parts separated by an inflection point. The first part is 200 meters long with a slope of 0.025. The second part is 600 meters long, having a slope of 0.0002. The sudden change in bed slope results in the presence of a hydraulic jump (a transition from supercritical to subcritical flow), i.e., a RVF. The cross-section in this reach is trapezoidal with a base of 2.5 meters, a lateral slope of 0.8, n is 0.012, and the flow is $25 \text{ m}^3 \text{ s}^{-1}$.

Figure 5.1d depicts Case 4. It is composed of two reaches. The first reach is 1000 meters long with a slope of 0.0006, and the second one is 200 meters long with a slope of 0.015. The sudden slope increase produces the flow depth profile to suddenly decrease, passing from subcritical to supercritical flow, a RVF as in the previous case. As in Case 3, Case 4 has a trapezoidal cross-section with a width of 1 meter, a lateral slope of 1, an n value of 0.018 and a discharge of $6 \text{ m}^3 \text{ s}^{-1}$.

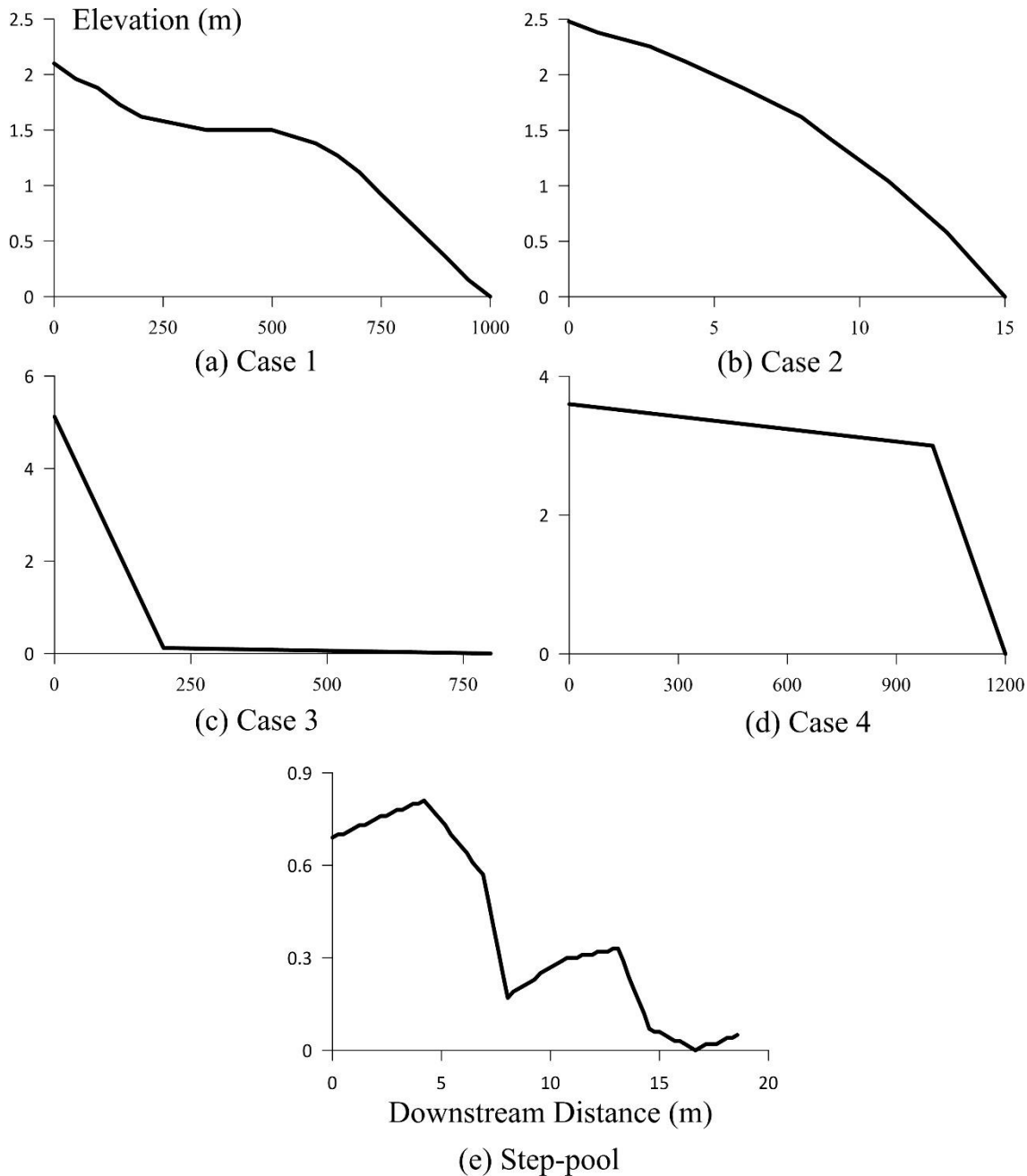


Figure 5.1: . Bed profile for different cases. Benchmark cases: (a) Case 1, (b) Case 2, (c) Case 3, (d) Case 4, Real Case: (e) Step-pool

5.2.1.2 Real case

Figure 5.1e depicts the profile of the step-pool under study having two step-pool units. The chosen morphology to be studied is Step-pool 1 in Figure 5.2. This is part of a hydraulic observatory where different morphologies are studied in the headwaters of the mountain Quinuas river, in Southern Ecuador. This reach is 12.22 meters long and has a mean slope of 6.1%. Moreover, this Step-pool has been used in previous studies by the authors (Cedillo et al., 2021a, 2021b). The available data consist of mean velocity and water depth for different flow magnitudes so that different flow resistance conditions can be studied. Moreover, topography and bed composition are available as well. This kind of morphology has been selected for its flow characteristics, as mentioned in the Introduction, given that its prediction poses a challenge to any numerical model.

Three flow magnitudes have been chosen for the current research based on the data available in Cedillo et al. (2021b): $0.035 \text{ m}^3\text{s}^{-1}$, $0.443 \text{ m}^3\text{s}^{-1}$, and $0.878 \text{ m}^3\text{s}^{-1}$ with the respective effective resistance coefficients: 0.414, 0.193, and 0.134.

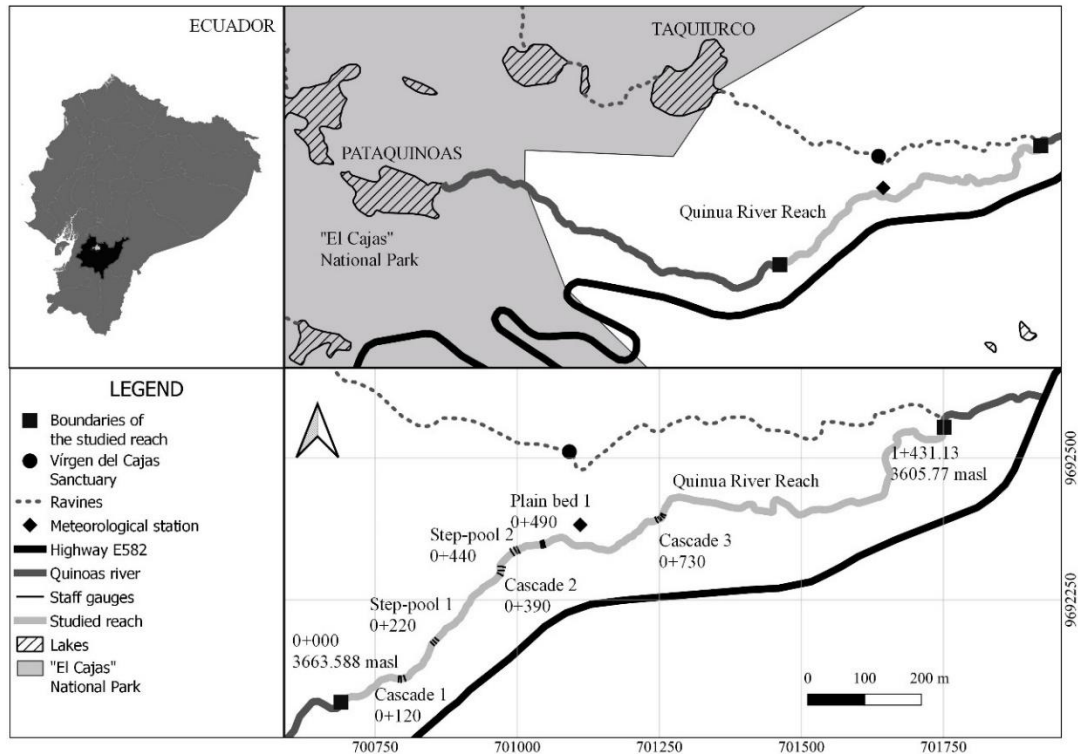


Figure 5.2: Plan view of the studied 1500 km river reach showing the sequence of the sub-reaches and the location of the meteorological station.

5.2.2 Physics-informed neural network (PINN)

5.2.2.1 PINN: an alternative for the calibration of the resistance parameter

In this chapter, we look for an alternative methodology to calibrate the resistance parameter with limited field data for one dimensional steady state flow. As a first step to attain this goal, we search for a way to solve the corresponding differential equation with a methodology that can be easily adapted for calibration. Physical informed neural networks (PINN) emerge as a very interesting possibility. The idea is to approximate the solution of the differential equation taking advantage of neural networks as universal function approximators (Raissi et al., 2017b). Then, in a second step, we use PINN to consider the inverse problem of optimizing parameters using observations, i.e., calibration. These two steps are explained further below.

Step 1. We verify that the conservation equation used in one dimensional steady state flows (a Differential Equation (DE) of first order) is solved correctly with PINN. This is called the “forward problem” in the seminal work of Raissi et al. (2017b). Deep neural networks are used to approximate the solution of the DE. It is important to notice that, in this context, neural networks are regarded as solution approximators instead of their usual role as a tool to perform some kind of regression based on a set of given data. Furthermore, Cuomo et al. (2022) show that the generalization error is bounded by the training error, so overfitting is not an issue in PINN. Hence, the training process in PINN corresponds to finding a numerical approximation of the solution of the DE. Indeed, the prescription of the conservation equation in PINN is attained by one of the terms of the loss function. The other terms take care of the geometry and the boundary conditions. During the process of verification, the deep neural network approximation of the Differential Equation solution is compared with the one found by the software HEC-RAS®. This widely used program solves the conservation equation using finite differences and is regarded as a base-line for comparison.

Step 2. Based on step 1, PINN is used to calibrate the resistance factor using limited measured data. This constitutes an inverse problem, as mentioned by Raissi et al. (2017a). In this step, one can realize the potential of PINN to go from solving the equation (the forward problem) to calibration (the inverse problem): only a change in the loss function is needed. Instead of a boundary condition term, a term that includes the measured data is considered. Thus, the PINN training process approximates the solution of the DE while providing the resistance parameter that fits the observed data at the same time. The verification consists in the comparison of the resistance parameter calibrated with PINN with the one obtained with the GLUE method. It is important to notice that the fact that the physics of

the phenomenon is included for the training of the neural network is likely to compensate for the limited availability of field data.

5.2.2.2 PINN schemes

The schemes shown in Figure 5.3 schematizes the PINN architecture used for our study in multiple cases. The PINN models were implemented in TensorFlow ® (Abadi et al., 2016). The code is based on the one shared by Raissi, Perdikaris & Karniadakis (2017a). Following the procedure of Kissas et al. (2020), two fully-connected neural networks sharing hyper parameters were used. The first one deals with the complex geometry present in each case, the second one is for the prediction of water depth. Each described case was run with different PINN models varying the number of hidden layers (3,5,7, 9, and 11), the number of neurons per hidden layer (10, 20, 40, and 60) (the number of input and output neurons specified for each case is shown in Figure 5.3), and the activation functions: Hyperbolic Tangent (Tanh), ReLU, Sigmoid, and Sin. Tanh is a zero-centered AF whose output varies between -1 and 1 (Ding et al., 2018).

According to Nwankpa et al. (2018), this aids in backpropagation. Tanh suffers saturation when the input tends to $\pm \infty$, resulting in a vanishing gradient where the weights are not updated during backpropagation (Ding et al., 2018). ReLU output is always positive (Sharma et al., 2020), producing bias in the next layer (Ding et al., 2018). Moreover, it is left-hand saturated, and only a certain number of neurons are active (Nwankpa et al., 2018). Sigmoid values range between 0 to 1 (Sharma et al., 2020), which has the same bias problem as ReLU. The Sin AF has been selected based on Goodfellow et al. (2016), who advise not to limit the considered AF's to popular ones.

In the forward problems Figure 5.3 a) and b), the main information for the loss function comes from the evaluation of the governing equation at collocation points. Water depth data is provided only at the boundary conditions (BC). The loss function is computed using the mean square error (MSE) metric, including the data at BC:

$$\text{Loss function} = \text{MSE}_{\text{BC}} + \text{MSE}_f + \text{MSE}_G \quad (5.1)$$

where

$$\text{MSE}_{\text{BC}} = 1/N_{\text{BC}} \sum_{i=1}^{N_{\text{BC}}} |h(x_{\text{BC}}^i) - h^i| \quad (5.2)$$

$h(x_{\text{BC}}^i)$ denotes the training data (water depths) at the boundaries, h^i are the predictions of PINN value at BC, and N_{BC} the number of training data;

$$\text{MSE}_f = 1/N_f \sum_{i=1}^{N_f} |f(x_f^i)| \quad (5.3)$$

x_f^i are the collocation points where the Differential Equation is evaluated and N_f is the number of collocation points;

$$\text{MSE}_G = 1/N_G \sum_{i=1}^{N_G} |z(x_G^i) - z^i| \quad (5.4)$$

x_G^i are points where the bed elevations are available, z^i are the predictions of geometric points of PINN, and N_G is the number of geometric points available.

The loss function depicted in Eq. (5.1) includes both data and the evaluation of the governing differential equation at collocation points. This combination has demonstrated to be exceptionally well suited for the solution of physical equations governing a given phenomenon, as well as for the corresponding inverse problem. The Energy Differential Equation (EDE) (Eq. (5.5)) was used as the main information for PINN since all the cases are run under steady-state conditions (Artichowicz & Mikos-Studnicka, 2014).

Step-pool brings an additional difficulty besides a complex profile: the cross-sections are not prismatic. Our proposed solution is to obtain an equivalent cross-section and then adjust cross sectional area (A) and hydraulic radius (R) data to an exponential equation which are used for discharge-stage relations. The computation of the equivalent cross-sections requires the following steps. First, cross-sections are measured at the studied reach; second, the cross-sections coordinates are translated so that the deepest point is located at the origin; third, each elevation of the equivalent cross-section is the geometric mean of the corresponding points of the measured cross-sections. Geometric mean is not sensible towards outliers (Dodge, 2008; Lovric, 2011) being useful in highly varied cross sections in natural rivers.

The scheme of the inverse problem is depicted in Figure 5.3 c) and it was solved for Case 5 only: The Step-pool. In this case, instead of having water depths at BC, there are water level measured at three points inside the domain.

Those values are used instead BC values in Eq. (5.2) so that this loss function component enforces measured field data. In the inverse problem, the water level profile as well as the resistance factor are found. The resistance values are compared with the effective resistance coefficients found in Cedillo et al. (2021b) with GLUE methodology. The scope of inverse problem is to analyze the predictive capacity of the resistance parameter under different resistance conditions and with limited cross-sectional data.

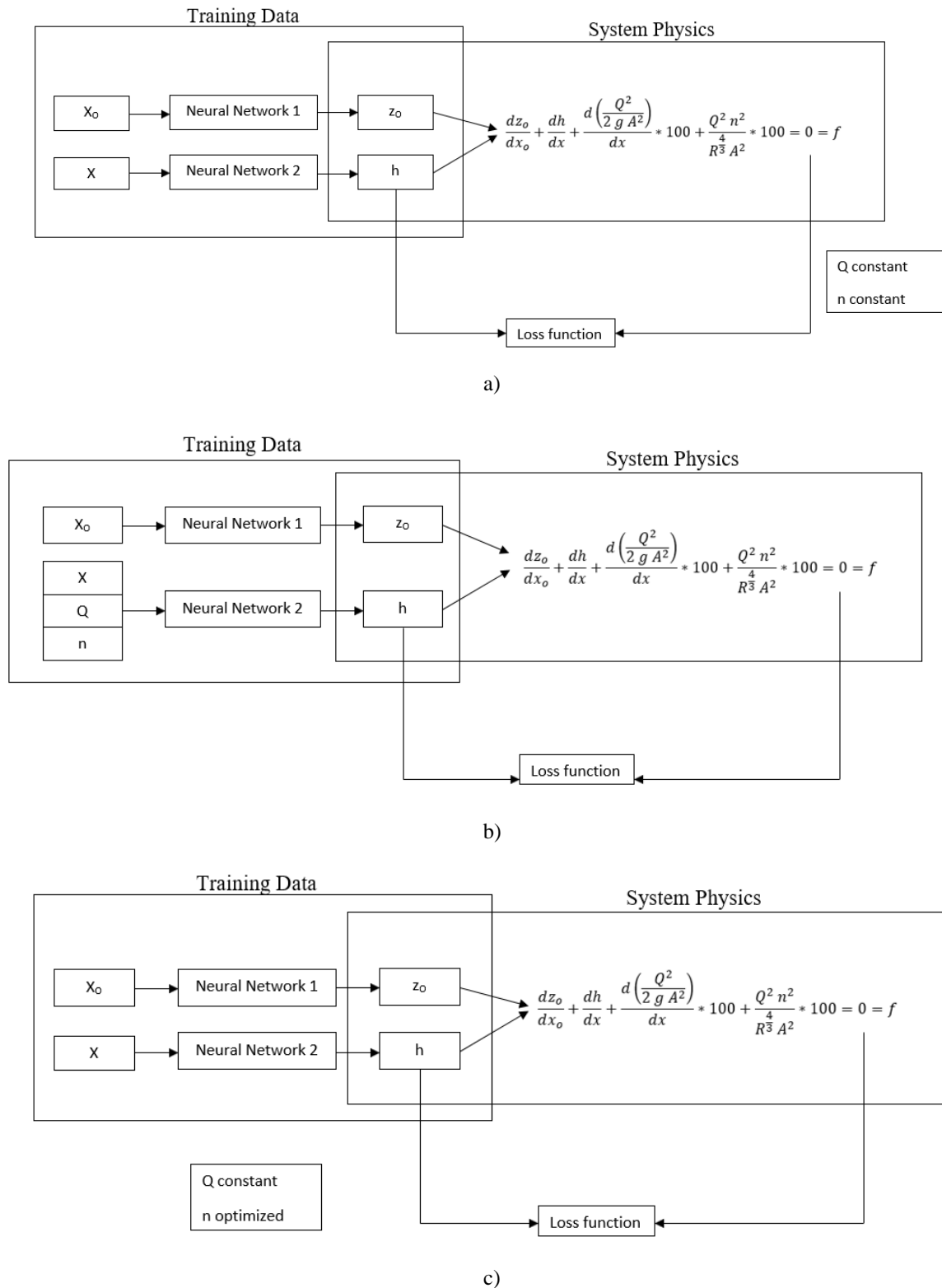


Figure 5.3: Physics-Informed Deep Learning schemes: a) Forward problem: Benchmark cases b) Forward Problem: Real Case c) Inverse problem: Real Case

5.2.2.3 Conservation equation

It is important to mention that the governing equation was written using centimeters as length units for the water depth and the bed level. This was necessary because during exploratory tests the resulting water levels of PINN did

not approximate correctly the analytical solutions (AS). Take into account that the way the PINN method enforces the different physical principles and constraints is by means of a loss function that has to be optimized. Thus, it is necessary for convergence that the terms of this loss function are of the same order of magnitude. In the above-mentioned exploratory studies, it was observed that gradients in the differential equation had a lower order of magnitude than other terms of the loss function. After the above-mentioned modification of units, PINN started converging to good solutions.

The Energy Differential Equation (EDE) has the following form:

$$\frac{dz_o}{dx_o} + \frac{dh}{dx} + \frac{d\left(\frac{Q^2}{2gA^2}\right)}{dx} * 100 + \frac{Q^2 n^2}{R^{\frac{4}{3}} A^2} * 100 = 0 = f \quad (5.5)$$

where z_o is the bed level (cm), x_o is the distance (m), h is the water depth (cm), Q is the flow m^3s^{-1} , R hydraulic radius (m), and A is the cross-sectional area (m^2). The first term in Eq. (5.1) represents the change in bed slope elevation (z_o) with the distance (x_o). The next term is the water depth slope, followed by the change in kinetic energy. The last term deals with the friction loss.

5.2.3 HEC RAS model

HEC-RAS® is a hydrodynamic model widely used in different studies (Bhola et al., 2019; Horritt & Bates, 2002; Papaioannou et al., 2017; Wohl, 1998). Furthermore, these model results have been used as the benchmark for PINN results. All the models have been run under steady-state conditions. Case 1 was run under subcritical flow, Case 2 was run with supercritical flow, and Case 3, Case 4, and Case 5 were run with a mixed flow regime. Under these conditions, HEC-RAS solves the energy equation between two consecutive cross-sections (Eq. (5.6)) (Brunner, 2021):

$$z_2+h_2+\alpha_2 U_2^2/2g=z_1+h_1+\alpha_1 U_1^2/2g+h_e \quad (5.6)$$

z_1 , z_2 are bed levels; h_1 , h_2 are water depth; U_1 , U_2 are velocities; α_1 , α_2 are velocity weighting coefficients; and h_e is the energy head loss. The parameter h_e has, in principle, two components: expansion or contraction losses and friction losses. All the studied cases have prismatic XS, so there are no expansion-contraction losses.

5.2.4 Direct step method

In Case 3 an additional solution method called “Direct Step Method” is used (Marriott et al., 2016). This method consists of the solution of The Energy Differential Equation (EDE) (Eq. (5.1)) by using finite differences. This methodology is applied in this case because of the discontinuity (hydraulic jump) location procedure used. The hydraulic jump location is determined through an iterative process where the initial depth upstream (y_i) and subsequent depth downstream (y_s) must coincide with the values of equation given by Marriott et al. (2016) which relate both values. This entails using an ad hoc strategy once hydraulic jumps are detected. For PINN, we do not use any ad hoc procedure.

5.2.5 Metrics

Three metrics are used to compare the PINN predictions and the HEC-RAS model results. Each metric analyzes different aspects of the difference between both models (residuals). First, Root Mean Square Error (RMSE) is an average of the residuals between PINN and HEC-RAS model, giving more weight to higher residuals (Chai & Draxler, 2014; Willmott & Matsuura, 2005). Second, MAE is an average of the residuals, where all the residuals have the same weight (Willmott & Matsuura, 2005). Third, the Nash-Sutcliffe efficiency index (EF) is a reliable and flexible metric used as an indicator of fitness goodness (McCuen et al., 2006; Merz & Blöschl, 2004; Nayak et al., 2013). Moreover, Ritter & Muñoz-Carpena (2013) provides a table to interpret the fitting quality based on the EF value. Both RMSE and MAE were divided by the mean of the observations and multiplied by 100 to have dimensionless metrics.

5.2.6 Systematic studies

In order to gain a deeper understanding of PINN as a numerical method for the solution of the differential equation treated in this study, we have performed several numerical studies in a systematic way to analyze both the rate of convergence and the robustness of the approach. For the latter, we have performed a sensitivity analysis.

5.2.6.1 Rate of convergence

The convergence rate in a numerical method can be determined by finding the relation between the log of the error norm of the solution (L_2 -norm (Jacquemin & Bordas, 2021)) and the discretization size (related to the number of

grid points). The slope of that relation is called rate of convergence. The rate of convergence indicates the rate at which the error decreases as the number of grid points increases (Fish & Belytschko, 2007).

As stated before, PINN does not have grid points, *sensu stricto*. Instead, it has the so-called collocation points, where the governing equations are imposed through the loss functions. Hence, we have computed different approximations of the solution with different number of collocation points. The L_2 -norm of the solution error was found for each run, allowing for the determination of rates of convergence for the different studied cases. This study was performed for each case with the activation function rendering the lowest loss function at convergence.

5.2.6.2 Sensitivity test

A sensitivity test has been performed by introducing a “perturbation” at the boundary conditions. That “perturbation” consist on a certain modification of the water depth values at the boundary condition: +/- 2%, +/- 4%, +/- 6%, +/- 8%, and +/- 10%. The idea is to see the effect of this perturbation on the solution.

5.3 Results

5.3.1 Equivalent cross-section

Figure 5.4 shows three different measured cross-sections of the Step-pool. In addition, that Figure also shows that the equivalent cross-section tends to follow a central tendency, where the outliers do not play an important role. Furthermore, Figure 5.5a and b shows both the Area and Hydraulic Radius of the equivalent cross-section fit well to an exponential equation having R^2 values higher than 0.9.

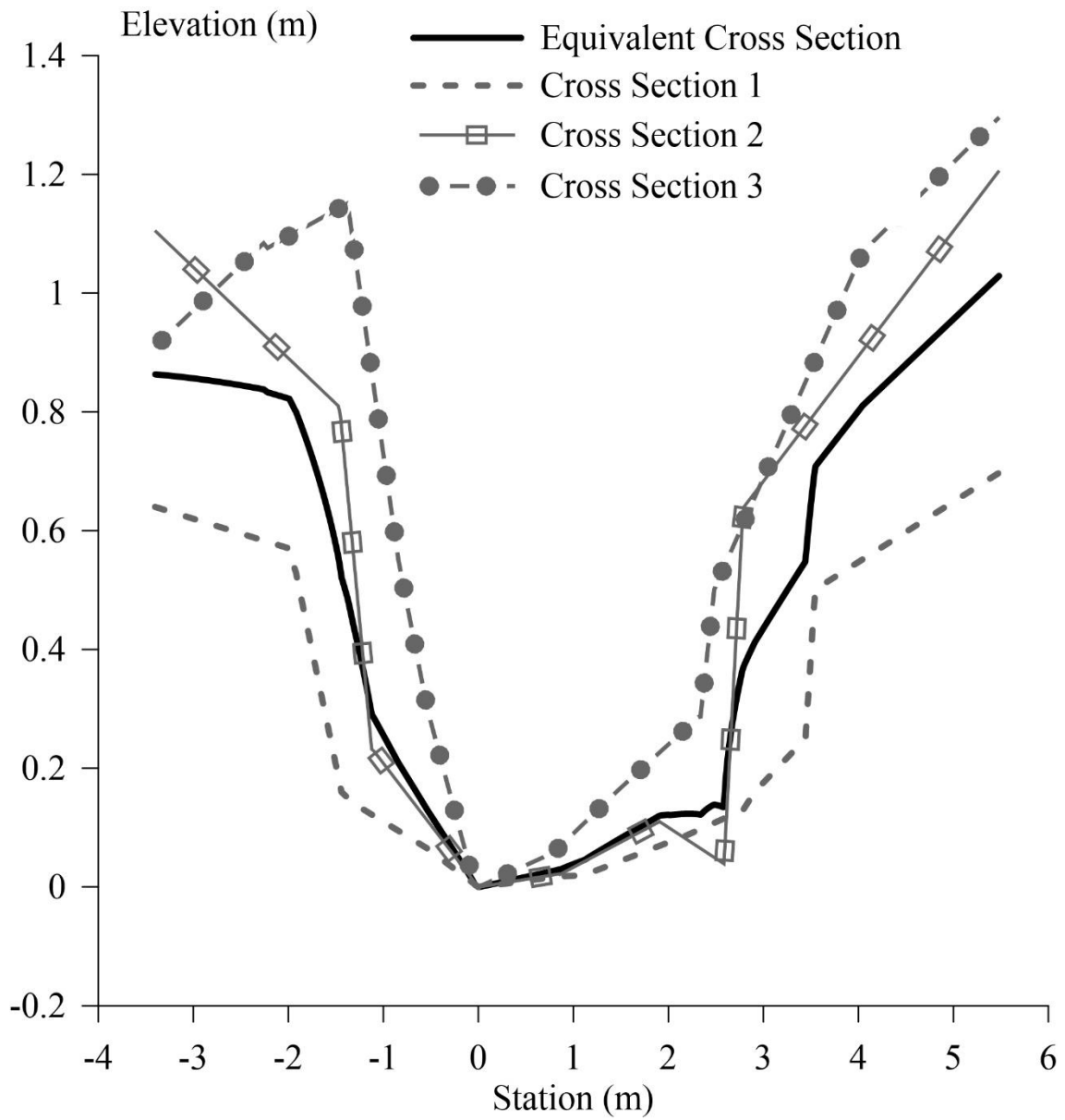


Figure 5.4: Cross sections in Step-pool and equivalent cross section

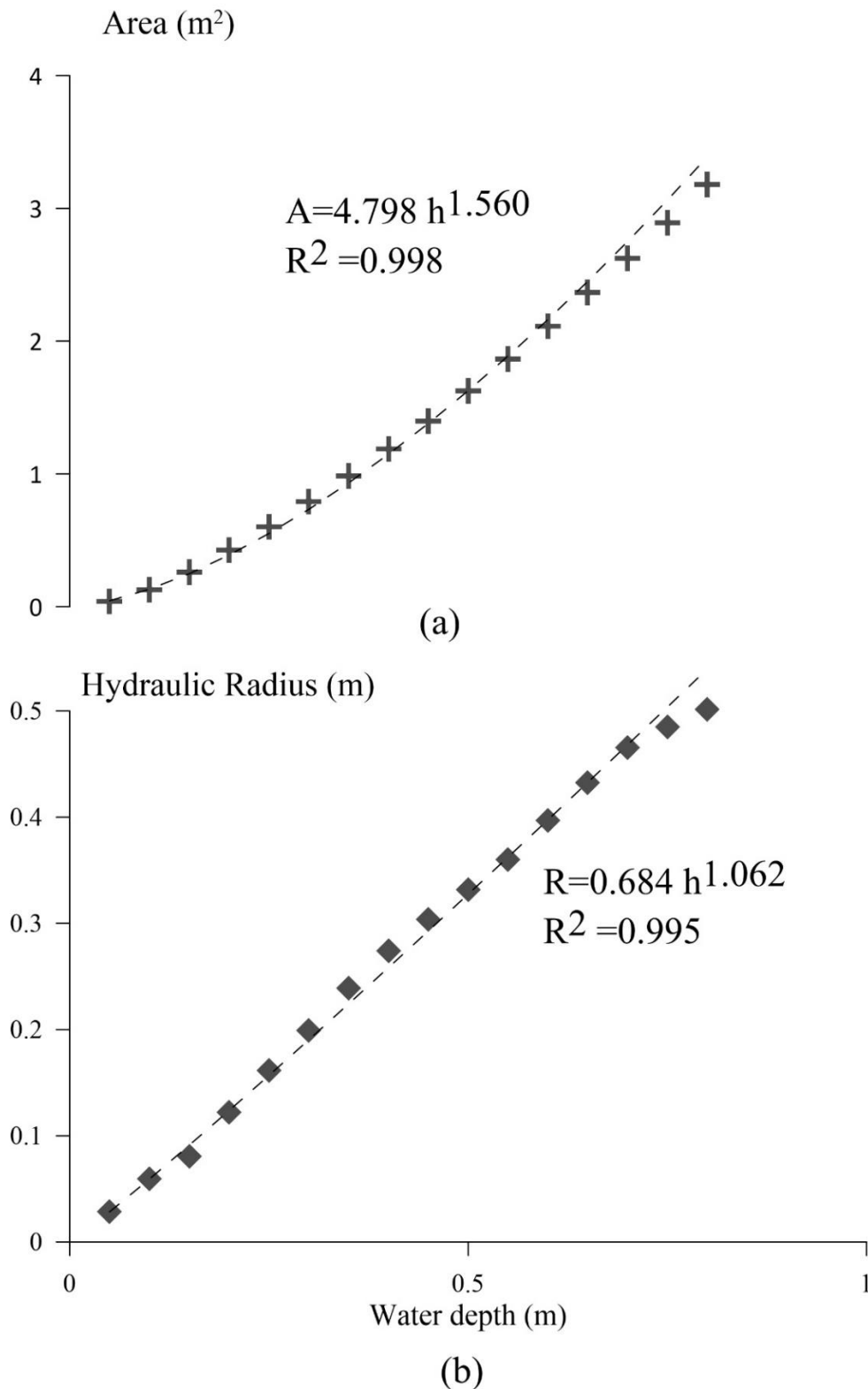


Figure 5.5: Area and Hydraulic Radius data of the equivalent cross-section. (a) Area, (b) Hydraulic Radius

5.3.2 Forward PINN: solving the differential equation

We analyze now the performance of PINN as a discretization method for a Differential Equation that models the behavior of a stationary 1D fluid in an open channel. The idea is to study several aspects of the approximation space subjacent to the PINN method, which is directly related to the architecture of the Neural Networks used. We start by analyzing the performance of several activation functions.

5.3.2.1 Activation function performance

Several PINN models were run with different combinations of number of layers (depth), neurons per layer (width), and activation functions (AF). We consider the best model for each AF as the one that has reached the lowest value for loss function during the training process.

The ReLU activation function is the one with the lowest predictive performance in all the cases under study, having the highest values of the RMSE and MAE statistics in cases where hydraulic discontinuities are present - RVF flow (refer to Table 5.1). Moreover, EF depicts that most of the ReLU models have a “Unsatisfactory” predictability except for Case 2 where the goodness-of-fit is “Very good” (Ritter & Muñoz-Carpena, 2013). Case 2 has the smoothest solution (GVF) with a constant descending pattern downstream (Figure 5.6b). The remaining cases have peaks and minima in the solution. Furthermore; Figure 5.6 and 5.7 display ReLU predicting a completely different response pattern than Sigmoid, Sin, Tanh, or HEC-RAS for benchmark as well as for the real case.

Looking at Table 5.1, the prediction quality of Sigmoid, Sin, and Tanh is almost the same for all the cases according to RMSE and MAE. Moreover, EF shows a “Very Good” goodness-of-fit for most studied Cases. However, in Case 3, these AFs provide “Unsatisfactory” predictions. The “Direct Step Method” provides the best fitting according to Table 5.1, with lower RMSE and MAE values than PINN results and an EF value of 0.796 rendering a fitting performance deemed as “Acceptable”. Figure 5.6c and d shows the presence of oscillations near discontinuities in benchmark cases with RVF when Sigmoid and Sin are used. Sigmoid, Sin, and Tanh have produced promising results predicting almost the same water depth profile in the real case (Figure 5.7a-c).

There are some predictability aspects to consider while using PINN. In Case 3 (Figure 5.6c), three of the activation functions, Tanh, Sin, and Sigmoid, were able to predict the presence of the discontinuity (hydraulic jump) downstream from the place where the HEC-RAS model predicted it. None of them was able to accurately locate the position of the discontinuity on the second part of the reach. The “Direct Step Method” was not able to predict the position of the hydraulic jump either, but it was the closest to the HEC-RAS result. In the real case (Case 5, Figure 5.7), the performance of PINN improves as flow increases according to RMSE and MAE values. Furthermore, the predictability of PINN in this real case is very good according to EF values (Ritter & Muñoz-Carpena, 2013) except for ReLU AF. However, Figure 5.7 presents discrepancies between the results of PINN and HEC-RAS which is not the case in benchmark cases.

Based on the above analysis, Tanh has been the activation function with the highest resilience for all the studied cases when an important number of collocation points are used. Thus, the analysis of the neural network's size will be based on the models using Tanh. On the other hand, ReLU has been the activation function with the worst performance providing acceptable water depth predictions only in Case 2.

Table 5.1: Best cases of activation functions based on loss function

Case	Activation Function	RMSE %	MAE %	EF	Hidden Layers	Neurons per hidden layer	Loss Function
Case 1	Tanh	0.53	0.42	0.999	7	60	4.57E-04
	ReLU	16.04	14.5	-0.138	7	60	1.15E-01
	Sin	0.99	0.77	0.996	5	40	3.77E-03
	Sigmoid	0.58	0.46	0.999	7	60	1.17E-03
Case 2	Tanh	2.23	2.07	0.988	5	20	2.25E-03
	ReLU	6.25	4.32	0.903	7	40	5.72E+00
	Sin	2.2	2.04	0.988	5	40	8.07E-03
	Sigmoid	2.24	2.08	0.988	7	60	1.86E-03
Case 3	Tanh	26.69	12.08	0.554	5	60	7.42E-04
	ReLU	42.95	39.65	-0.154	3	60	2.85E+00
	Sin	26.11	11.29	0.573	3	20	9.85E-02
	Sigmoid	25.4	12.91	0.596	3	40	5.78E-03
	Direct Step Method	18.05	4.85	0.796	-	-	-
Case 4	Tanh	1.76	0.93	0.997	3	20	2.61E-06
	ReLU	21.13	14.23	0.589	3	40	1.68E-01
	Sin	4.04	1.77	0.985	7	40	2.39E-06
	Sigmoid	4.56	2.67	0.981	7	60	1.56E-05
Case 5 Low Flow	Tanh	7.86	6.62	0.932	3	40	8.48E-02
	ReLU	27.49	18.48	0.171	7	60	4.48E+01
	Sin	6.56	5.88	0.953	7	60	9.87E-02
	Sigmoid	7.44	6.45	0.939	7	40	1.07E-01
Case 5 Mid Flow	Tanh	6.89	5.06	0.925	3	40	8.48E-02
	ReLU	21.22	14.69	0.291	7	60	4.48E+01
	Sin	5.18	3.89	0.958	7	60	9.87E-02
	Sigmoid	6.32	4.89	0.937	7	40	1.07E-01
Case 5 High Flow	Tanh	6.30	4.82	0.933	3	40	8.48E-02
	ReLU	19.90	13.55	0.328	7	60	4.48E+01
	Sin	4.90	3.67	0.959	7	60	9.87E-02
	Sigmoid	5.76	4.56	0.944	7	40	1.07E-01

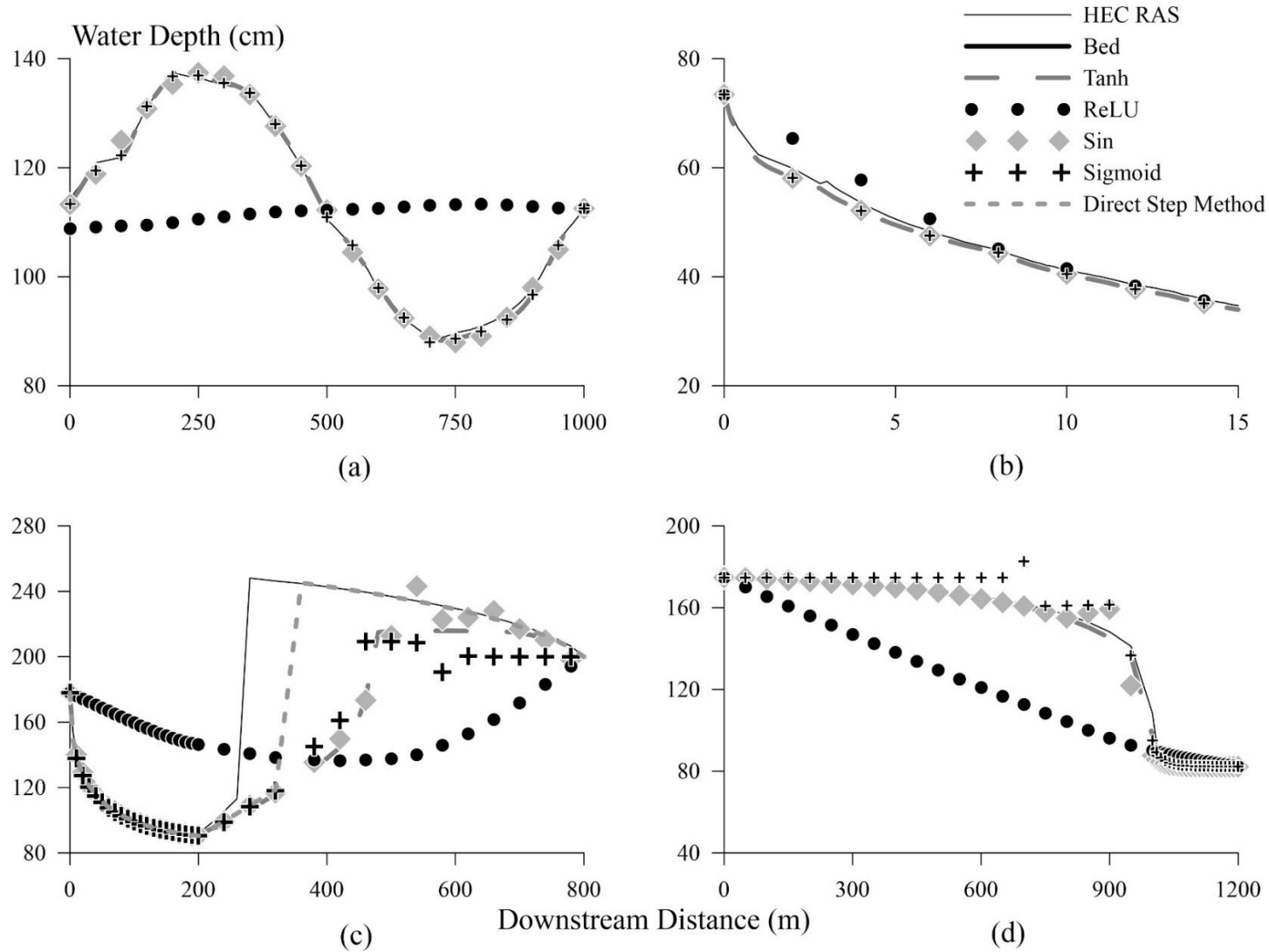


Figure 5.6: PINN results with the best case for each activation function for: (a) Case 1, (b) Case 2, (c) Case3, and (d) Case 4

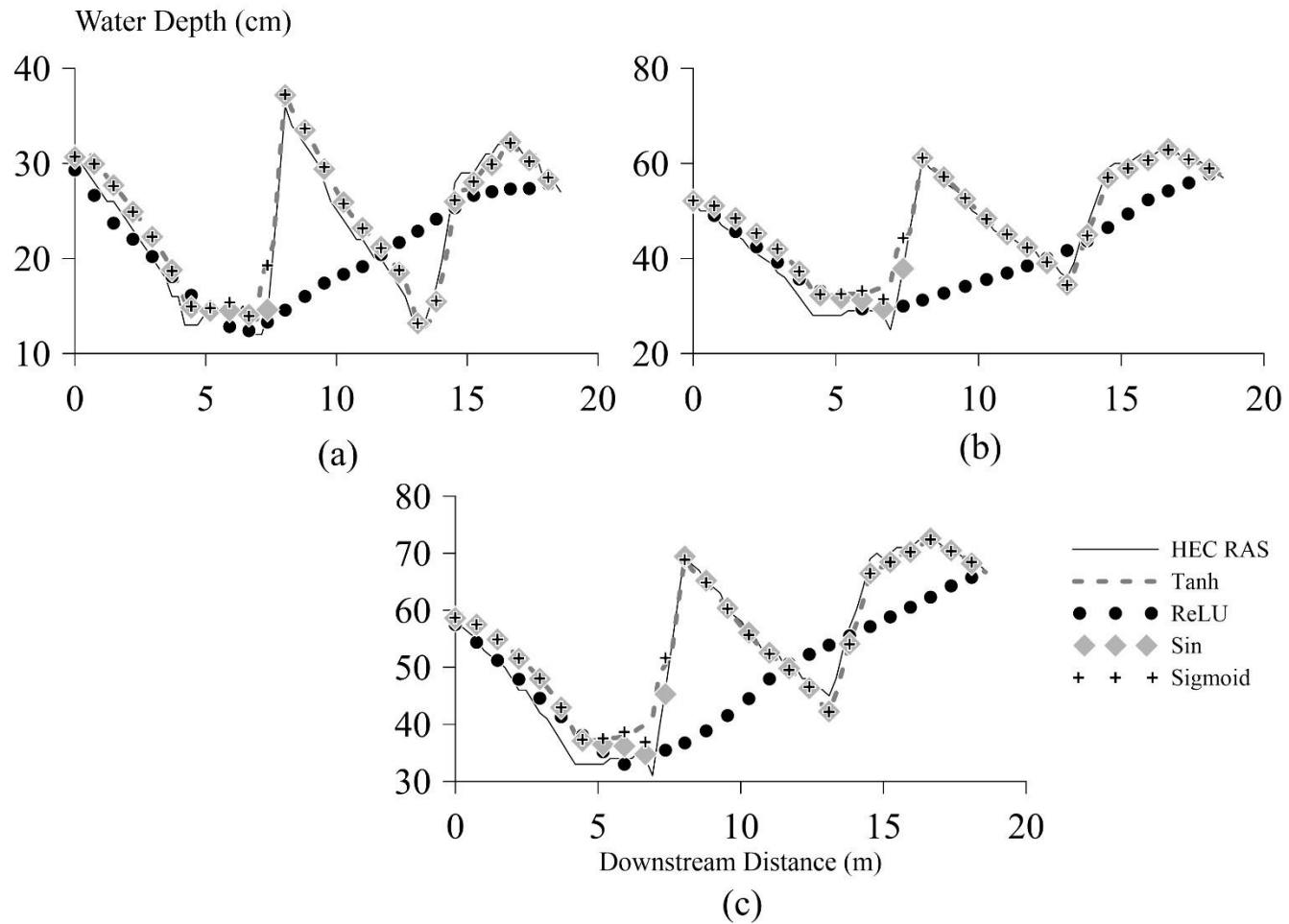


Figure 5.7: PINN results with the best case for each activation function for Step-pool: (a) Low flow, (b) Mid flow, and (c) High Flow

5.3.2.2 Neural network architecture

According to the previous section, the neural network architecture analysis is based on the best performing models, i.e., those using Tanh as AF. The optimal combination of hidden layers and neurons per hidden layer varies with the case under study. According to Table 5.1, a similar number of hidden layers are used in Cases 1, 2, and 3 having a variation of 5 and 7. However, the number of neurons per hidden layer ranges from 20 to 60. Case 4 has the lowest number of layers and neurons: 3 hidden layers with 20 neurons per hidden layer. Case 5 has 40 neurons per hidden layers being inside the range of Cases 1, 2, and 3, but the number of hidden layers is 3 which is lower than the previous mentioned cases. Moreover, it is important to notice that the remaining AFs in Case 5 are inside the number of hidden layers and neurons per hidden layer given by Cases 1, 2, and 3.

5.3.3 Inverse PINN

Figure 5.8 and Table 5.2 provides a comparison of the resistance values found by PINN with different AFs and the ones obtained through GLUE experiments (effective resistance) in Cedillo et al. (2021b). Figure 5.8 displays that PINN resistance values follow the descending effective resistance pattern as flow increases. For low flow, Table 5.2 shows that Tanh, Sin, and Sigmoid provide similar resistance values, but lower than GLUE results. Furthermore, ReLU gives a completely different resistance value, lower than the rest of models. For mid and high flow, all the AFs seem to provide the same resistance values close to the GLUE ones. Moreover, Table 5.2 depicts that ReLU results are not trustful because of the high loss function value being one thousand times higher than the rest of AFs.

Looking at Table 5.2, it is apparent that the hidden layers (ranging from 3 to 9) with the lowest loss function covers a wide range of the tested cases; however the number of neurons per hidden layer is rather limited to high values such as 40 and 60. Tanh, Sin and Sigmoid provides almost the same values for low and high flow, but at mid flow Tanh got a value which is inside the resistance value of GLUE experiment.

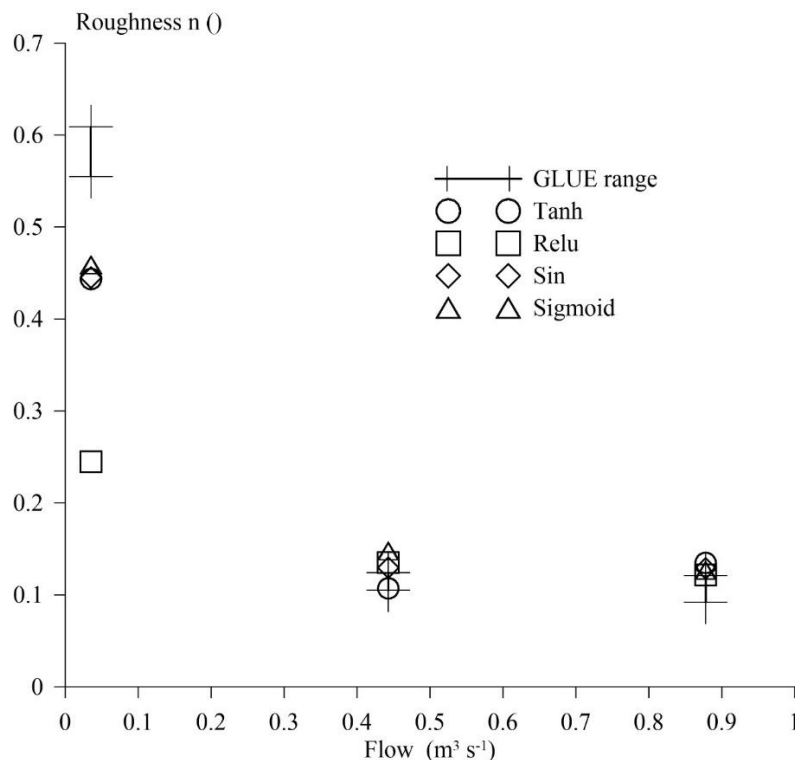


Figure 5.8: PINN results with the best case for each activation function for Step-pool, high flow

Table 5.2: Inverse PINN comparison between calibrated resistance values from GLUE experiments and the ones obtained from different AFs and different flow values

Flow (m ³ s ⁻¹)	n GLUE (Cedillo et al., 2021b)	Activation Function	n	Hidden Layers	Neurons per hidden layer	Loss Function
0.035	0.555-0.609	Tanh	0.444	3	60	0.024
		ReLU	0.245	9	60	21.275
		Sin	0.445	5	60	0.020
		Sigmoid	0.459	5	60	0.019
0.443	0.105-0.124	Tanh	0.107	7	60	0.025
		ReLU	0.135	7	60	27.487
		Sin	0.130	5	40	0.067
		Sigmoid	0.148	7	60	0.019
0.878	0.092-0.121	Tanh	0.135	3	60	0.024
		ReLU	0.122	9	60	28.317
		Sin	0.129	5	40	0.044
		Sigmoid	0.127	9	60	0.018

5.3.4 Results of the systematic studies

5.3.4.1 Rate of convergence

Figure 5.9a-c provides the plot of L_2 -norm against the number of collocation points used in PINN. The slope of each plot provides the rate of convergence. Cases with smooth solution have different rate of convergence depending on the flow regime. Case 2 (supercritical flow: shallow and rapid flow; see Figure 5.9b), has the highest rate of convergence: 1.4. On the other hand, Case 1 (subcritical flow: deep and slow flow; see Figure 5.9a) shows a rate of convergence of 0.4. Cases with discontinuities present different rates of convergence depending on the type of discontinuity. Case 3 (Figure 5.9c) and Case 5 (Figure 5.9e) discontinuity consist of a sudden water depth increase (hydraulic jump) having a rate of convergence of 0.2. In contrast, in Case 4 (Figure 5.9d) the discontinuity has a sudden decrease of water depth. This Case has a higher rate of convergence: 0.7.

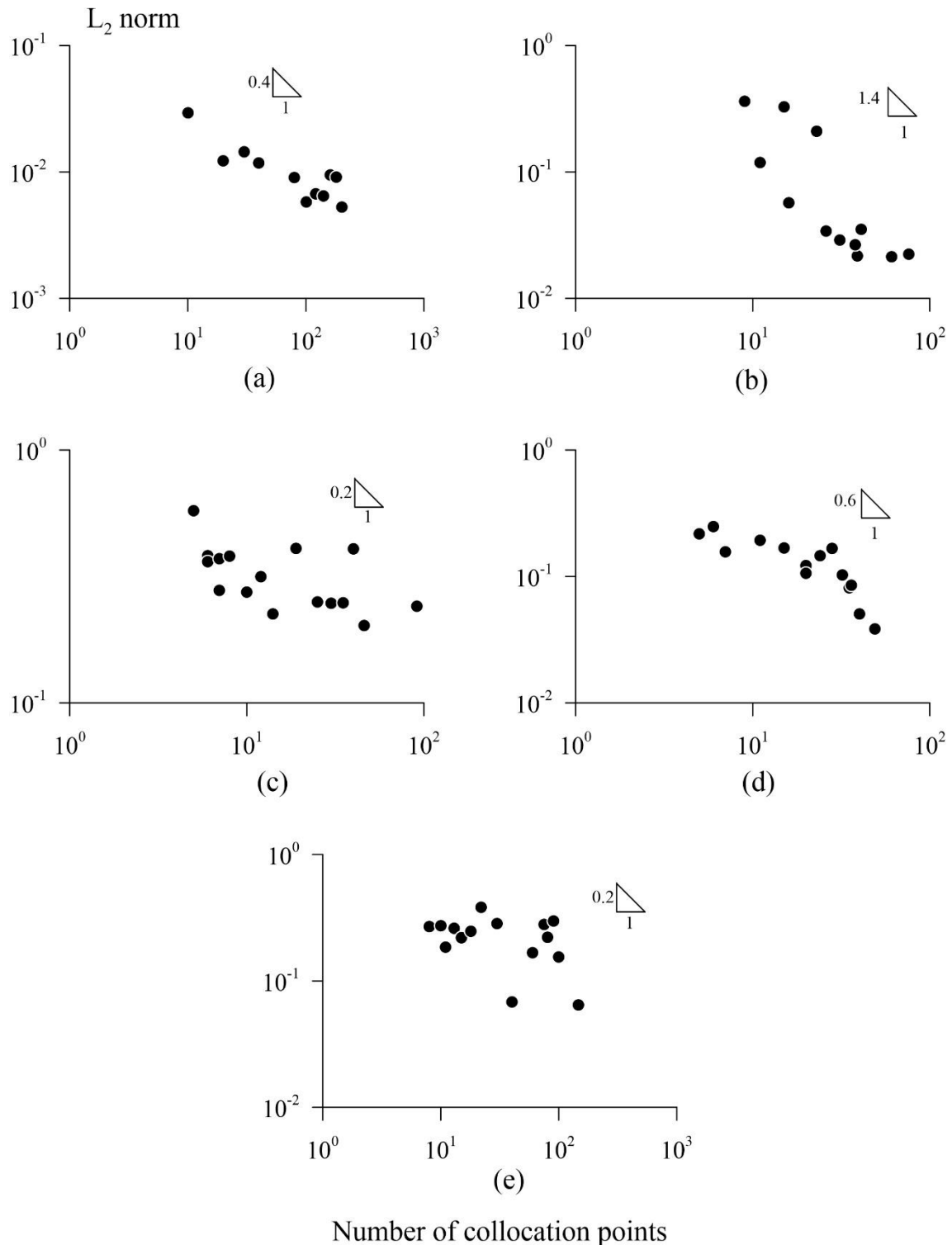


Figure 5.9: Rate of convergence. (a) Case 1, (b) Case 2, (c) Case 3, (d) Case 4, and (e) Case 5

5.3.4.2 Sensitivity test

Figure 5.10a-e presents the L_2 -norm when a “perturbation” of $\pm 10\%$ is introduced in the water depth at the boundary condition. The results depict that the addition of the perturbation has effects on the model fitting performance, but, more importantly, a different behavior is observed depending on the flow regime. In Case 4 (sudden water depth decrease), and Case 5 (Step-pool), there are performance oscillations when the boundary water depths are increased or decreased. In Case 1 (Subcritical flow), the performance stays constant until reaching 6% of water depth increase. When the boundary water depth increases more than 6%, the performance decreases

rapidly. However, there are performance oscillations when the boundary water depth decreases. In Case 2 the decrease of fitting performance when BC is decreased follows a pattern that seems parabolic, but this pattern is close to a line when the perturbation is positive. Case 3 (sudden increase of water depth) shows no sensitivity for negative variations in the water depth at the boundary; however a positive variation yields the highest performance variations.

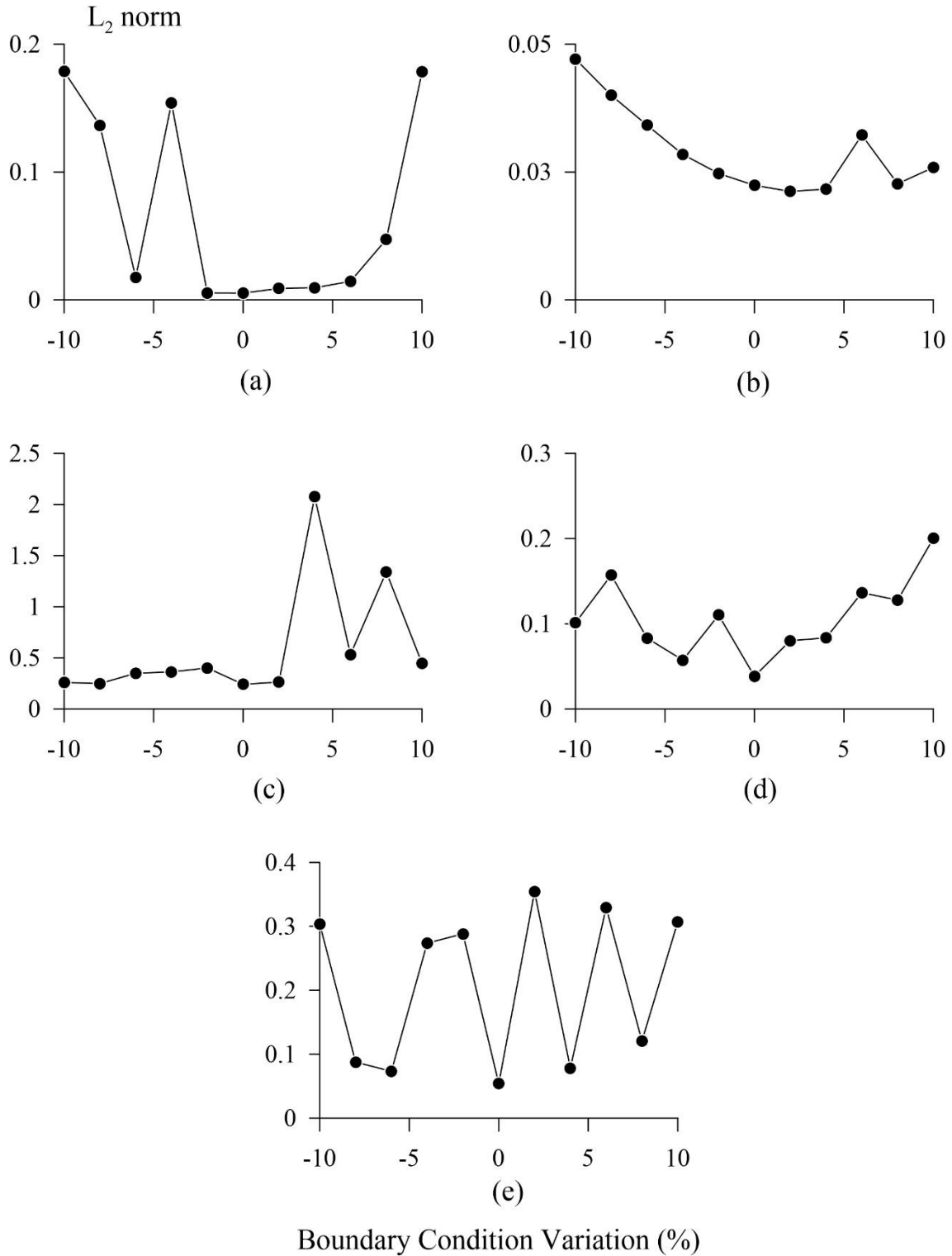


Figure 5.10: Sensibility test. (a) Case 1, (b) Case 2, (c) Case 3, (d) Case 4, and (e) Case 5

5.4 Discussion

5.4.1 Activation function performance

The selection of activation functions (AF) is important for the predictability of a neural network (Glorot & Bengio, 2010; Nwankpa et al., 2018), so its analysis is an important issue (Sharma et al., 2020). An AF introduces non-linearity into the network (Nwankpa et al., 2018). Hence, neural networks can learn complex relationships between input and output (Sibi et al., 2013). Moreover, selecting a convenient AF depends on the case under analysis, and there is no standard procedure (Sharma et al., 2020).

The current study found that the quality of the results strongly depends on the AF chosen. ReLU was the transfer function with the worst modelling predictions for forward as well as inverse problems. Nevertheless, this AF is the most widely used according to Ding et al. (2018) for typical machine learning applications. Sigmoid and Sin provide good results for GVF, but their performance is not good for RVF. For the inverse problem, both AF provide good results, except for mid flow where Tanh gives a resistance value closer to those of GLUE. Sigmoid cannot be recommended for RVF.

The performance of Sin is not surprise according to Goodfellow et al. (2016), who state that unpublished AF can have a similar performance to popular AF. Moreover, Hyperbolic Tangent (Tanh) is the transfer function with the best predictability for both forward and inverse problem. This AF has been widely adopted in PINN because it is infinitely differentiable, which is necessary to approximate the states of second or third-order partial differential equations governing different cases (Tartakovsky et al., 2020).

5.4.2 Neural network architecture

As in the case of the Activation Function, the number of layers and neurons per hidden layer plays an important role in a neural network performance (Guo et al., 2020; Sharma et al., 2020). As stated in Section 3.2 and 3.3, the analysis of the number of layers and neurons is based on Tanh results for forward problem and inverse problem.

Tartakovsky et al. (2020) explained that the number of layers and neurons depends on the smoothness of the output function. Moreover, the size of a neural network should be big enough to learn the mapping between inputs and outputs and small enough to be trained with the limited data available.

5.4.2.1 Forward problem: solving the differential equation

Case 1 and Case 3 (see Figures 5.6a and c) have the most complicated water depth profile of the benchmark cases. Case 1 water profile is characterized by two peaks with two inflection points, and Case 3 presents a discontinuity due to a hydraulic jump. Both Cases have the neural networks with the biggest size. Furthermore, Case 2 has the smoothest water depth profile of all the cases (see Figure 5.6b), having the second smallest neural network. The neural network dimensions of Cases 1, 2, and 3 agree with the information given above. Case 4 water depth profile (refer to Figure 5.6d) has a smooth solution, so it is not surprise the size of its neural network being the smallest.. Step-pool (Case 5), as expected, has a flow depth profile more complex than the benchmark cases due to the tumbling flow. The dimension of the neural network, when Tanh is used, is smaller than the previous most complex benchmark cases: Case 1 and Case 3.

The literature on PINN has shown that the number of hidden layers ranges from 7 to 9, while the number of neurons per hidden layer lies in the range of 20 to 120 neurons per hidden layer. The studied cases include the solution of forwarding problems using Burger's equation (Raissi et al., 2017b), the solution of the Euler equation for high-speed flows (Mao et al., 2020), the use of KdV-Burger's equation (Guo et al., 2020), and the fluid of blood in arteries applying a reduced form of Navier-Stokes equation (Kissas et al., 2020). Thus, the literature cases are representative of several phenomena in fluid flows. As mentioned in Section 3.2.2, the same pattern was obtained in this study, agreeing with the previously mentioned results except for Case 5. For Step-pool cases the resulting number of hidden layers is lower than the presented range, but the number of neurons per hidden layers is inside the range when Tanh is used. Nonetheless, if Sin or Sigmoid are used then the neural network dimension agrees with the found range of number of hidden layers and neurons per hidden layer.

5.4.2.2 Inverse problem

The available found literature for inverse problems is based on data from reference models or solvers: Raissi et al. (2017b) successfully found parameters of Burger's equation and Navier Stokes equations in continuous time models and, Mao et al. (2020) was able to find states of interest and parameters in high-speed aerodynamic flows.

In this study, real staff gauges measurements for three flow magnitudes (low, mid, and high flow (Cedillo et al., 2021b)) were used to obtain the resistance parameter.

The range of neural network architecture found in literature for inverse problem is highly variable: 3 to 9 hidden layers with 20 to 120 neurons per hidden layer (Mao et al., 2020; Raissi et al., 2017a). The architecture found in this research is inside the mentioned range. Furthermore, the number of hidden layers of the neural network varies depending on the flow magnitude while the number of neurons per hidden layer keeps constant. It has not been possible to find any reference with the application of PINN in Step-pool for inverse problem to compare the results. In that sense, this a first step in that direction.

5.4.3 PINN predictability

Case 1 and Case 2 show a GVF, meaning that the water depth never crosses the critical depth. Under these conditions the use of energy equation is allowed (Brunner, 2021). Case 1 and Case 2 has different flow types: Case 1 has subcritical flow, so there is low velocity and the flow is considered as tranquil. Case 2 has supercritical flow having high velocity and considered as rapid flow (Chow, 1959). Under subcritical flow, all AF have a good performance to predict water depth profile except for ReLU. On the other hand, the prediction of supercritical flow was performed efficiently by all the AF.

Case 3 and Case 4 represent RVF where the energy equation cannot be applied. According to Brunner (2021) in the case of rapidly varied flow, HEC-RAS uses the momentum equation for some instances such as hydraulic jump, low flow hydraulics at bridges, and stream junctions. In Case 4, PINN got a good answer when Tanh was used as an activation function, and the remaining activation functions got spurious discontinuities or non-physical answers. Indeed, PINN and HEC-RAS get the same answer because both solve the same equation. On the other hand, PINN was not able to predict the water depth profile in Case 3, producing a model with unsatisfactory performance. Even though HEC-RAS solves the momentum equation and PINN solves energy equation, PINN was able to predict the discontinuity in the water depth profile.

Case 5 represents a real system called Step-pool. For this system, besides having a complex profile, the cross sections are variable. Moreover, there is RVF at pools below the steps. Even through EF in Table 5.1 depicts a good fitting performance; Figures 5.7a, b, and c clearly shows small discrepancies in the water depth between PINN and HEC-RAS at some points, attributable to the different description of the cross-sectional geometry since in the proposed PINN all the cross sections geometry is contained in an equivalent cross section. In case of highly variable cross sections, it will be necessary to divide the reach into sub reaches each with a equivalent cross section and to implement continuity equations such as the ones used in Kissas et al. (2020).

Case 3 and 5 contain hydraulic jumps in the water depth profiles. Case 3 has a sudden decrease of the slope, and Case 5 has tumbling flow. Despite being a more complex case, Case 5 PINN prediction are much better than Case 3. There are some reasons why this may happen. These are, first, the difference between y_i and y_s in Case 3 is 1.56 m while in Case 5 the difference ranges from 0.24 to 0.39 cm. The hydraulic jump in Case 3 is four times bigger than those in Case 5. Second, the resistance value in Case 3 is ten times smaller than in Case 5. Thus, the resistance to flow in Case 5 is bigger than in Case 3 meaning a higher energy dissipation besides the one in the hydraulic jump. It seems possible that as hydraulic jump gets higher due to a low flow resistance, the prediction of PINN get worse.

5.4.4 Systematic studies

5.4.4.1 Rate of convergence

Case 2 (Supercritical flow) has the highest rate of convergence. A possible reason of the different pattern may be produced by the smoothness of the solution. Indeed, as can be seen in Figure 5.6b, the water depth in this Case do not have peaks, follow a descending pattern, and have small slopes. This may be the cause of the different convergence answers of PINN. Even though Case 4 has a sudden decrease of water depth (discontinuity), this case has a smooth solution. Thus, its high convergence rate is no surprise. Furthermore, the difference between both cases with discontinuities Case 4 and Case 3 (sudden increase of water depth) is the way in which HEC-RAS deals with the discontinuity. For a discontinuity like Case 3 HEC-RAS uses an alternative form of the momentum equation. However, for a Case 4 type of discontinuity HEC-RAS uses the same equation as ours: the equation of the energy (Eq. (5.1)).

The cases with a sudden increase in water depth (hydraulic jump) like Case 3 and Case 5 has the same rate of convergence 0.2. On the other hand, Case 1 (Subcritical flow) having a smooth solution with multiple peaks has a rate of convergence of 0.4. Thus, the effect of a discontinuity like a sudden increase of water depth affects the convergence by 50%.

5.4.4.2 Sensitivity test

Case 3 has the highest changes in the PINN model performance when boundary conditions are increased. The increasing of boundary depth could change the flow conditions in this case. Indeed, the boundary condition with supercritical flow could change to subcritical flow. In that case, there is no discontinuity (hydraulic jump), which explains the significant change in the performance of the method. On the other hand, the reduction of the value in the boundary condition might preserve the flow type, so the lack of sensitivity showed in Figure 5.10c is justified.

Case 2 has the slowest change in the model fitting performance. Case 2 profile has an increasing slope, so the flow is going to be supercritical. The supercritical profile is smooth so any change in the BC is not going to affect the water depth in an important way.

Case 1 fitting performance is affected only when the BC change reaches the highest values. When BC water depth is increased the subcritical flow is preserved. However, it seems that when the increase in the BC reaches a certain value the prediction quality decreases. The reduction in the boundary could lead to a change in the flow conditions, so the oscillation present in -4% in Figure 5.10a could be justified.

The oscillations in performance when BC water depths are increased or decreased are to be expected in the real case. This case has the most complex geometry and water depth pattern. Thus, any change at the BC could have different effect in the predicted water depth.

5.5 Conclusions

In this research, the predictive performance of the Physical Informed Neural Network (PINN) has been tested for a forward and an inverse problem. Moreover, PINN is a tool where the physics of a system is used. Four open channels cases with different bed shapes and prismatic cross-sections have been proposed to test the approximation ability of PINN under different flow types: subcritical, supercritical, and mixed for forward problem. Moreover, a fifth case based on a Step-pool in the Quinuas river was also included to solve a forward and an inverse problem with PINN. In addition, PINN results for the forward problem were compared to HEC-RAS, while the inverse problem results were compared with the results of a previous study based on the GLUE methodology.

This study has provided several interesting results for forward and inverse problems. For forward problems, PINN has shown good approximation characteristics, when a high number of collocation points are used. The predictability of Step-pool water depth profile was considered good; however a close look to the profiles shows a slight difference between PINN and HEC-RAS probably as a result of the simplified cross-sectional information.

The activation function (AF) played an important role in the approximation performance on forward problems. The hyperbolic tangent (Tanh) ended up being the activation function with the best performance for forward and inverse problem, when there are a sufficiently large number of collocation points. Furthermore, Sin and Sigmoid did not provide adequate results for rapid flow cases in the forward problem, but these AFs provide good results in the inverse problem. ReLU had the worst results in all the studied cases.

The rate of convergence was higher in cases with smooth solutions, and poorer in cases with a sudden increase of water depth. The introduction of a perturbation at the boundary condition has different effects depending on the flow type at each Case.

Chapter 6

6 Conclusions

The resistance factor has an important impact on the results of one-dimensional hydrodynamic models. Thus, the correct determination of that parameter is crucial for multiple applications where the model output will be used. Additionally, the resistance parameter estimated through field measurements is not always the same as the one used in a certain hydrodynamic model. Hence, in this thesis the focus was the different values that the resistance parameter could have for different applications. First, a so-called resistance factor field values were estimated through field measurements at different flow magnitudes and different morphologies of a mountain river. Then, different empirical equations to predict the resistance parameter were tested to find the best option for the mountain river study. Furthermore, knowing the vast options available in literature for resistance coefficients and their parameters, an alternative methodology was developed to improve the parameters of the best empirical equation found. Second, GLUE tests were employed to find an optimal resistance parameter range for the widely used one-dimensional HEC-RAS model. All the runs were executed under steady-state conditions. The found resistance parameter range was compared to the values found with field measurements. Third, the field values were used to construct “Physics-Informed Neural Network” (PINN) models to solve two kinds of models. The first ones to test the predictability of PINN models when using only boundary conditions as input data under different flow conditions. The second ones to test the PINN predictability of resistance values when compared to GLUE results. The research, therefore, has covered several important aspects of the resistance parameter and has proposed novel methodologies including the use of a recent development in deep learning which is PINN.

As explained, different topics were treated in different Chapters. In Chapter 3, all the field measurements required to estimate a physical resistance parameter are explained. There was a single type of equation which shows a better fitting performance, so a new methodology to estimate its parameters was proposed. Chapter 4 deals with GLUE test. Besides the resistance factor, the Representative Friction Slope Method was tested. Different conclusions with direct application to modelling were drawn. Chapter 5 depicts a first application of “Physics-Informed Neural Network” for mountain rivers. One of those experiments deals with the estimation of resistance parameter where the partial differential equation is the same as the one solved by HEC-RAS. In the following subsections, specific conclusions of the topics covered are presented.

6.1 Physical resistance parameter (PRP)

The field measurement campaign to estimate the Physical Resistance Parameter in mountain rivers is a challenge. The water depth measurement is much more than install flow gauges at calm zones. The presence of turbulence at high flows makes the level reading difficult being a source of uncertainty. The measurement of wetted width was also a challenge task. During low flow, the estimation of wetted width requires the measurement of the width of any exposed particle to be subtracted from the total width. Indeed; at some morphologies such as Step-pool or Cascade, the number of exposed particles becomes critical. The flow and mean velocity were the easiest variables to be measured because the corresponding sensor automatically register the water conductivity. However, the salt transportation was difficult due to high slopes. The measurement of bed material composition was one of the most tough tasks during this research. A pebble box was built specifically for this research. When big particles appear, a measuring tape was used instead. The mountain river cross-sections are highly variable so data from multiple cross-sections need to be taken to represent the whole reach. The field work at mountain rivers is complex and needs to be taken carefully to get valid results.

The estimation of the Physical Resistance Parameter was done in the Quinuas environment observatory. In this observatory there are three of the most common morphologies found in mountain rivers in just 1500 meters: three Cascades, two Step-pools, and one plane bed. Moreover, this research involved field measurements for different flow magnitudes. Thus, the analysis of different in-site and between-site resistance phenomena was possible. Different equations to predict resistance parameter as well as velocity has been tested and contrasted with the field data resulting Nondimensional hydraulic geometry equations the best performed predictive equation. Those equations relate a non-dimensional velocity (U^* or U^{**}) with a non-dimensional unitary flow parameter (q^* or q^{**}).

Furthermore, a new methodology to estimate parameters for Nondimensional hydraulic geometry equations was proposed. The methodology uses U^{**} and q^{**} because they were found through dimensional analysis in a publication. The developed new methodology requires at least three data of U^{**} and q^{**} to calibrate two parameters.

However, some findings in this research points toward that those parameters could be related to some characteristics of the reaches such as slope. Nevertheless, more field data is needed to go further and explore those relations. A research aiming to find a relation to those coefficients could extend the applicability of the proposed methodology to ungauged reaches.

6.2 Effective resistance coefficient (ERC)

The GLUE implementation allowed us to research the impact of two aspects of a HEC-RAS hydrodynamic model: The effect of the Representative Friction Slope Method and the resistance parameter range which best fits the available data.

The Representative Friction Slope Method is a parameter which acts during the solution of the energy equation in HEC-RAS. There were two experiments: The Representative Friction Slope Method was randomly selected in GLUE Experiment 1, while HEC-RAS automatically chose the Representative Friction Slope Method methodology in GLUE Experiment 2. The experiments taught us that an automatic selection of this parameter should be done only when the reach has a low slope, which is not most of the cases in mountain rivers. Moreover, the manual selection of the Representative Friction Slope Method has shown a limited effect.

The resistance parameters calibrated with GLUE were compared with those found through field measurements. Both values are similar for mid and high flows but differ at low flows. The difference pattern depends on the morphology and flow magnitude. Even though the comparison of both parameters were done under different morphologies and flow magnitudes (different resistance conditions), further analysis are required to extend the range of comparison between the effective parameters and the parameters determined with field data. More flow cases need to be tested to set up this comparison.

6.3 PINN application to mountain rivers

In this research, a methodology to use PINN for open channel with complex longitudinal profile and complex cross sections has been proposed and being tested with two experiment types: first; forward problems where some benchmark cases with different flow types and profiles were solved. A Step-pool case was also solved. Second, PINN model was used in inverse problem where a resistance parameter was found and compared to resistance parameters found in GLUE experiments.

The solution of PINN for forward problems was compared with the results of HEC-RAS model where PINN showed a great capability to predict the water level profile for benchmark cases as well as for a Step-pool cases despite tumbling flow. At Step-pool cases, a closer look to the water depth predictions showed slightly differences between PINN and HEC RAS model attributed to simplifications done in PINN architecture.

PINN and GLUE provide a promising similar resistance values for most flow magnitudes. At low flows, there are still differences between both predictions which is attributed to the simplifications of the transversal geometry. PINN have demonstrated a huge potential to model the typical flows of mountain rivers. Further improvements in the PINN model architecture will certainly increase its predictability; however, the physics of the flow will be always there to remind us the challenge hidden in turbulent flows.

6.4 Research limitations and further research

Even though the conclusions presented above are limited to one-dimensional flow under steady-state conditions, they are valuable and have important applications because one dimensional models are still widely used and require a small amount of data. Indeed, the PINN scheme proposed in this thesis could be extended to include additional phenomena and to make important predictions e.g. pollution transport. Furthermore, the expansion of this study to 2D or 3D will require an important field measurement effort, and where 2D or 3D flows are important.

The applicability of the previous obtained results in a big catchment such as Paute river depends on the chapter. First, the proposed methodology to predict velocity in Chapter 3 can be used at any mountain river reach. That methodology has been validated with data from literature consisted in a wide range of reaches. However, the comparisons of calibrated and measured based resistance parameter in Chapter 4 and the PINN methodology proposed in Chapter 5 has been develop for a certain mathematical description. In those chapters the flow is considered as one-dimensional steady state. Thus, additional research is needed to apply the proposed methodology in common cases such as main channel-flood plain interactions or curves.

References

- Abadi, M., Agarwal, A., Barham, P., Brevdo, E., Chen, Z., Citro, C., Corrado, G. S., Davis, A., Dean, J., Devin, M., Ghemawat, S., Goodfellow, I., Harp, A., Irving, G., Isard, M., Jia, Y., Jozefowicz, R., Kaiser, L., Kudlur, M., ... Zheng, X. (2016). TensorFlow: Large-Scale Machine Learning on Heterogeneous Distributed Systems. *ArXiv Preprint ArXiv:1603.04467*.
- Aberle, J., & Smart, G. M. (2003). The influence of roughness structure on flow resistance on steep slopes. *Journal of Hydraulic Research*, 41(3), 259–269. <https://doi.org/10.1080/00221680309499971>
- Aronica, G., Bates, P. D., & Horritt, M. S. (2002). Assessing the uncertainty in distributed model predictions using observed binary pattern information within GLUE. *Hydrological Processes*, 16(10), 2001–2016. <https://doi.org/10.1002/hyp.398>
- Aronica, G., Hankin, B., & Beven, K. (1998). Uncertainty and equifinality in calibrating distributed roughness coefficients in a flood propagation model with limited data. *Advances in Water Resources*, 22(4), 349–365. [https://doi.org/10.1016/S0309-1708\(98\)00017-7](https://doi.org/10.1016/S0309-1708(98)00017-7)
- Artichowicz, W., & Mikos-Studnicka, P. (2014). Comparison of average energy slope estimation formulas for one-dimensional steady gradually varied flow. *Archives of Hydro-Engineering and Environmental Mechanics*, 61(3–4), 89–109. <https://doi.org/10.1515/heem-2015-0006>
- Bathurst, J. C. (1985). Flow Resistance Estimation in Mountain Rivers. *Journal of Hydraulic Engineering*, 111(4), 625–643. [https://doi.org/10.1061/\(ASCE\)0733-9429\(1985\)111:4\(625\)](https://doi.org/10.1061/(ASCE)0733-9429(1985)111:4(625))
- Bathurst, J. C. (1986). Slope-area Discharge Gaging in Mountain Rivers. *Journal of Hydraulic Engineering*, 112(5), 376–391. [https://doi.org/10.1061/\(ASCE\)0733-9429\(1986\)112:5\(376\)](https://doi.org/10.1061/(ASCE)0733-9429(1986)112:5(376))
- Bathurst, J. C. (2002). At-a-site variation and minimum flow resistance for mountain rivers. *Journal of Hydrology*, 269(1–2), 11–26. [https://doi.org/10.1016/S0022-1694\(02\)00191-9](https://doi.org/10.1016/S0022-1694(02)00191-9)
- Berger, R. C., & Stockstill, R. L. (1995). Finite-element model for high-velocity channels. *Journal of Hydraulic Engineering*, 121(10), 710–716.
- Beven, K., & Binley, A. (1992). The future of distributed models: Model calibration and uncertainty prediction. *Hydrological Processes*, 6(3), 279–298. <https://doi.org/10.1002/hyp.3360060305>
- Beven, K., & Binley, A. (2014). GLUE: 20 years on. *Hydrological Processes*, 28(24), 5897–5918. <https://doi.org/10.1002/hyp.10082>
- Bhola, P. K., Leandro, J., & Disse, M. (2019). Reducing uncertainties in flood inundation outputs of a two-dimensional hydrodynamic model by constraining roughness. *Natural Hazards and Earth System Sciences*, 19(7), 1445–1457. <https://doi.org/10.5194/nhess-2018-369>
- Blasone, R. S., Vrugt, J. A., Madsen, H., Rosbjerg, D., Robinson, B. A., & Zyvoloski, G. A. (2008). Generalized likelihood uncertainty estimation (GLUE) using adaptive Markov Chain Monte Carlo sampling. *Advances in Water Resources*, 31(4), 630–648. <https://doi.org/10.1016/j.advwatres.2007.12.003>
- Bozzi, S., Passoni, G., Bernardara, P., Goutal, N., & Arnaud, A. (2015). Roughness and Discharge Uncertainty in 1D Water Level Calculations. *Environmental Modeling and Assessment*, 20(4), 343–353. <https://doi.org/10.1007/s10666-014-9430-6>
- Brunner, G. (2021). *HEC RAS, River Analysis System Hydraulic Reference Manual*.
- Bunte, K., & Abt, S. R. (2001). *Sampling surface and subsurface particle-size distributions in wadable gravel- and cobble-bed streams for analyses in sediment transport, hydraulics, and streambed monitoring*. US Department of Agriculture, Forest Service, Rocky Mountain Research Station. <https://doi.org/10.1017/CBO9781107415324.004>

- Camp, J., Whyte, D., & Shaw, A. (2016). *Vulnerabilities Due to Flooding Events*. <https://rosap.nrl.bts.gov/view/dot/32095>
- Cedillo, S., Sánchez-Cordero, E., Timbe, L., Samaniego, E., & Alvarado, A. (2021a). Resistance Analysis of Morphologies in Headwater Mountain Streams. *Water*, *13*(16), 2207. <https://doi.org/10.3390/w13162207>
- Cedillo, S., Sánchez-Cordero, E., Timbe, L., Samaniego, E., & Alvarado, A. (2021b). Patterns of Difference between Physical and 1-D Calibrated Effective Roughness Parameters in Mountain Rivers. *Water*, *13*(22), 3202. <https://doi.org/10.3390/W13223202>
- Chai, T., & Draxler, R. R. (2014). Root mean square error (RMSE) or mean absolute error (MAE)? -Arguments against avoiding RMSE in the literature. *Geoscientific Model Development*, *7*(3), 1247–1250. <https://doi.org/10.5194/gmd-7-1247-2014>
- Chapra, S. C. (2008). *Surface water-quality modeling* (2008th ed.). Waveland Press Inc.
- Chin, A., & Wohl, E. (2005). Toward a theory for step pools in stream channels. *Progress in Physical Geography*, *29*(3), 275–296. <https://doi.org/10.1191/0309133305pp449ra>
- Chow, V. T. (1959). Open-Channel Hydraulics. In *Science*. McGraw-Hill civil engineering series.
- Comiti, F., Cadol, D., & Wohl, E. (2009). Flow regimes, bed morphology, and flow resistance in self-formed step-pool channels. *Water Resources Research*, *45*(4), 1–18. <https://doi.org/10.1029/2008WR007259>
- Comiti, F., Mao, L., Wilcox, A., Wohl, E. E., & Lenzi, M. A. (2007). Field-derived relationships for flow velocity and resistance in high-gradient streams. *Journal of Hydrology*, *340*(1–2), 48–62. <https://doi.org/10.1016/J.JHYDROL.2007.03.021>
- Cook, A., & Merwade, V. (2009). Effect of topographic data, geometric configuration and modeling approach on flood inundation mapping. *Journal of Hydrology*, *377*(1–2), 131–142. <https://doi.org/10.1016/J.JHYDROL.2009.08.015>
- Cuomo, S., di Cola, V. S., Giampaolo, F., Rozza, G., Raissi, M., & Piccialli, F. (2022). *Scientific Machine Learning through Physics-Informed Neural Networks: Where we are and What's next*. <https://doi.org/10.48550/arxiv.2201.05624>
- Curran, J. H., & Wohl, E. E. (2003). Large woody debris and flow resistance in step-pool channels, Cascade Range, Washington. *Geomorphology*, *51*(1–3), 141–157. [https://doi.org/10.1016/S0169-555X\(02\)00333-1](https://doi.org/10.1016/S0169-555X(02)00333-1)
- David, G. C. L., Wohl, E., Yochum, S. E., & Bledsoe, B. P. (2010). Controls on spatial variations in flow resistance along steep mountain streams. *Water Resources Research*, *46*(3). <https://doi.org/10.1029/2009WR008134>
- Ding, B., Qian, H., & Zhou, J. (2018). Activation functions and their characteristics in deep neural networks. *2018 Chinese Control and Decision Conference (CCDC)*, 1836–1841. <https://doi.org/10.1109/CCDC.2018.8407425>
- Dodge, Y. (2008). The Concise Encyclopedia of Statistics. In *The Concise Encyclopedia of Statistics*. Springer Science & Business Media. <https://doi.org/10.1007/978-0-387-32833-1>
- Douben, K. J. (2006). Characteristics of river floods and flooding: A global overview, 1985-2003. *Irrigation and Drainage*, *55*(SUPPL. 1), 25–27. <https://doi.org/10.1002/ird.239>
- Ferguson, R. (2007). Flow resistance equations for gravel- and boulder-bed streams. *Water Resources Research*, *43*(5). <https://doi.org/10.1029/2006WR005422>
- Ferro, V., & Giordano, G. (1991). Experimental Study of Flow Resistance in Gravel-Bed Rivers. *Journal of Hydraulic Engineering*, *117*(10), 1239–1246. [https://doi.org/10.1061/\(ASCE\)0733-9429\(1991\)117:10\(1239\)](https://doi.org/10.1061/(ASCE)0733-9429(1991)117:10(1239))
- Fish, J., & Belytschko, T. (2007). A First Course in Finite Elements. In *A First Course in Finite Elements*. <https://doi.org/10.1002/9780470510858>
- Fornasini, Paolo. (2008). *The uncertainty in physical measurements : an introduction to data analysis in the physics laboratory*. Springer.

- Glorot, X., & Bengio, Y. (2010). Understanding the difficulty of training deep feedforward neural networks. *Journal of Machine Learning Research*, 9(May), 249–256.
- Goodell, C. (2014). *Breaking the HEC-RAS Code: A User's Guide to Automating HEC-RAS*. h2ls.
- Goodfellow, I., Bengio, Y., & Courville, A. (2016). *Deep Learning*. MIT Press.
- Graf, W. H., & Qu, Z. (2004). Flood hydrographs in open channels. *Proceedings of the Institution of Civil Engineers - Water Management*, 157(1), 45–52. <https://doi.org/10.1680/wama.2004.157.1.45>
- Güneş Baydin, A., Pearlmutter, B. A., Andreyevich Radul, A., & Mark Siskind, J. (2018). Automatic differentiation in machine learning: A survey. *Journal of Machine Learning Research*, 18, 1–43.
- Guo, Y., Cao, X., Liu, B., & Gao, M. (2020). Solving partial differential equations using deep learning and physical constraintsts. *Applied Sciences*, 10(17), 5917. <https://doi.org/10.3390/app10175917>
- He, Q., & Tartakovsky, A. M. (2021). Physics-Informed Neural Network Method for Forward and Backward Advection-Dispersion Equations. *Water Resources Research*, 57(7), e2020WR029479.
- Horritt, M. S., & Bates, P. D. (2002). Evaluation of 1D and 2D numerical models for predicting river flood inundation. *Journal of Hydrology*, 268(1–4), 87–99. [https://doi.org/10.1016/S0022-1694\(02\)00121-X](https://doi.org/10.1016/S0022-1694(02)00121-X)
- Hudson, R., & Fraser, J. (2005a). Introduction to salt dilution gauging for streamflow measurement, Part IV: The mass balance (or dry injection) method. *Streamline Watershed Management Bulletin*, 9(1), 6–12.
- Hudson, R., & Fraser, J. (2005b). *The Mass Balance (or Dry Injection) Method*. 9(1), 6–12.
- Jacquemin, T., & Bordas, S. P. A. (2021). A unified algorithm for the selection of collocation stencils for convex, concave, and singular problems. *International Journal for Numerical Methods in Engineering*, 122(16). <https://doi.org/10.1002/nme.6703>
- Jarrett, R. D. (1984). Hydraulics of high-gradient streams. *Journal of Hydraulic Engineering*, 110(11), 1519–1539. [https://doi.org/https://doi.org/10.1061/\(ASCE\)0733-9429\(1984\)110:11\(1519\)](https://doi.org/https://doi.org/10.1061/(ASCE)0733-9429(1984)110:11(1519))
- Jarrett, R. D. (1985). *Determination of roughness coefficients for streams in Colorado*.
- Jung, Y., & Merwade, V. (2012). Uncertainty quantification in flood inundation mapping using generalized likelihood uncertainty estimate and sensitivity analysis. *Journal of Hydrologic Engineering*, 17(4), 507–520. [https://doi.org/10.1061/\(ASCE\)HE.1943-5584.0000476](https://doi.org/10.1061/(ASCE)HE.1943-5584.0000476)
- Kissas, G., Yang, Y., Hwuang, E., Witschey, W. R., Detre, J. A., & Perdikaris, P. (2020). Machine learning in cardiovascular flows modeling: Predicting arterial blood pressure from non-invasive 4D flow MRI data using physics-informed neural networks. *Computer Methods in Applied Mechanics and Engineering*, 358, 112623. <https://doi.org/10.1016/j.cma.2019.112623>
- Knight, D. W. (1981). Some field measurements concerned with the behaviour of resistance coefficients in a tidal channel. *Estuarine, Coastal and Shelf Science*, 12(3), 303–322. [https://doi.org/10.1016/S0302-3524\(81\)80127-2](https://doi.org/10.1016/S0302-3524(81)80127-2)
- Knight, D. W., McGahey, C., Lamb, R., & Samuels, P. (2009). *Practical channel hydraulics: Roughness, conveyance and afflux*. CRC Press.
- Laurenson, E. M. (1986). Friction Slope Averaging in Backwater Calculations. *Journal of Hydraulic Engineering*, 112(12), 1151–1163. [https://doi.org/10.1061/\(ASCE\)0733-9429\(1986\)112:12\(1151\)](https://doi.org/10.1061/(ASCE)0733-9429(1986)112:12(1151))
- Lee, A. J., & Ferguson, R. I. (2002). Velocity and flow resistance in step-pool streams. *Geomorphology*, 46(1–2), 59–71. [https://doi.org/10.1016/S0169-555X\(02\)00054-5](https://doi.org/10.1016/S0169-555X(02)00054-5)
- Lovric, M. (2011). International Encyclopedia of Statistical Science. In L. Miodrag (Ed.), *International Encyclopedia of Statistical Science*. Springer. <https://doi.org/10.1007/978-3-642-04898-2>
- MacFarlane, W. A., & Wohl, E. (2003). Influence of step composition on step geometry and flow resistance in step-pool streams of the Washington Cascades. *Water Resources Research*, 39(2). <https://doi.org/10.1029/2001WR001238>

- Mao, Z., Jagtap, A. D., & Karniadakis, G. E. (2020a). Physics-informed neural networks for high-speed flows. *Computer Methods in Applied Mechanics and Engineering*, 360, 112789. <https://doi.org/10.1016/j.cma.2019.112789>
- Mao, Z., Jagtap, A. D., & Karniadakis, G. E. (2020b). Physics-informed neural networks for high-speed flows. *Computer Methods in Applied Mechanics and Engineering*. <https://doi.org/10.1016/j.cma.2019.112789>
- Marcus, W. A., Roberts, K., Harvey, L., & Tackman, G. (1992). An Evaluation of Methods for Estimating Manning's n in Small Mountain Streams. *Mountain Research and Development*, 12(3), 227–239. <https://doi.org/10.2307/3673667>
- Marriott, M., Featherstone, R. E., & Nalluri, C. (2016). *Nalluri And Featherstone's Civil Engineering Hydraulics: Essential Theory with Worked Examples*. John Wiley & Sons.
- Maxwell, A. R., & Papanicolaou, A. N. (2001). Step-pool morphology in high-gradient streams. *International Journal of Sediment Research*, 16(3), 380–390.
- McCuen, R. H., Knight, Z., & Cutter, A. G. (2006). Evaluation of the Nash–Sutcliffe Efficiency Index. *Journal of Hydrologic Engineering*, 11(6), 597–602. [https://doi.org/10.1061/\(ASCE\)1084-0699\(2006\)11:6\(597\)](https://doi.org/10.1061/(ASCE)1084-0699(2006)11:6(597))
- Merz, R., & Blöschl, G. (2004). Regionalisation of catchment model parameters. *Journal of Hydrology*, 287(1–4), 95–123. <https://doi.org/10.1016/j.jhydrol.2003.09.028>
- Montgomery, D. R., & Buffington, J. M. (1997). Channel-reach morphology in mountain drainage basins. *Geological Society of America Bulletin*, 109(5), 596–611. [https://doi.org/https://doi.org/10.1130/0016-7606\(1997\)109<0596:CRMIMD>2.3.CO;2](https://doi.org/https://doi.org/10.1130/0016-7606(1997)109<0596:CRMIMD>2.3.CO;2)
- Moore, R. D. D. (2005). Slug injection using salt in solution. *Streamline Watershed Management Bulletin*, 8(2), 1–6.
- Morvan, H., Knight, D., Wright, N., Tang, X., & Crossley, A. (2008). The concept of roughness in fluvial hydraulics and its formulation in 1D, 2D and 3D numerical simulation models. *Journal of Hydraulic Research*, 46(2), 191–208. <https://doi.org/10.1080/00221686.2008.9521855>
- Mrokowska, M. M., Rowi, P. M., & Kalinowska, M. B. (2015). A methodological approach of estimating resistance to flow under unsteady flow conditions. *Hydrol. Earth Syst. Sci*, 19, 4041–4053. <https://doi.org/10.5194/hess-19-4041-2015>
- Mrokowska, M. M., Rowiński, P. M., & Kalinowska, M. B. (2015). Evaluation of friction velocity in unsteady flow experiments. *Journal of Hydraulic Research*, 53(5), 659–669. <https://doi.org/10.1080/00221686.2015.1072853>
- Nayak, P. C., Venkatesh, B., Krishna, B., & Jain, S. K. (2013). Rainfall-runoff modeling using conceptual, data driven, and wavelet based computing approach. *Journal of Hydrology*, 493, 57–67. <https://doi.org/10.1016/j.jhydrol.2013.04.016>
- Nitsche, M., Rickenmann, D., Kirchner, J. W., Turowski, J. M., & Badoux, A. (2012). Macroroughness and variations in reach-averaged flow resistance in steep mountain streams. *Water Resources Research*, 48(12). <https://doi.org/10.1029/2012WR012091>
- Nwankpa, C., Ijomah, W., Gachagan, A., & Marshall, S. (2018). Activation Functions: Comparison of trends in Practice and Research for Deep Learning. *ArXiv Preprint ArXiv:1811.03378*.
- Pagliara, S., & Chiavaccini, P. (2006). Flow Resistance of Rock Chutes with Protruding Boulders. *Journal of Hydraulic Engineering*, 132(6), 545–552. [https://doi.org/10.1061/\(ASCE\)0733-9429\(2006\)132:6\(545\)](https://doi.org/10.1061/(ASCE)0733-9429(2006)132:6(545))
- Pagliara, S., Das, R., & Carnacina, I. (2008). Flow resistance in large-scale roughness condition. *Canadian Journal of Civil Engineering*, 35(11), 1285–1293.
- Papaioannou, G., Vasiliades, L., Loukas, A., & Aronica, G. T. (2017). Probabilistic flood inundation mapping at ungauged streams due to roughness coefficient uncertainty in hydraulic modelling. *Advances in Geosciences*, 44, 23–34. <https://doi.org/10.5194/adgeo-44-23-2017>

- Papanicolaou, A. N., Bdour, A., & Wicklein, E. (2004). One-dimensional hydrodynamic/sediment transport model applicable to steep mountain streams. *Journal of Hydraulic Research*, 42(4), 357–375. <https://doi.org/10.1080/00221686.2004.9641204>
- Pappenberger, F., Beven, K., Horritt, M., & Blazkova, S. (2005). Uncertainty in the calibration of effective roughness parameters in HEC-RAS using inundation and downstream level observations. *Journal of Hydrology*, 302(1–4), 46–69. <https://doi.org/10.1016/J.JHYDROL.2004.06.036>
- Parker, G., Toro-Escobar, C. M., Ramey, M., & Beck, S. (2003). Effect of Floodwater Extraction on Mountain Stream Morphology. *Journal of Hydraulic Engineering*, 129(11), 885–895. [https://doi.org/10.1061/\(asce\)0733-9429\(2003\)129:11\(885\)](https://doi.org/10.1061/(asce)0733-9429(2003)129:11(885))
- Parker, G., Wilcock, P. R., Paola, C., Dietrich, W. E., & Pitlick, J. (2007). Physical basis for quasi-universal relations describing bankfull hydraulic geometry of single-thread gravel bed rivers. *Journal of Geophysical Research: Earth Surface*, 112(F4). <https://doi.org/10.1029/2006JF000549>
- Raissi, M., Perdikaris, P., & Karniadakis, G. E. (2017a). Physics informed deep learning (Part ii): Data-driven discovery of nonlinear partial differential equations. *ArXiv Preprint ArXiv:1711.10566v1*.
- Raissi, M., Perdikaris, P., & Karniadakis, G. E. (2017b). Physics informed deep learning (part i): Data-driven solutions of nonlinear partial differential equations. *ArXiv Preprint ArXiv:1711.10561*. <http://arxiv.org/abs/1711.10561>
- Raissi, M., Perdikaris, P., & Karniadakis, G. E. (2018). Multistep neural networks for data-driven discovery of nonlinear dynamical systems. *ArXiv Preprint ArXiv:1801.01236*.
- Raissi, M., Yazdani, A., & Karniadakis, G. E. (2018). *Hidden Fluid Mechanics: A Navier-Stokes Informed Deep Learning Framework for Assimilating Flow Visualization Data*.
- Rao, C., Sun, H., & Liu, Y. (2020). Physics-informed deep learning for incompressible laminar flows. *Theoretical and Applied Mechanics Letters*, 10(3), 207–212. <https://doi.org/10.1016/j.taml.2020.01.039>
- Rickenmann, D., & Recking, A. (2011). Evaluation of flow resistance in gravel-bed rivers through a large field data set. *Water Resources Research*, 47(7). <https://doi.org/10.1029/2010WR009793>
- Ritter, A., & Muñoz-Carpena, R. (2013). Performance evaluation of hydrological models: Statistical significance for reducing subjectivity in goodness-of-fit assessments. *Journal of Hydrology*, 480, 33–45. <https://doi.org/10.1016/j.jhydrol.2012.12.004>
- Romero, M., Revollo, N., & Molina, J. (2010). Flow resistance in steep mountain rivers in Bolivia. *Journal of Hydrodynamics*, 22(5 SUPPL. 1), 679–684. [https://doi.org/10.1016/S1001-6058\(10\)60018-2](https://doi.org/10.1016/S1001-6058(10)60018-2)
- Sart, C., Baume, J.-P., Malaterre, P.-O., & Guinot, V. (2010). Adaptation of Preissmann's scheme for transcritical open channel flows. *Journal of Hydraulic Research*, 48(4), 428–440. <https://doi.org/10.1080/00221686.2010.491648>
- Sellin, R. H. J., & van Beesten, D. P. (2004). Conveyance of a managed vegetated two-stage river channel. *Proceedings of the Institution of Civil Engineers - Water Management*, 157(1), 21–33. <https://doi.org/10.1680/wama.2004.157.1.21>
- Sharma, S., Sharma, S., & Athaiya, A. (2020). Activation functions in neural networks. *International Journal of Engineering Applied Sciences and Technology*, 04(12), 310–316. <https://doi.org/10.33564/ijeast.2020.v04i12.054>
- Sibi, P., Allwyn Jones, S., & Siddarth, P. (2013). Analysis of different activation functions using back propagation neural networks. *Journal of Theoretical and Applied Information Technology*, 47(3), 1264–1268.
- Tartakovsky, A. M., Marrero, C. O., Perdikaris, P., Tartakovsky, G. D., & Barajas-Solano, D. (2020). Physics-informed deep neural networks for learning parameters and constitutive relationships in subsurface flow problems. *Water Resources Research*, 56(5), e2019WR026731. <https://doi.org/10.1029/2019WR026731>
- Teng, J., Jakeman, A. J., Vaze, J., Croke, B. F. W., Dutta, D., & Kim, S. (2017). Flood inundation modelling: A review of methods, recent advances and uncertainty analysis. *Environmental Modelling and Software*, 90, 201–216. <https://doi.org/10.1016/j.envsoft.2017.01.006>

- Waldon, M. G. (2004). Estimation of Average Stream Velocity. *Journal of Hydraulic Engineering*, 130(11), 1119–1122. [https://doi.org/10.1061/\(ASCE\)0733-9429\(2004\)130:11\(1119\)](https://doi.org/10.1061/(ASCE)0733-9429(2004)130:11(1119))
- Wang, R., Kashinath, K., Mustafa, M., Albert, A., & Yu, R. (2020). Towards physics-informed deep learning for turbulent flow prediction. *Proceedings of the 26th ACM SIGKDD International Conference on Knowledge Discovery & Data Mining*, 1457–1466. <https://doi.org/10.1145/3394486.3403198>
- Wilcox, A. C., Nelson, J. M., & Wohl, E. E. (2006). Flow resistance dynamics in step-pool channels: 2. Partitioning between grain, spill, and woody debris resistance. *Water Resources Research*, 42(5). <https://doi.org/10.1029/2005WR004278>
- Wilcox, A. C., & Wohl, E. E. (2006). Flow resistance dynamics in step-pool stream channels: 1. Large woody debris and controls on total resistance. *Water Resources Research*, 42(5). <https://doi.org/10.1029/2005WR004277>
- Willmott, C. J., & Matsuura, K. (2005). Advantages of the mean absolute error (MAE) over the root mean square error (RMSE) in assessing average model performance. *Climate Research*, 30(1), 79–82. <https://doi.org/10.3354/cr030079>
- Wohl, E. (1998). Uncertainty in flood estimates associated with roughness coefficient. *Journal of Hydraulic Engineering*, 124(2), 219–223. [https://doi.org/10.1061/\(ASCE\)0733-9429\(1998\)124:2\(219\)](https://doi.org/10.1061/(ASCE)0733-9429(1998)124:2(219))
- Wohl, E. (2000). *Mountain Rivers* (Vol. 14). American Geophysical Union. <https://doi.org/10.1029/WM014>
- Wohl, E. (2013). Mountain Rivers Revisited. In *Mountain Rivers Revisited*. American Geophysical Union. <https://doi.org/10.1029/WM019>
- Wolman, M. G. (1954). A method of sampling coarse river-bed material. *EOS, Transactions American Geophysical Union*, 35(6), 951–956.
- Yochum, S., & Bledsoe, B. (2010). Flow resistance estimation in high-gradient streams. *4th Federal Interagency Hydrologic Modeling Conference*. https://acwi.gov/sos/pubs/2ndJFIC/Contents/5E_Yochum_01_04_10_2_.pdf
- Yochum, S. E. (2010). *Flow resistance prediction in high-gradient streams* [Doctoral dissertation, Colorado State University]. <https://search.proquest.com/openview/64634e98be340e633e1358aecb735b41/1?pq-origsite=gscholar&cbl=18750&diss=y>
- Yochum, S. E., Comiti, F., Wohl, E., David, G. C. L., & Mao, L. (2014). Photographic guidance for selecting flow resistance coefficients in high-gradient channels. In *Gen. Tech. Rep. RMRS-GTR-323*. Fort Collins, CO: U.S. Department of Agriculture, Forest Service, Rocky Mountain Research Station. 91 p. (Vol. 323). <https://doi.org/10.2737/RMRS-GTR-323>
- Zimmermann, A. (2010). Flow resistance in steep streams: An experimental study. *Water Resources Research*, 46(9). <https://doi.org/10.1029/2009WR007913>

Curriculum vitae

PERSONAL DETAILS

Name: Juan Sebastián Cedillo Galarza

Age: 34

Address: Marco Tulio Erazo y Manuel Espinoza, Cuenca, Ecuador

Telephone Number: 0987397162

Email: sebastiancedillo@gmail.com

EDUCATION

2011: Civil Engineer

2016: Master of Science in Civil Engineering with specialization in water management

EXPERIENCE

2016: Estudiante Doctoral- Departamento de Recursos Hídricos y Ciencias Ambientales.

2016-2017: Asistente de ingeniería hidráulica- Estudios de vulnerabilidad a eventos de crecida y diseño de obras físicas para protección de márgenes e infraestructuras existentes de los aprovechamientos Alazan y San Antonio" proceso LCC-CELHAZ-015-16 y su contrato complementario HAZ-CON-007-17.

2013-2014: Asistente de investigación- Departamento de Recursos Hídricos y Ciencias Ambientales.

2011-2012: Asistente de investigación- Grupo de las ciencias de la tierra y el ambiente.

CONGRESS

World Environmental and Water Resources Congress 2021: Calibration of effective resistance parameters for Andean mountain river morphologies using 1D hydraulic models.

VII International Conference on Science, Technology and Innovation for Society CITIS 2021, Exploratory study of physic informed deep learning applied to a step-pool for different flow magnitudes

Segundo Congreso Nacional de Geografía del Ecuador: Variabilidad temporal y espacial del coeficiente de rugosidad en un río de cabecera: Caso río Quinuas

2021 IEEE Fifth Ecuador Technical Chapters Meeting (ETCM): Differences between effective and physical resistance parameter- A headwater mountain river experiment

CONGRESS ARTICLES

Cedillo, S.; Timbe, L.; Sanchez-Cordero, E.; Samaniego, E.; Narea, K.; Alvarado, A. Differences Between Effective and Physical Resistance Parameter- A Headwater Mountain River Experiment. 2021 IEEE Fifth Ecuador Tech. Chapters Meet. 2021, 1–4, doi:10.1109/ETCM53643.2021.9590636.

Cedillo, S.; Sánchez-Cordero, E.; Samaniego, E.; Alvarado, A. Exploratory Study of Physic Informed Deep Learning Applied to a Step-Pool for Different Flow Magnitudes. Smart Innov. Syst. Technol. 2021, 252, 275–284, doi:10.1007/978-981-16-4126-8_26.

Cedillo, S.; Timbe, L.; Samaniego, E.; Alvarado, A. Resistance Partitioning of Headwater Mountain Streams A Case Study in Southern Ecuador. In Proceedings of the World Environmental and Water Resources Congress 2020: Hydraulics, Waterways, and Water Distribution Systems Analysis - Selected Papers from the Proceedings of the World Environmental and Water Resources Congress 2020; 2020.

Lepot, Mathieu; Hernandez, Benjamin; Cedillo, Sebastian; Goes, Bart; Schellart, Alma; Verlinden, Jouke ; Clemens, F.H.L.R. Use of numbered and coloured 3d printed pills as a new, low-cost, robust and easy method to inspect mis-, cross- and illicit connections in separate sewers. NOVATECH 2016.

Cedillo, Sebastian; Lepot, Mathieu; Fischer, Stéphane; Clemens, F.H.L.R. 3D interpolation in a velocity field in sewers. 10th Int. Symp. Ultrason. Doppler Methods Fluid Mech. Fluid Eng. 2016.

Cedillo, Sebastian; Lepot, Mathieu; Clemens, F.H.L.R. Potentiality of a velocity profiler to investigate sewers: results of laboratory experiments. 8 th Int. Conf. Sewer Process. Networks 2016.

Lepot, Mathieu; Hernandez, Benjamin; Cedillo, Sebastian; Goes, Bart; Schellart, Alma; Verlinden, Jouke ; Clemens, F.H.L.R. 3d printed pills to investigate mis-connections. 8 th Int. Conf. Sewer Process. Networks 2016.

ARTICLES IN INDEXED JOURNALS

Cedillo Galarza, J.S.; Timbre Castro, L.M.; Samaniego Alvarado, E.P.; Alvarado Martínez, A.O. Efecto del refinamiento de la descripción de la rugosidad en una aproximación 2D para un río de montaña: un caso de estudio. *La Granja* 2021, 33, 92–102, doi:10.17163/lgr.n33.2021.08.

Cedillo, S.; Sánchez-Cordero, E.; Timbe, L.; Samaniego, E.; Alvarado, A. Patterns of Difference between Physical and 1-D Calibrated Effective Resistance Parameters in Mountain Rivers. *Water* 2021, 13, 3202, doi:10.3390/W13223202.

Cedillo, S.; Sánchez-Cordero, E.; Timbe, L.; Samaniego, E.; Alvarado, A. Resistance Analysis of Morphologies in Headwater Mountain Streams. *Water* 2021, 13, 2207, doi:10.3390/w13162207.

Cedillo, S., Núñez, A.-G., Sánchez-Cordero, E., Timbe, L., Samaniego E., Alvarado A. (2022) Physics-Informed Neural Network water surface predictability for 1D steady-state open channel cases with different flow types and complex bed profile shapes. *Advanced Modeling and Simulation in Engineering Sciences*. [Online] 9 (1), 10. Available from: doi:10.1186/S40323-022-00226-8 [Accessed: 30 June 2022].

Symbology and abbreviations

A: Cross sectional area [L^2]

AD: Automatic Differentiation

A_{lob}, A_{mc}, and A_{rob}: Flow areas at the left overbank, main channel, and right overbank (L^2)

A_t: Total flow area (m^2)

a,b,c,d1,e: Parameters [-]

ΔB_i : Width discretization [L]

C: Chezy resistance coefficient []

C_t: Concentration at time t [ML^{-3}]

C(x,t): Concentration at certain time and space [ML^{-3}]

d: Mean water depth [L]

d_{step}: Height of a step-pool bed form [L]

d_i: Depth at $n \cdot \Delta B_i$ [L]

D_{xx}: Characteristic bed material diameter [L]

EC_t: Total conductivity [$L^{-1}M^{-2}T^{-3}I^{-1}$]

EF: Nash–Sutcliffe efficiency index

ERC: Effective Resistance Coefficient

ERE: Empirical Resistance Equations

Fr: Froude Number [-]

f: Darcy-Weisbach resistance Eq. [-]

f_{form}: Form resistance component of resistance [-]

f_{grain}: Skin resistance component of resistance [-]

f_{spill}: Spill resistance component of resistance [-]

f_{total}: Total resistance which comprises all the resistance components [-]

g: Gravity acceleration [$L T^{-2}$]

GLUE: Generalized Likelihood Uncertainty Estimation

H: Step height [L]

HM: Hydrodynamic Model

h: Water surface elevation above a common datum [L]

h_e: Energy head loss [L]

h_v: Velocity head [L]

K: Conveyance [$L T^{-3}$]

K_{lob}, K_{mc}, and K_{rob}: Conveyance at the left overbank, main channel, and right overbank [$L T^{-3}$]

k: Contraction and expansion factor []

- k_s** : Resistance height [L]
- L**: Unit of distance /space between step peaks/reach length [L]
- L_r**: Reach length [L]
- L_{i,j}**: Distance from point i to j [L]
- LWD**: Large Woody Debris
- M**: Unit of mass or tracer mass [M]
- m**: Coefficient [-]
- MAE**: Mean average error
- N**: Number of data [-]
- NDGH**: Nondimensional hydraulic geometry equations
- n**: Manning resistance coefficient [-]
- n₀**: Base resistance [-]
- n₁**: Cross-section irregularities [-]
- n₂**: Channel variation [-]
- n₃**: Obstructions [-]
- n₄**: Channel vegetation [-]
- m**: Degree of meandering [-]
- m^{*}**: Average of measurements
- PE**: Prediction errors
- PEE**: Predictive empirical equations
- PIDL**: Physics-Informed deep learning
- PL**: Pool length [L]
- PRP**: Physical Resistance Parameter
- Q**: Flow [L T⁻³]
- q**: Unit discharge (Q w⁻¹) [L²T⁻¹]
- q^{*}**: Non-dimensional unitary flow [-]
- q^{**}**: Non-dimensional unitary flow [-]
- R**: Hydraulic Radio [L]
- RFSM**: Representative Friction Slope Method
- RMSE**: Root mean square error
- S₀**: Bed slope [-]
- S_f**: Friction slope [-]
- S_{f-form}**: Friction slope due to bed forms [-]
- S_{f-grain}**: Friction slope due to the grain resistance [-]

S_x: Average standard error of estimation

T: Unit of time [T]

TSI: Tracer Slug Injection

t_H: Harmonic travel time [T]

t_{in}: time interval [T]

\bar{t}_i : Mean time of passage of the tracer cloud at point i [T]

t_c: First momentum of the curve concentration-time [T]

U: Mean cross sectional velocity [L T⁻¹]

U*: Non-dimensional velocity [-]

U**: Non-dimensional velocity [-]

U_{meas}: Measure value

U_{pred}: Predicted values

U_{res}: Residual values

VPE: Variable Power Equation

w: Wetted width [L]

X₀: Central value of the resolution of an instrument

x: Distance or streamwise coordinate [L]

x_i: Measured value

y: Coordinate across the cross section [L]

y_i: Water depth [L]

ΔX: Resolution of an instrument

z: Bed level [L]

α: Velocity weighting coefficients [-]

Γ: Concentration of boulders [-]

δU_{meas}: Uncertainty associated with prediction of a variable

δU_{res}: Cumulative error

δU_{mean-bias}: Difference between the mean of predicted and measured variable.

δX: Uncertainty associated with the measure of a quantity "X"

δX_{cas}: Random error

δX_{res}: Resolution error

δX_{sys}: Systematic error

δX_{tot}: Total uncertainty

τ_b: Shear stress [MT⁻²L⁻¹]